Fermilab

FERMILAB-THESIS-2000-35

# A Search for Direct CP Violation in $K^{\pm} \to \pi^{\pm}\pi^{\pm}\pi^{\mp}$ Decays

by

Woon-Seng Choong

B.S. (University of California, Irvine) 1993

A dissertation submitted in partial satisfaction of the

requirements for the degree of

Doctor of Philosophy

in

Physics

in the

GRADUATE DIVISION

of the

UNIVERSITY OF CALIFORNIA, BERKELEY

Committee in charge:

Professor Kam-Biu Luk, Chair
Professor Robert Jacobsen
Professor Stephen Derenzo

Fall 2000

**A Search for Direct CP Violation in $K^{\pm} \to \pi^{\pm}\pi^{\pm}\pi^{\mp}$ Decays**



by

Woon-Seng Choong

# Abstract

A Search for Direct CP Violation in $K^{\pm} \to \pi^{\pm}\pi^{\pm}\pi^{\mp}$ Decays

by

Woon-Seng Choong

Doctor of Philosophy in Physics

University of California, Berkeley

Professor Kam-Biu Luk, Chair

An experimental search for CP violation in $K^{\pm} \to \pi^{\pm}\pi^{\pm}\pi^{\mp}$ decays has been performed in Experiment 871 at the Fermi National Accelerator Laboratory. The experiment used an 800 GeV/c primary proton beam impinging on copper targets to produce charged Kaons which were then collimated through a curved channel in a magnetic field. The three pions from the Kaon decays were tracked in the spectrometer with four high-rate multiwire proportional chambers upstream of an analysis magnet and four more downstream. The data was collected between April 1997 and September 1997, resulting in 43.3 billion positive and 18.8 billion negative Kaon triggers. Based on 41.8 million $\tau^+$ decays and 12.4 million $\tau^-$ decays of charged Kaon, the linear slope parameter $g$ describing the energy spectrum of the odd pion in the expansion of the squared matrix element was estimated using a Hybrid Monte Carlo method. This is the largest sample of $\tau$ decays of charged Kaons ever analyzed, over an order of magnitude larger than the previous analysis. The asymmetry in the linear slope $g$ was found to be

$$\frac{\Delta g}{2g_{PDG}} = [2.2 \pm 1.5(stat) \pm 3.7(syst)] \times 10^{-3}.$$

This result is consistent with no CP violation in $K^{\pm} \to \pi^{\pm}\pi^{\pm}\pi^{\mp}$ decays.

# Contents

# List of Figures

# List of Tables

# Acknowledgments

I would like to thank Kam-Biu Luk for giving me the opportunity to participate in this experiment. His enthusiasm and devotion to experimental high energy physics research has been greatly appreciated. Throughout my years with the Berkeley group, I have learned much from George Gidal, Craig Ballagh, Shigeki Misawa, Dave Pripstein, Ray Fuzesy, Boyan Turko, Ping Gu, Piotr Zyla and Tim Jones. In particular, I like to acknowledge Craig for teaching me the art of reconstruction, and Shigeki for guiding me as I ventured into object-oriented programming and C++ land.

The success of this experiment would not have been possible without the efforts of the HyperCP collaborators and the Fermilab staff. It was a pleasure working with them. I would like thank Nikos for making my time at Fermilab more enjoyble. I really enjoyed our nights out in Chicago listening to Jazz and Blues.

The past seven years has been very memorable. There were good times and there were bad times. All in all, without the friendship and support of my classmates and housemates (Lukman, Ernesto, Paul, Marc, Ed, AiAi), and friends from I-House (Marco, Asa, Insu) life in Berkeley would not have been fun. Special thanks go to Ami, and Cucee and his wife, May Quin, for being there at the right time in my life. It wouldn't be complete without mentioning Anne Takizawa and Donna Sakima from the Physics Department, and Mark Convington from LBNL for making my life as a student much more bearable.

Above all, I would like to thank my parents and my brothers for the understanding, support, patience and encouragement they gave me throughout my years as a student.

# Chapter 1

# Introduction

Symmetry is one of the fundamental concepts in physics. In 1918, Emmy Noether [1] showed that every symmetry leads to a related conserved quantity. Violation of symmetry would indicate the existence of some mechanism beyond the current understanding of physics. Our understanding of nature was once thought to be invariant under the operation of charge conjugation (C), parity (P), and time reversal (T) separately. The discoveries of parity violation in 1957 [2, 3] and CP violation in 1964 [4] led to reconsideration of the validity of these three discrete symmetries. In the following years, tremendous progress was made in our understanding of these symmetries. However, 36 years have passed since the first observation, CP violation remains a phemenonon unique to the neutral Kaon system.

Although CP violation can be accomodated in the Standard Model, our understanding of the underlying dynamics is limited. Despite many experimental efforts, our understanding improved little. However, a new generation of beautiful experiments have been performed or are underway to unlock this mystery. One of these experiments is the subject of this thesis.

## 1.1 CP Violation in the Standard Model

In this section, the Standard Model which has been extremely successful in explaining particle physics phenomena will be described. The three forces described in the Standard Model are the strong, weak and electromagnetic interactions. The fundamental constituents of nature are six quarks and six leptons. Quarks are spin-$\frac{1}{2}$ particles, have fractional electric charge, come in flavors ($+\frac{2}{3}e$ for u, c and t quarks or $-\frac{1}{3}e$ for d, s and b quarks where e is the

electric charge of the proton) and couple to all known interactions. Leptons are also spin-$\frac{1}{2}$ particles, have integer electric charge (neutral for neutrino or -$e$ for charged leptons) and couple to all known interactions except the strong force. Quarks and leptons are separately grouped in pairs and each pair is called a generation.

In the Standard Model, the interactions are mediated by bosons (particles with integral spin), and are described by a renormalizable gauge field theory based on the gauge group $SU(3)_C \otimes SU(2)_L \otimes U(1)_Y$ which are invariant under local gauge transformations.

The $SU(3)_C$ component of the gauge group called quantum chromodynamics describes the strong interaction. The subscript $C$ refers to color which specifies the strong charge of the quarks. There are three fundamental colors: red, blue and green. The gluons which mediate the strong interaction form a color octet. Quarks have not been observed as isolated particles. This fact leads to the belief that all matter must be color singlet.

The unification of weak and electromagnetic interactions [5, 6, 7], known as electroweak interaction, is described by the component $SU(2)_L \otimes U(1)_Y$ which undergoes a spontaneous symmetry breakdown:

$$SU(2)_L \otimes U(1)_Y \rightarrow U(1)_Q \tag{1.1}$$

where $Y$ and $Q$ refer to the weak hypercharge and electric charge respectively. The three gauge fields of the $SU(2)$ group, which are massless before spontaneous symmetery breaking, only interact with the left-handed weak isospin doublets of the leptonic and quark sectors as indicated by the subscript $L$. Through this way the Standard Model incorporates the fact that weak interactions violate parity. Spontaneous symmetry breaking is accomplished through the Higgs mechanism[8, 9] by introducing a complex doublet of scalar fields $\Phi$. In the process of symmetry breaking, three of the four degrees of freedom from the complex doublet are taken by the gauge fields of $SU(2)_L$ and become massive, yielding the $W^{\pm}$ and $Z^{\circ}$ bosons of the weak interactions. The remaining degree of freedom shows up as the Higgs field. The vacuum expectation value $\langle\Phi\rangle_{\circ}$ remains invariant under some effective $U(1)$ transformation which is denoted as $U(1)_Q$ in Equation 1.1. As a result, the gauge field of the electormagnetic interaction, corresponding to the photon, remains massless.

There are three generations of quarks and leptons in the Standard Model such that the left-handed ones are put into $SU(2)_L$ doublets:

$$quarks \qquad \begin{pmatrix} u \\ d' \end{pmatrix}_L, \begin{pmatrix} c \\ s' \end{pmatrix}_L, \begin{pmatrix} t \\ b' \end{pmatrix}_L \tag{1.2}$$

$$leptons \qquad \begin{pmatrix} \nu_e \\ e^- \end{pmatrix}_L, \begin{pmatrix} \nu_\mu \\ \mu- \end{pmatrix}_L, \begin{pmatrix} \nu_\tau \\ \tau- \end{pmatrix}_L \tag{1.3}$$

while the right-handed ones are transformed as singlets under $SU(2)_L$. The quarks and leptons participating in the electroweak interaction are the weak eigenstates. These fermions acquire mass through the Yukawa couplings to the scalar doublet $\Phi$. In the quark sector, the matrix relating the weak eigenstates to the mass eigenstates is given by the Cabibbo-Kobayashi-Maskawa (CKM) matrix [10, 11]

$$\begin{pmatrix} d' \\ s' \\ b' \end{pmatrix} = \begin{pmatrix} V_{ud} & V_{us} & V_{ub} \\ V_{cd} & V_{cs} & V_{cb} \\ V_{td} & V_{ts} & V_{tb} \end{pmatrix} \begin{pmatrix} d \\ s \\ b \end{pmatrix}. \tag{1.4}$$

The primed quantities correspond to the weak eigenstates, the unprimed quantities are the mass eigenstates. This mixing matrix provides a mechanism for the charge-changing weak interaction to change flavor to a different generation. In the leptonic sector, the corresponding mixing matrix is a unit matrix due to the fact that neutrinos are assumed to be massless.

The CKM matrix can be parametrized by three real rotation angles $(\theta_{12}, \theta_{13}, \theta_{23})$ and one complex phase $(\delta_{13})$ [12]:

$$V = \begin{pmatrix} c_{12}c_{13} & s_{12}c_{13} & s_{13}e^{-i\delta_{13}} \\ -s_{12}c_{23} - c_{12}s_{23}s_{13}e^{i\delta_{13}} & c_{12}c_{23} - s_{12}s_{23}s_{13}e^{i\delta_{13}} & s_{23}c_{13} \\ s_{12}s_{23} - c_{12}c_{23}s_{13}e^{i\delta_{13}} & -c_{12}s_{23} - s_{12}c_{23}s_{13}e^{i\delta_{13}} & c_{23}c_{13} \end{pmatrix} \tag{1.5}$$

where $c_{ij} = cos\theta_{ij}$ and $s_{ij} = sin\theta_{ij}$. It is through this complex phase $\delta_{13}$ in the CKM matrix that produces CP violation in the Standard Model.

## 1.2 CP Violation in Charged Kaon Decays

In the neutral Kaon system, a relatively large CP violation is caused by the $\Delta S = 2$ mixing transition between $K^\circ$ and $\bar{K}^\circ$ (indirect CP violation). In addition, there is a small direct CP violation coming from the decay of the neutral Kaon that has recently been observed [13]. However, in the charged Kaon system, $K^+ \leftrightarrow K^-$ mixing is forbidden by charge conservation. Thus, any CP asymmetry in the charged Kaon decays is unambiguously direct CP violation from $\Delta S = 1$ transition. Observation of direct CP violation outside the

neutral Kaon decays would be significant in further validating the CKM framework of CP violation.

A necessary condition for the observation of direct CP violation in charged Kaon decay is the presence of at least two decay amplitudes with different weak phases and strong rescattering phases:

$$A(K^+ \to f) = a_f e^{i\delta_a} + b_f e^{i\delta_b} \tag{1.6}$$

where $a_f$ and $b_f$ are the weak amplitudes, and $\delta_a$ and $\delta_b$ are the strong phases. Apart from an arbitrary phase $\eta$, the weak amplitudes of the corresponding anti-particle decay are complex conjugated while the strong phases, which are invariant under CP transformation, remain the same:

$$A(K^- \to \bar{f}) = e^{i\eta}(a_f^* e^{i\delta_a} + b_f^* e^{i\delta_b}). \tag{1.7}$$

Observation of CP violation in this process can be realized as an asymmetry, which is a convention-independent quantity, in the partial decay rate between the particle and anti-particle decays

$$\begin{aligned} \mathcal{A} &= \frac{,\,(K^+ \to f) - ,\,(K^- \to \bar{f})}{,\,(K^+ \to f) + ,\,(K^- \to \bar{f})} \\ &= \frac{2Im(a_f^* b_f) sin(\delta_a - \delta_b)}{|a_f|^2 + |b_f|^2 + 2Re(a_f^* b_f) cos(\delta_a - \delta_b)}. \end{aligned} \tag{1.8}$$

The weak phases within the weak amplitudes are related to the phase of the CKM matrix but they can also be related to phases due to new physics. Clearly from Equation 1.8, if there is only a single amplitude in the decay, which is equivalent to having $b_f = a_f$ and $\delta_b = \delta_a$, then the asymmetry $\mathcal{A} = 0$.

### 1.2.1 Decay Amplitudes of Charged $K \to 3\pi$

There are two distinct three-pion decay modes for the charged Kaon:

$$K^\pm \to \pi^\pm \pi^\pm \pi^\mp, \tag{1.9}$$

$$K^\pm \to \pi^\circ \pi^\circ \pi^\pm. \tag{1.10}$$

Historically, (1.9) and (1.10) are known as $\tau$ and $\tau^{'}$ decays respectively. The partial decay rate of the three-body decays can be written as

$$d, \; = \frac{1}{(2\pi)^5 16 m_K} |\mathcal{M}|^2 \; dE_1 \; dE_2 \; d\alpha \; d(cos\beta) \; d\gamma \tag{1.11}$$

where $E_1$ and $E_2$ are the energies of two of the daughter particles, and ($\alpha$, $\beta$, $\gamma$) are the three Euler angles that specify the orientation of the final system relative to the parent particle. Since the decaying particles are pseudoscalars, the angles can be integrated out. As a result, the decay amplitudes depend only on two independent kinematical variables. In particular, for charged $K \to 3\pi$ decays, one can define the following kinematical invariants:

$$s_i = (p_K - p_i)^2 = (m_K - m_i)^2 - 2m_K T_i \ , \ i = 1, 2, 3 \tag{1.12}$$

and

$$s_0 = \frac{1}{3}\sum_i s_i = \frac{1}{3}(m_K^2 + m_1^2 + m_2^2 + m_3^2) \tag{1.13}$$

where $p_i$ are the momentum 4-vectors, $m_i$ and $T_i$ are the mass and kinetic energy of the $i^{th}$ pion in the center of mass frame respectively, and $m_K$ and $p_K$ are the mass and momentum 4-vector of the charged Kaon respectively. The index 3 is used for the odd pion (the pion that is opposite in charge to the other two same charge pions). In terms of $s_0$ and $s_i$, two independent kinematical variables can be chosen as

$$X = \frac{|s_1 - s_2|}{m_\pi^2}, \tag{1.14}$$

$$Y = \frac{s_3 - s_0}{m_\pi^2}. \tag{1.15}$$

$X$ is taken to be positive because the two same-sign pions are identical.

Since the three-pion phase space is quite small, $Q = m_K - 3m_\pi \sim 80$ MeV, higher-order terms in $X$ and $Y$ corresponding to higher angular momenta are highly suppressed. Thus, it is possible to expand the Dalitz distribution in powers of $X$ and $Y$. Current experimental data on charged $K \to 3\pi$ have been analyzed up to the quadratic terms in $X$ and $Y$

$$|A(K \to 3\pi)|^2 \propto 1 + gY + hY^2 + kX^2 \tag{1.16}$$

where $g = -0.2154 \pm 0.0035$, $h = 0.012 \pm 0.008$, and $k = -0.0101 \pm 0.0034$ are from the Particle Data Group (PDG) [14]. The term linear in $X$ in missing because of Bose symmetry. The Dalitz plot of a sample of simulated $\tau$ decays of charged Kaon using the PDG numbers is shown in Figure 1.1.

Since a charged Kaon has isospin $I = 1/2$ and pion has $I = 1$, the $3\pi$ final state from charged Kaon decays can be combined to give $I = 1, 2, 3$. The linear combinations of the $I = 1$ states can be completely symmetric or mixed; the $I = 2$ state is mixed; and finally

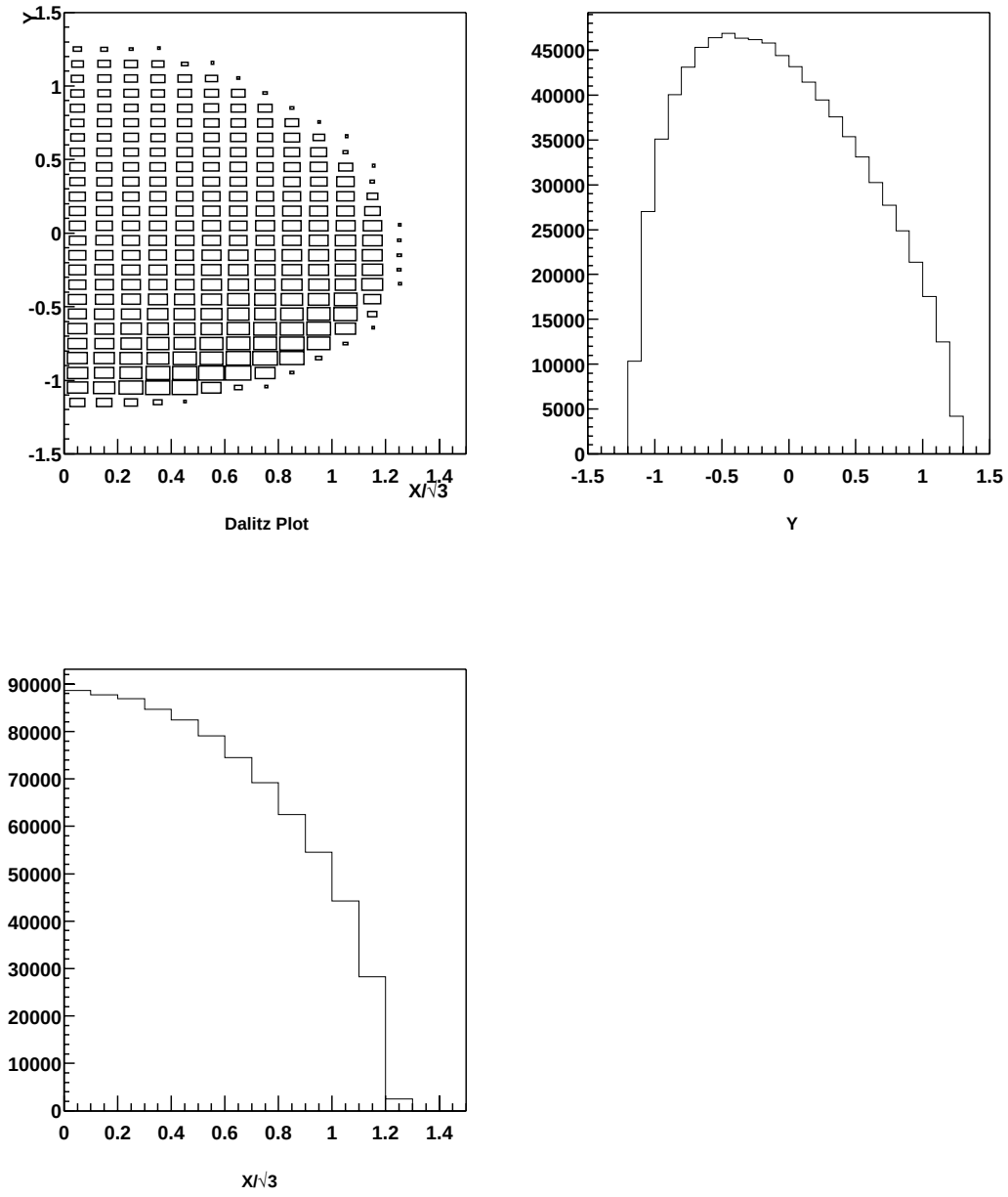


Figure 1.1: Dalitz plot of simulated $\tau$ decays of charged Kaon (top left) using PDG numbers. The size of each box in the plot is proportional to its contents. The $X/\sqrt{3}$ and $Y$ projections are also shown.

the $I = 3$ state is completely symmetric. Experimentally, transitions with isospin change $|\Delta I| = 1/2$ dominant over $|\Delta I| = 3/2$. The origin of this enhancement of $|\Delta I| = 1/2$ transitions over $|\Delta I| = 3/2$ is not completely understood yet and is referred to as the $|\Delta I| = 1/2$ rule. By requiring Bose symmetry in the total final-state wavefunction and restricting to $|\Delta I| = 1/2, 3/2$ transitions, the transition amplitudes for charged $K \to 3\pi$ decay can be expanded in terms of $X$ and $Y$ as follows [15, 16]:

$$\begin{aligned} A(K^+ \to \pi^+\pi^+\pi^-) &= (a_{11} + a_{13})e^{i\delta_{1S}} + [-(b_{11} + b_{13})e^{i\delta_{1M}} + b_{23}e^{i\delta_2}]Y \\ &\quad + c(Y^2 + X^2/3)e^{i\delta_{1S}} + d(Y^2 - X^2/3)e^{i\delta_{1M}}, \qquad (1.17) \\ A(K^+ \to \pi^\circ\pi^\circ\pi^+) &= (a_{11} + a_{13})e^{i\delta_{1S}} + [(b_{11} + b_{13})e^{i\delta_{1M}} + b_{23}e^{i\delta_2}]Y \\ &\quad + c(Y^2 + X^2/3)e^{i\delta_{1S}} + d(Y^2 - X^2/3)e^{i\delta_{1M}}. \qquad (1.18) \end{aligned}$$

The amplitudes $a$'s and $b$'s have two subscripts: the first denotes the isospin of the final-state and the second is twice the change in isospin between the initial and final states. The final state strong phases in $I = 1, 2$ and mixed symmetry $I = 1$ states are given by $\delta_{1S}$, $\delta_2$ and $\delta_{1M}$ respectively. In fact, these representations are only correct at the centre of the Dalitz plot because strong interaction can mix the two $I = 1$ states. If isospin breaking is included, even $I = 1$ and $I = 2$ can get mixed, which can lead to more phases [17]. Thus, Equations 1.17 and 1.18 are used only to show the main contributions of the amplitudes to direct CP violation.

### 1.2.2 CP-violating Effects in $K^\pm \to \pi^\pm\pi^\pm\pi^\mp$

There are two ways to look for CP-violating effects in charged $K \to 3\pi$ transitions: (1) through the asymmetry of the partial decay rates; and (2) through the asymmetry in the Dalitz distribution, in particular, the linear slope parameter. One can define the following CP-violating observables:

$$\delta, = \frac{, _{\tau^+} - , _{\tau^-}}{, _{\tau^+} + , _{\tau^-}}, \qquad (1.19)$$

$$\delta g = \frac{g_{\tau^+} - g_{\tau^-}}{g_{\tau^+} + g_{\tau^-}}. \qquad (1.20)$$

In particular, one can write

$$\delta g = \frac{Im[(a_{11} + a_{13})^*(b_{11} + b_{13})]sin(\delta_{1S} - \delta_{1M}) + Im[(a_{11} + a_{13})^* b_{23}]sin(\delta_{1S} - \delta_2)}{Re[(a_{11} + a_{13})^*(b_{11} + b_{13})]cos(\delta_{1S} - \delta_{1M}) + Re[(a_{11} + a_{13})^* b_{23}]cos(\delta_{1S} - \delta_2)}. \qquad (1.21)$$

It is important to note here that the dominant CP-violating interference as required by Equation 1.21 is between two $|\Delta I = 1/2|$ amplitudes ($a_{11}$ and $b_{11}$). This is in contrast to the CP-violating effects in the neutal Kaon system where the interference is between a $|\Delta I = 1/2|$ and a $|\Delta I = 3/2|$ amplitudes. This fact could lead to a possible enhancement of direct CP-violating effect in charged Kaon decays as has been demonstrated in some higher order calculations of the amplitudes [18, 19]. Unfortunately, it is very difficult to make definite predictions in these higher order calculations.

Theoretical predictions of $\delta$, and $\delta g$ require the calculation of the transition amplitude in Equation 1.17. In principle, one can use the full Hamiltonian of the Standard Model to do the calculation but this can be a formidable task. However, in the low-energy limit, the transition amplitude can be calculated by introducing an effective Hamiltonian. The non-leptonic effective weak Hamiltonian for $\Delta S = 1$ transitions is written as [20, 21, 22, 23]

$$\mathcal{H}_{eff} = \frac{G_F}{\sqrt{2}} V_{ud} V_{us}^* \sum_i C_i(\mu) Q_i(\mu) \tag{1.22}$$

where $G_F$ is Fermi constant, $C_i(\mu)$ are the complex Wilson coefficients describing the couplings in perturbative QCD and $Q_i(\mu)$ are the local four-quark operators with the selection rules $\Delta S = 1$ and $\Delta I = 1/2, 3/2$. The renormalization scale $\mu$ separates the physics contributions into the short-distance (perturbative) calculation of the coupling $C_i(\mu)$ and the long-distance (non-perturbative) calculation of the matrix elements $\langle 3\pi|Q_i(\mu)|K\rangle$. Since the result cannot depend on the choice of $\mu$, the $\mu$-dependence of the coefficients $C_i(\mu)$ must cancel the $\mu$-dependence of the hadronic matrix elements. Since the hadronic matrix elements involve long-distance contributions, one has to resort to non-perturbative methods such as lattice QCD calculations, the $1/N_c$ expansion where $N_c$ is the number of quark colors, chiral perturbation theory, and many others.

A number of authors [17, 19, 24, 25, 26, 27] have estimated the magnitude of the CP-violating observables in charged $K \to 3\pi$ decays. The results are summarized in Table 1.1. The rate asymmetry $\delta$, is over 2 orders of magnitude smaller than the slope asymmetry $\delta g$ because the integral over the Dalitz plot of the terms linear in $Y$ is zero causing the rate asymmetry to be highly suppressed. Thus, experimentally, it is more likely to observe a CP-violating effect by measuring $\delta g$ which is the subject of this thesis.

As I have alluded, making definite predictions of the transition amplitudes is not easy and this is clearly seen from the predictions of $\delta g$ which range from $10^{-4}$ to $10^{-6}$. This large discrepancy in the estimates stems from the large uncertainties in performing the

| | $\|\delta g\|$ | $\|\delta, \|$ |
|---|---|---|
| H.-Y. Cheng (1991) | $< 1 \times 10^{-5}$ | |
| D'Ambrosio *et al.* (1991) | $< 1 \times 10^{-5}$ | |
| Isidori *et al.* (1992) | $\sim 1 \times 10^{-6}$ | $(2-4) \times 10^{-8}$ |
| E.P. Shabalin (1993) | $\leq (5 \pm 2) \times 10^{-5} \|sin\delta\|$ | |
| A.A. Bel'kov *et al.* (1993) | $\sim 0.5 \times \|\epsilon'/\epsilon\|$ | |
| D'Ambrosio *et al.* (1998) | $< 10^{-5}$ | |
| E.P. Shabalin (1998) | $\sim 2 \times 10^{-4}$ | |

Table 1.1: Theoretical predictions of the rate and slope asymmetries for $K^{\pm} \to \pi^{\pm}\pi^{\pm}\pi^{\mp}$.

non-perturbative calculations of the hadronic matrix elements and also from the lack of experimental data on decay parameters that are taken as inputs in the calculations. In general, the calculations use chiral perturbation theory up to $O(p^4)$ in the expansion coupled with predictions from lattice QCD. Predictions of $O(p^4)$ using the framework of chiral perturbation theory in the limit of $N_c \to \infty$ has been considered in [24] and using linear $\sigma$-model in [26]. Belkov *et al.* [27] argues that the other predictions [17, 19, 24, 25, 26] did not take into account the full corrections to $O(p^4)$ resulting in lower estimates in the asymmetries. On the other hand, using a model-independent approach, D'Ambrosio, G. Isidori and N. Paver [19, 25] put an upper limit on $\delta g$ of about $10^{-5}$ and claimed that Belkov *et al.* [27] overestimated the final-state rescattering phase difference. For beyond- Standard-Model predictions, Shabalin [28] predicted an enhancement by including spontaneous CP violation in the Higgs sector by incorporating more than two Higgs doublets.

### 1.2.3 Experimental Limit on $\delta g$

The only dedicated experiment measuring $\delta g$ was performed in 1970 at the Alternating Gradient Synchrotron (AGS) of the Brookhaven National Laboratory [29]. About 3.2 million $\tau$ decays were collected, approximately 1.6 million for each charge of the Kaon. They did not observe any CP-violating effect and obtained a result of $\delta g = -0.0070 \pm 0.0053$.

# Chapter 2

# Experiment

The experiment described in this thesis was carried out at the Fermi National Accelerator Laboratory (Fermilab) during the 1997 fixed-target run. The E871 spectrometer used to carry out the search for the CP violation in charged $K \to 3\pi$ was located in the Meson Center beam line at Fermilab. The layout of the experimental area is shown in Figure 2.1. It was a fixed-target experiment using an 800 GeV/c primary proton beam provided by the Tevatron accelerator at Fermilab. Secondary particles were produced through interactions of the proton beam with a copper (Cu) target, and were collimated with a curved magnetic collimator to select a narrow momentum bite and the desired charge polarity. The primary goal of the experiment is to search for possible CP violation in hyperon decays at very high sensitivity. Therefore, having high yield of secondary particles, in particular hyperons, is a prerequisite of the experiment. In addition to hyperons, there is also a large number of charged Kaons in the secondary beam, hence allowing the experiment to perform the search reported in this thesis.

## 2.1 Beam

The 800 GeV/c protons were delivered to the experiment over a cycle time of approximately 60.5 seconds (the spill cycle). The accelerator took about 25.0 seconds to accelerate the protons to 800 GeV/c. These protons were then extracted from the accelerator to the fixed-target beam lines for about 23.0 seconds. After that the superconducting magnets ramped back down. The protons were accelerated by RF cavities running at 53.1 MHz resulting in a bunched beam with protons populating 1-ns-long RF buckets. The separation

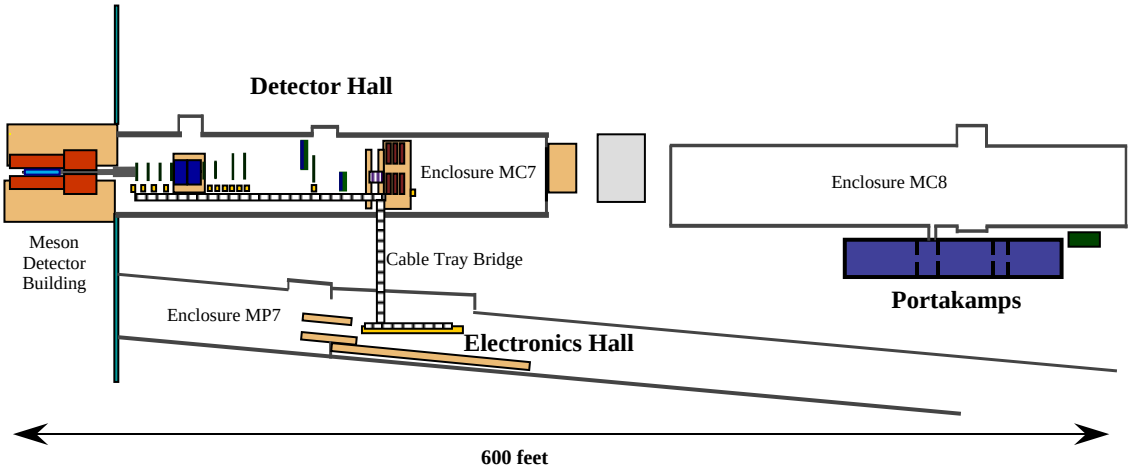


Figure 2.1: Experimental area. The spectrometer was in MC7, readout and trigger electronics were in MP7, and the data acquisition system and on-line computers were in the Portakamps.

between two adjacent buckets in time was, determined by the RF frequency, about 19 ns. In the first few seconds of beam extraction, there was a series of high intensity proton pulses (pings) that was used by neutrino experiments. These pings were gated off from the trigger, resulting effectively in about 19 seconds of beam to the experiment.

Typically the proton intensity delivered to the experiment was about $1.5 \times 10^{11}$ protons per spill. The intensity was monitored using an ion chamber (MC6IC) and a secondary emission monitor (MC6SEM).

The beam position and targeting were monitored using two 0.5 mm wire pitch segmented wire ion chamber (SWIC) separated by 245.0 cm with the first one located 20.3 cm from the center of the target. In order to have good targeting fraction, the beam spot at the target was elliptic in cross-section, about 1.2 mm full-width at half maximum (FWHM) in the horizontal direction and about 0.9 mm FWHM in the vertical direction. Although some data were taken with non-zero production angles for other physics topics and for systematic studies, the data used in this analysis has a mean production angle of approximately 0.5 mrad.

## 2.2 Laboratory Coordinate System

The laboratory coordinate system $(x, y, z)$ is defined by 156.7 GeV/c (note that this momentum is different from the average beam momentum at the exit of the collimator which is about 170 GeV/c) secondary beam tracks with a mean transverse momentum of zero GeV/c and centered at the exit of the collimator (to be described in Section 2.4) without any field in the analysis magnet. The Z-axis lies along these tracks. The Y-axis is perpendicular to the Z-axis and pointing upward, and the X-axis is defined by a right-handed coordinate system. The origin of the coordinate system is taken to be the center of the aperture at the exit of the collimator.

Beam tracks with a momentum of 156.7 GeV/c are traced back to the location of the target at $z_{target} = -638.8$ cm. Inside the collimator, the Z-axis of the laboratory coordinate system is defined by these beam tracks with the target centered on the Z-axis and is denoted as the central orbit.

## 2.3 Targets

In the 1997 run, two copper targets with a transverse dimension of 2.0 mm $\times$ 2.0 mm and length 2.2 and 6.0 cm were used to produce positively and negatively charged Kaons respectively. Different target lengths were used to produce approximately the same particle flux in the spectrometer. The target box was made of two 1-mm-thick ceramic plates separated by 1.0 cm. Each ceramic plate had holes with 2.8 mm diameter cut out of it as shown in Figure 2.2 to hold the targets. Only the four holes at the corners had targets installed. The middle holes were left empty. The targets were positioned such that the centers of the target length were located at z = -638.8 cm. The target box was mounted on a mover that could be controlled remotely to move vertically and horizontally in step of 53.7 $\mu$m. Depending on the running condition, the appropriate target was moved into position to intercept the proton beam.

## 2.4 Collimator and Hyperon Magnet (M1)

The secondary charged particles produced at the target were collimated by a curved collimator embedded in a 6.096 m long dipole magnet (M1). The collimator consisted of

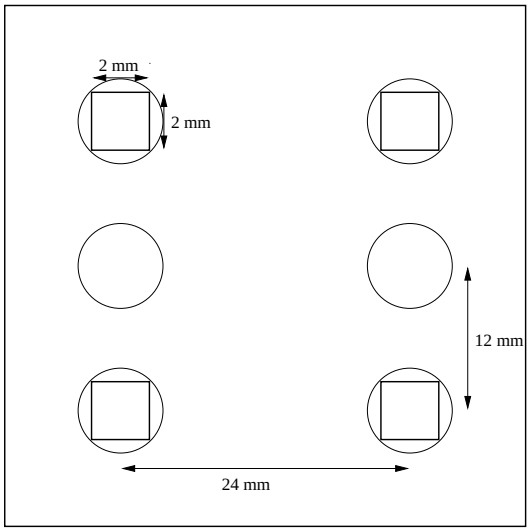


Figure 2.2: Beam-eye view of ceramic plate of target box.

five sections, made out of brass and tungsten, joined together as shown in Figure 2.3. It was fitted snugly inside the beam pipe of M1 with both ends capped off with 75-$\mu$m-thick kapton windows. The collimator was filled with helium gas to reduce multiple scattering and interaction. The upstream tungsten section had the smallest aperture, hence defining the acceptance of the secondary charged beam. The defining aperture was 0.5 cm high in the vertical direction and 1.0 cm wide in the horizontal direction, giving a solid angle of 4.88 $\mu$sr with respect to the entrance of the collimator. This tungsten section also served as a dump for the protons that did not interact in the target.

The design of the collimator has been optimized to maximize the fraction of charged $\Xi$ in the secondary beam and to select a narrow momentum bite. The radius of curvature of the collimator was 270.27 m and the bend angle, defined by the tangents to the central orbits at the entrance and the exit of the collimator, was 19.56 mrad. M1 produced a horizontal field of 1.667 T at 4200 A, bending the charged particles of interest vertically upward with the central orbit corresponding to the trajectory of a charged particle with momentum 156.7 GeV/c and zero transverse momentum. The acceptance of the collimator as a function of the secondary beam momentum is shown in Figure 2.4. During the experiment, the target was not completely centered at the opening of the collimator, resulting in a higher average secondary beam momentum. Figure 2.5 shows the distribution of the reconstructed

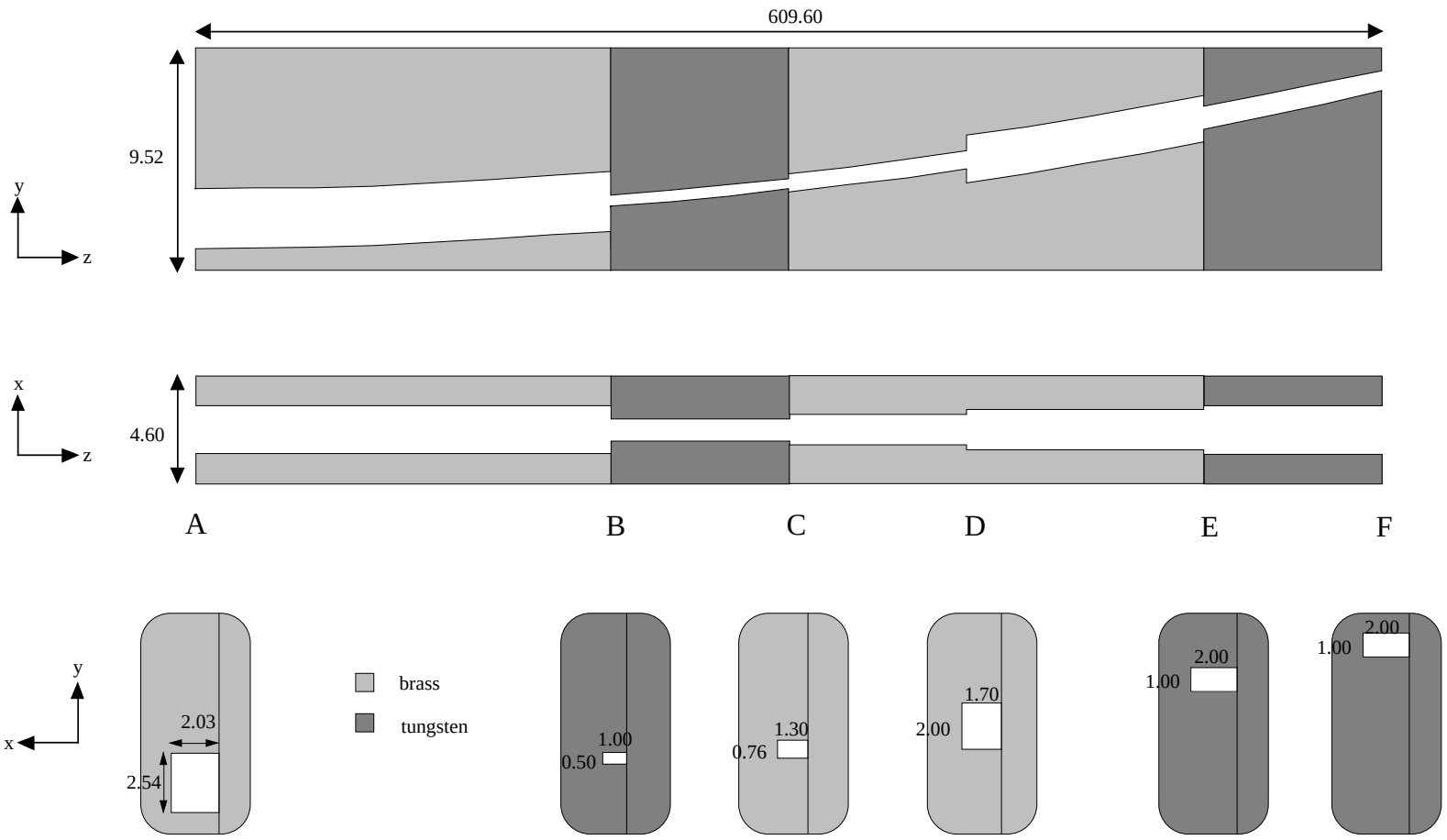


Figure 2.3: Schematic of collimator.

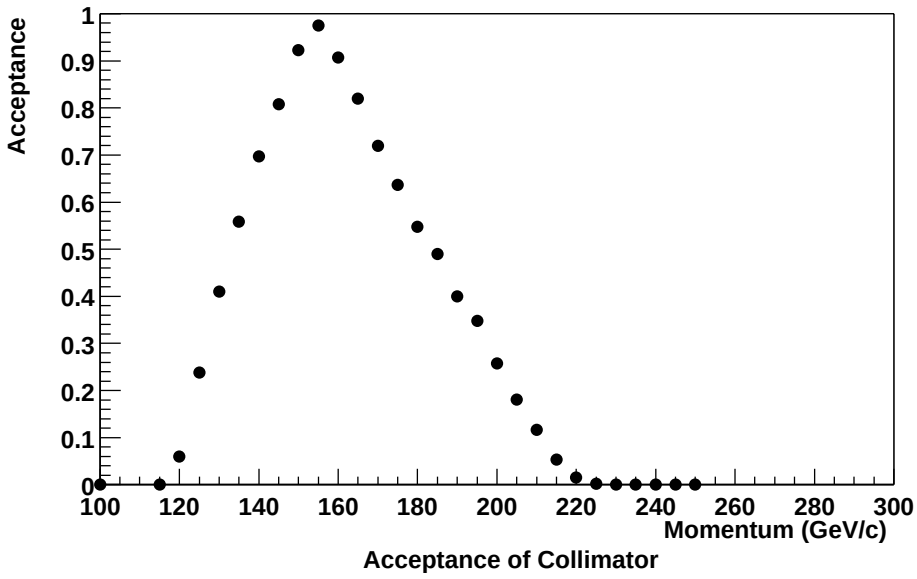


Figure 2.4: Acceptance of collimator. A field of 1.667 T is used.

momentum for charged Kaons.

The polarity of M1 was reversed when switching from selecting positively charged beam to negatively charged beam and vice versa. The field inside M1 was monitored using two Hall probes [30] located about 60.0 cm from the exit of the collimator and approximately centered inside the beam pipe. The Hall probes had a precision of about $2 \times 10^{-4}$ T.

## 2.5 Decay Pipe

Downstream of the collimator was a decay pipe which consisted of three cylindrical vessels joined together, resulting in a total length of 1300 cm. The diameters of the vessels were 15.2 cm, 30.5 cm and 61.0 cm, growing larger as it progressed downstream to accommodate the divergence of the decay particles. The decay pipe was evacuated to better than 1 mTorr to minimize multiple scattering and interaction. The upstream end of the decay pipe was closed with a 76-$\mu$m-thick titanium window and the downstream end was covered with a 0.51-mm-thick aluminized kelvar window, together representing about 0.115% of an interaction length.

The charged Kaons exiting the collimator had an average momentum of about 170 GeV/c. Therefore, only about 1.2% of them decayed inside the decay pipe.

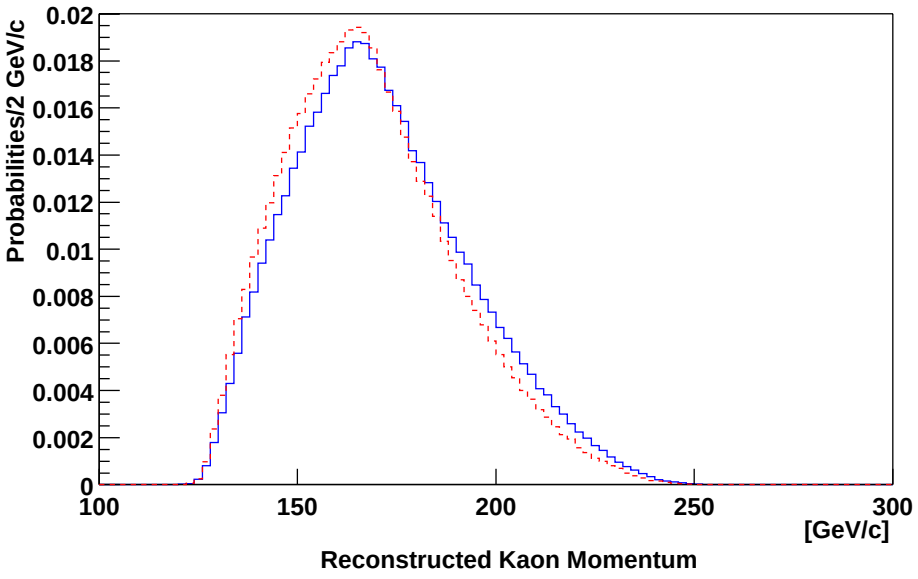


Figure 2.5: Probability distributions of the reconstructed positively (line) and negatively (dash) charged Kaon momentum. The momentum distributions are slightly different because of the different production dynamics for particles and anti-particles.

## 2.6 Spectrometer

The E871 spectrometer was designed to detect over a billion hyperon decays in addition to the charged Kaon decays. Given a running period of about 6 months, this was necessarily a high-rate spectrometer. The secondary beam rate at the exit of the collimator was about 20 MHz. The spectrometer was also simple to keep the number of possible sources of systematic effects small and controllable as required for measuring CP asymmetry to high precision. The plan and elevation views of the spectrometer is shown in Figure 2.6. All the detector elements were oversized in the Y-dimensions to fully accept events in the vertical direction. However, low-momentum particles can be swept out of the active area of the downstream detectors by the analysis magnet.

### 2.6.1 Wire Chambers

Tracking of charged particles transversing the spectrometer was accomplished by two sets of tracking stations, one uptream of the analysis magnet (M2) and the other downstream. Each of the tracking stations was made up of four multiwire proportional chambers

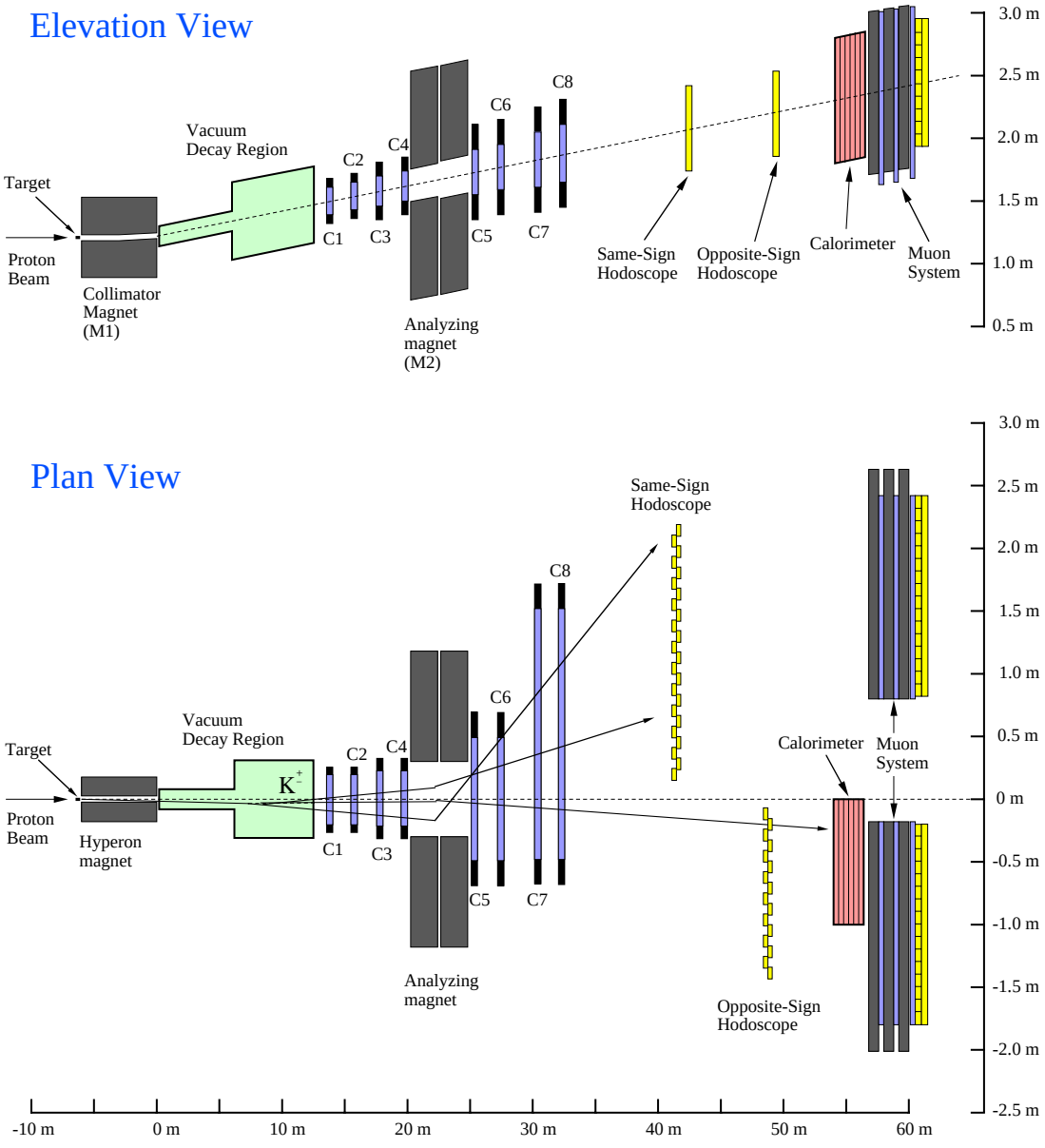


Figure 2.6: Plan and elevation views of spectrometer.

(MWPC) separated approximately by 2 m from each other. The transverse dimension of the chamber increased as proceeding downstream in order to accept the charged particles that diverged and got swept apart by the analysis magnet.

All of the MWPCs had similar design and readout. For each MWPC, there were four anode wire planes sandwiched by cathode foils and two outer grounded foils terminating the field region. The cathode and ground foils were made of 25-$\mu$m-thick kapton with 1200-Å-thick gold deposited on both surfaces. The anodes consisted of two planes of vertical wires (X and X') shifted by half a wire spacing relative to each other to resolve left-right ambiguity, and two stereo views (U and V) with the wires inclined at $\pm 26.6^\circ$ ($\pm tan^{-1}\frac{1}{2}$) from the vertical. The stereo angles were chosen in such a way that the resolution in the bend and non-bend views were comparable. All the MWPCs had small anode-cathode gaps (3 mm) and narrow wire spacings in order to handle the intense secondary beam emanating from the collimator. The wire spacing ranged from 1 mm for the two most upstream wire chambers to 2 mm for the two most downstream chambers. Furthermore, the decay particles occupied the same region in the upstream wire chambers as the secondary beam whereas in the downstream chambers they occupied somewhat disjoint regions. Therefore, the upstream wire chambers were filled with a "fast-gas" mixture of $CF_4$-isobutane in 50-50 ratio by weight to reduce their sensitivity to out-of-time hits. On the other hand, the downstream wire chambers were filled with a 50-50 Argon-Ethane mixture bubbled through isoproply alcohol at -2.8°C as timing resolution was less demanding. Additional information about the wire chambers are summarized in Table 2.1 and 2.2.

Over the course of the run in 1997, approximately 0.02 C/cm of charge was accumulated along the wires in the secondary beam region of the upstream wire chambers. The gains of the upstream wire chambers were monitored periodically with a $^{55}$Fe source in the secondary beam region. There was no indication of any degradation in gain of the anode wire due to aging.

High-gain preamplifiers with a gain of about 19 mV/fC were mounted directly on the wire chambers. With this electronics gain, the wire chambers could be operated at low avalanche gain of about $4 \times 10^4$ to minimize the effect of aging and still achieved high efficiencies. Each preamplifier contained 16 channels. The differential outputs of two preamplifiers were sent to one 32-channel discriminator boards, housed in VME 6U crates near the wire chambers, through a twist-and-flat cable ranging between 10 m and 15 m in length. For reasons related to radiation safety and space, the readout and trigger electronics were

| MWPC | Plane View | z Position ($cm$) | Number of Wire | Wire Spacing ($mm$) | Stereo Angle (degree) | Anode Diameter ($\mu m$) |
|---|---|---|---|---|---|---|
| C1 | X | 1385.4 | 320 | 1.016 | 0 | 12.5 |
| | U | 1386.0 | 384 | 1.016 | -26.6 | 12.5 |
| | V | 1386.6 | 384 | 1.016 | 26.6 | 12.5 |
| | X' | 1387.2 | 320 | 1.016 | 0 | 12.5 |
| C2 | X | 1585.6 | 320 | 1.016 | 0 | 12.5 |
| | U | 1586.2 | 384 | 1.016 | -26.6 | 12.5 |
| | V | 1586.8 | 384 | 1.016 | 26.6 | 12.5 |
| | X' | 1587.4 | 320 | 1.016 | 0 | 12.5 |
| C3 | X | 1784.0 | 320 | 1.270 | 0 | 12.5 |
| | U | 1784.6 | 384 | 1.270 | -26.6 | 12.5 |
| | V | 1785.2 | 384 | 1.270 | 26.6 | 12.5 |
| | X' | 1785.8 | 320 | 1.270 | 0 | 12.5 |
| C4 | X | 1984.7 | 320 | 1.270 | 0 | 12.5 |
| | U | 1985.3 | 384 | 1.270 | -26.6 | 12.5 |
| | V | 1985.9 | 384 | 1.270 | 26.6 | 12.5 |
| | X' | 1986.5 | 320 | 1.270 | 0 | 12.5 |

Table 2.1: Information of upstream wire chambers

| MWPC | Plane View | z Position ($cm$) | Number of Wire | Wire Spacing ($mm$) | Stereo Angle (degree) | Anode Diameter ($\mu m$) |
|---|---|---|---|---|---|---|
| C5 | X | 2566.0 | 800 | 1.501 | 0 | 15.0 |
| | V | 2566.6 | 816 | 1.501 | 26.6 | 15.0 |
| | U | 2567.2 | 816 | 1.501 | -26.6 | 15.0 |
| | X' | 2567.8 | 800 | 1.501 | 0 | 15.0 |
| C6 | X | 2768.4 | 800 | 1.501 | 0 | 15.0 |
| | V | 2769.0 | 816 | 1.501 | 26.6 | 15.0 |
| | U | 2769.6 | 816 | 1.501 | -26.6 | 15.0 |
| | X' | 2770.2 | 820 | 1.501 | 0 | 15.0 |
| C7 | X | 3069.0 | 992 | 2.000 | 0 | 20.0 |
| | V | 3069.6 | 1008 | 2.000 | 26.6 | 20.0 |
| | U | 3070.2 | 1008 | 2.000 | -26.6 | 20.0 |
| | X' | 3070.8 | 992 | 2.000 | 0 | 20.0 |
| C8 | X | 3269.3 | 992 | 2.000 | 0 | 20.0 |
| | V | 3269.9 | 1008 | 2.000 | 26.6 | 20.0 |
| | U | 3270.5 | 1008 | 2.000 | -26.6 | 20.0 |
| | X' | 3271.1 | 992 | 2.000 | 0 | 20.0 |

Table 2.2: Information of downstream wire chambers

located in a neighboring beam line (MP7) as shown in Figure 2.1. Custom-designed cables (Ansley flat cable) were used to connect the differential-ECL outputs of the discriminators to the latch cards. The cable with tranverse dimensions of 7.6 cm by 0.08 cm consisted of 100 fine wires embedded in heavy-duty polyethylene. It had a characteristic impedance of 150 ohms and a propagation delay of 4.9 ns/m. It also possessed superior attenuation and dispersion characteristics, maintaining differential-ECL signal integrity with 1-bucket timing after propagating for a long distance. The length of the cables ranged from 30 m to 90 m. These long Ansley cables also provided trigger delay.

### 2.6.2 Analysis Magnet (M2)

The momentum analyzing magnet was located between the two sets of tracking stations. It was made up of two dipole magnets, known as BM109 in Fermilab, separated from each other by a small gap (7.6 cm). For each BM109, the physical length was 228.6 cm and the effective field length was 194.0 cm. The aperture of the upstream BM109 was 61.0 cm wide by 26.0 high, whereas the aperture of the downstream BM109 was 61.0 cm wide by 30.5 cm high. The field in the central volume of the magnet, mapped with a Fermilab ziptrack to a precision of a few times $10^{-4}$ T, was fairly uniform. In addition, during data taking, the field was measured spill-by-spill with two Hall probes located on the bottom plate in the aperture near the middle of each magnet. The readings of these Hall probes were used to correct for any variation in the overall field in the analysis. The two BM109 magnets were operated at 2500 A with the major component of the field directed vertically. The total transverse momentum ($p_t$) kick was 1.426 GeV/c. With this kick, the decay particles were separated from each other as well as from the secondary beam in the downstream section of the spectrometer.

### 2.6.3 Hodoscopes

Two stations of hodoscopes (OS and SS hodoscopes) were used to detect the decay particles quickly as they transversed the spectrometer. The OS hodoscope was located at z = 4110.0 cm on the opposite-sign charge (relative to the charge of the secondary beam) side of the spectrometer, hence the designation OS. The SS hodoscope was located at z = 4841.3 cm on the same-sign charge side of the spectrometer but away from the passage of the secondary beam. The OS hodoscope consisted of 16 scintillation counters, whereas

there were 24 counters in the SS hodoscope. Each counter was 9.0-cm-wide by 66.0-cm-high and 2.0-cm-thick. To reduce inefficiency, each counter was overlapped with its neighbors by about 1.3 cm. The names of the counters were given by OSn or SSn where n denoted the counter number starting from one. OS1 and SS1 were closest to and OS16 and SS24 were farthest away from the secondary beam in the X direction.

### 2.6.4 Calorimeter

The calorimeter was a sampling hadronic calorimeter that was used to reduce the trigger rate due to particles from secondary interactions and to provide a muon-blind component to the CP-physics triggers. In addition, the response of the calorimeter was fast to handle the high rate of events in the spectrometer. The calorimeter contained 64 layers of 2.41-cm-thick Fe and 0.5-cm-thick plastic scintillator. The total length of the calorimeter was 238.9 cm, corresponding to 9.6 interaction length ($\lambda_I$) and 88.5 radiation length ($X_\circ$). The light output was read out using wavelength shifter fibers that were embedded in keyhole-shaped grooves that were machined in the scintillator. The fibers were 2 mm in diameter and 2-m-long, and were read out at one end with the other end polished and sputtered with aluminium. The calorimeter was divided into 8 cells, four longitudinal columns and two lateral rows. The readout ends of the fibers, 256 per cell, were potted in opaque epoxy before attaching to an arcylic light guide of the photomultiplier tube. The energy resolution of the calorimeter was determinined to be approximately $\sigma/E \approx 0.8/\sqrt{E}$.

The transverse size of the calorimeter was $99.0 \times 98.0$ cm$^2$ and was designed such that all the protons from $\Lambda$s decayed inside the decay pipe lie in a fiducial area of about half of the active area and more than 20 cm away from the edges of the calorimeter. However, the odd pions from charged Kaon decays were much softer than the protons from $\Lambda$ decays, hence occupying a much larger area than the calorimeter could cover in the X dimension. Therefore, the calorimeter could only trigger on about 60% of the charged Kaons decaying inside the decay pipe as shown in Figure 2.7.

### 2.6.5 Muon System

The muon system at the rear of the spectrometer was used for studying rare and forbidden decays of strange particles. The muon system was made of two similar stations on either side of the spectrometer. Each station contained three layers of 0.81-m-thick steel

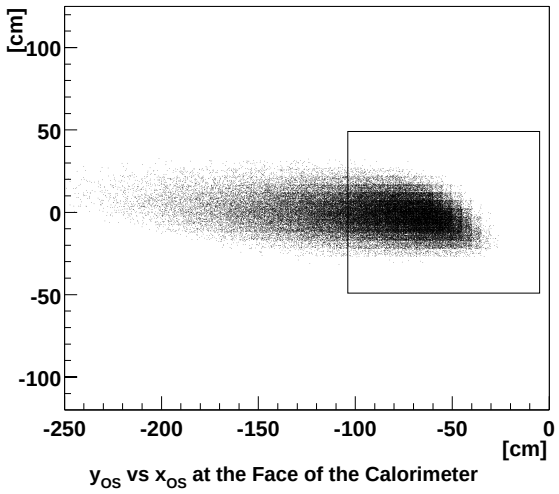


Figure 2.7: Distribution of Y-position versus X-position of opposite-sign pion from simulated $\tau$ decay of charged Kaon at the location of the calorimeter. The box indicates the cross-section of the upstream face of the calorimeter.

interspersed with three layers of proportional tubes with vertical and horizontal wires. The tubes used an Argon-$CO_2$ (90/10) gas mixutre. Behind the last proportional tube layer were two orthogonal hodoscopes used to trigger on muon events. The information from the muon system was not used in the analysis presented in this thesis.

## 2.7 Trigger

In order to minimize any potential systematic effects, the triggering system was designed to be simple and fast. In addition, only a first-level trigger system was employed. All of the decays of interest to the experiment consisted of at least three charged particles at the rear of the spectrometer, one on the OS side and at least one on the SS side. Therefore, common to all the physics triggers was a left-right coincidence of charged particles: (1) the presence of at least one charged particles in the OS hodoscope; and (2) the presence of at least one charged particles in the SS hodoscope. Furthermore, an OS particle would deposit significant amount of energy in the calorimeter. The minimum momentum of the proton from a $\Lambda$ decay was around 70 GeV/c, while the minimum momentum of the odd pion from

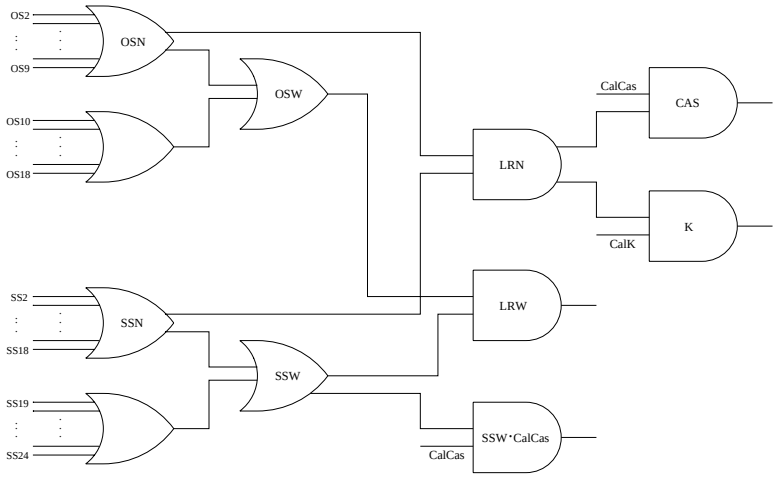


Figure 2.8: Trigger logic for CAS, K and some monitoring triggers.

a charged Kaon decay was around 20 GeV/c. However, the calorimeter at the designed location was only able to accept particles with momentum of at least 40 GeV/c. Therefore, two thresholds on the analog sum of the signals from all the photomultiplier tubes of the calorimeter were used, one denoted as CalCas which had an energy threshold of 50 GeV/c for identifying the proton from a $\Lambda$ decay, and the other with a threshold of 30 GeV/c denoted as CalK for the OS pion from a charged Kaon decay. Since the calorimeter did not have full acceptance for detecting the odd pion from a charged Kaon decay, a narrower region of the OS hodoscope, donoted as OSN which was the logic OR of OS2 to OS9, was required. In addition, only the logic OR of SS2 to SS18, denoted as SSN, was required to trigger on at least one of the SS pions from the hyperon and charged Kaon decays. The main physics trigger for the hyperon and charged Kaon decays were the coincidence CAS = OSN·SSN·CalCas and K = OSN·SSN·CalK respectively as shown in Figure 2.8. Without any system dead time, a typical K trigger rate was 67 kHz and the overall trigger rate including CAS, muon and monitoring triggers was 84 kHz.

In addition to the main physics triggers, some of the monitoring triggers were SSW·CalCas and LRW as described in Figure 2.8. SSW·CalCas and LRW were prescaled by a factor of 100 and 200 respectively. The former trigger was used to calculate the efficiency of the OS hodoscope, while the latter was used to calculate the efficiency of the calorimeter.

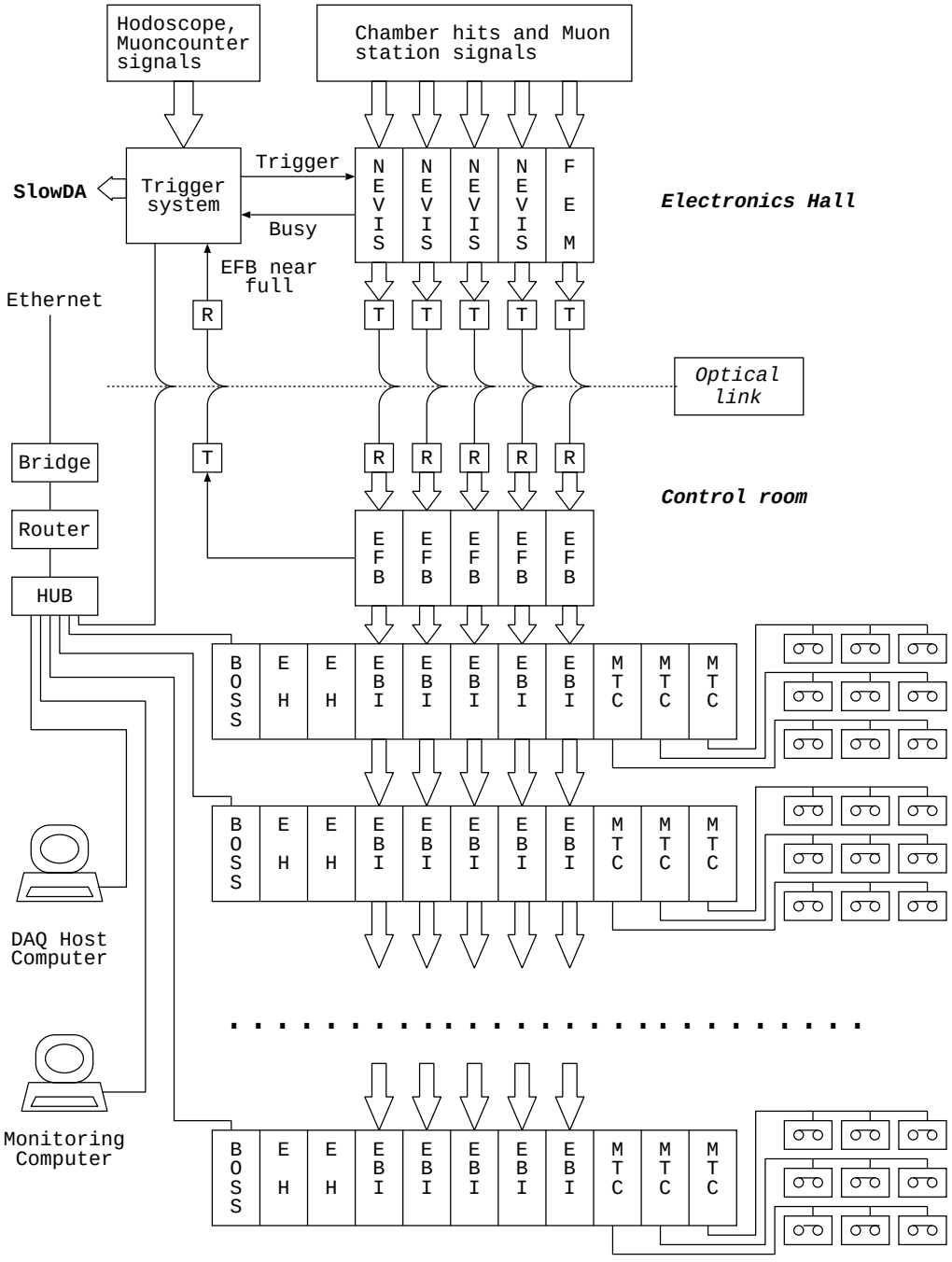


Figure 2.9: Block diagram of data acquisition system used in 1997.

## 2.8 Data Acquisition

Figure 2.9 shows the structure of the fast data acquisition system (fast DAQ). The design of the system [31] was an adaptation of the data acquisition system used in experiment E791 at Fermilab [32]. For an event satisfying at least one trigger, the information from the various detector elements was readout by five paths that were carefully balanced to ensure optimal parallelism of the system. Because the control room was located about 160 m from the electronics hall the data were transmitted in parallel using five optical fibers, each capable of transmitting information at a rate of 1 Gbit/s. At the end of the optical link in the control room, the optical signals were converted back to electrical data which were subsequently stored in five memory FIFO buffers. Each buffer contained 192 MB of SRAMs serving as pipeline as the data acquisition system built events and recorded them to tape.

The data from the buffers were sent to five event-building systems working in parallel. Each event-building system was housed in a 6U VME crate and consisted of three VME single-board central processing units (SBCs), five event-buffer interfaces (EBI), and three SCSI host adapters. One of the SBC controlled, scheduled and monitored the event-building system. The other two SBCs were responsible for building the event from the five event fragments. The event fragments belonging to an event were verified using an eight-bit event synchronization number (ESN) that were generated and attached to each event fragment. The EBIs were used to access the data in the buffers and passed them to the SBCs. Each SCSI host adapters controlled three EXB-8505 tape drives, each capable of reading and writing at a maximum rate of 500 KB/s in uncompressed mode. Therefore, a single VME crate could record data to a maximum of nine tape drives. In the 1997 run, only eight were used. The data acquisition system was controlled and monitored by two host computers.

The average event size was about 600 bytes. The data acquisition system was able to achieve a maximum sustained throughput of about 16 MB/s, corresponding to a maximum trigger rate of 84 kHz and a live time of about 65% as measured by the ratio of accepted triggers to generated triggers. Typically, the experiment took data at a rate of about 63 kHz, and recorded data to tape at a sustained throughput of 12 MB/s. The average live time was around 75%. The deadtime of the system, dominated by the readout system, was about 3 $\mu$s per event.

In addition, integrated and monitoring information such as scalers, beam-line infor-

| Trigger | Non-polarized Data ( $\times 10^9$ ) | |
|---|---|---|
| | Positive | Negative |
| CAS | 22.3 | 11.0 |
| K | 30.8 | 14.4 |
| Total | 43.3 | 18.8 |

Table 2.3: Summary of collected triggers.

mation, magnetic field and temperatures of magnets were recorded spill-by-spill with a separate data acquistion system (slow DAQ) based on standard CAMAC and GPIB instruments. The slow DAQ consisted of multiple CAMAC crates. The longest distance between two crates was about 60 m that necessitated the use of the CAMAC Serial Highway. The system was controlled by the DAQ host computer through a SCSI-Serial CAMAC interface. The slow DAQ obtained the beam-line information from the FNAL beam-line servers. All the data from the slow DAQ were recorded on a hard disc connected to the DAQ host computer.

## 2.9 Data Collection

Physics data were recorded between April 1997 and September 1997. The duration of a run was the time it took to fill all 40 Exabyte tapes, typically about six hours. Transport of the secondary beam was frequently changed between positive and negative modes to minimize any time-dependent systematic effect. Since the production cross-section of $\Xi^-$ is greater than that of $\bar{\Xi}^+$, the run cycle was made up of two positive runs followed by a negative run. Therefore, there was about twice as much positive data as negative. In addition, some polarized hyperon data were taken by targeting at non-zero production angle.

Out of a total of 62.1 billion non-polarized events written to about 9,000 data tapes, 43.3 billion events were taken with a positive secondary beam and 18.8 billion events in the negative runs. A summary of the triggers collected is given in Table 2.3. Because of time constraint, only about 60% of the non-polarized positive data and 40% of the non-polarized negative data were analyzed for this thesis.

# Chapter 3

# Data Reduction

In this chapter, processing of the data is described. The algorithms used to select the candidate events are explained. The criteria for selecting the final data sample are described and justified. Variations and the characteristic of the events are examined.

## 3.1 First Pass

In the first stage of data reduction, the raw data on tape was processed with an event reconstruction code to select events suitable for studying CP symmetry in the $\tau$ decay of charged Kaon. Figure 3.1 is a flow chart showing how the raw data is processed. The reconstruction code consists of track finding, event selection, and a global geometric fit of the candidate events.

In the experiment, digitized hits were produced by tracks tranversing the MWPCs. From these hits, the space-points or the $X-Y$ coordinates of the positions where the tracks crossed the planes of the MWPCs were found. Using these space-points, 3-dimensional tracks were reconstructed. The details of the track-finding algorithm is described in Appendix A. Figure 3.2 shows the probability of finding a certain number of reconstructed tracks for a typical sample of raw data from the positive and negative runs. On average there were slightly more tracks found in the negative runs.

After all tracks were found, events with at least one opposite-sign (OS) track and at least two same-sign (SS) tracks were kept. Each track was assumed to be a charged $\pi$. Any candidate with a $3\pi$ invariant mass that fell within $\pm 100$ MeV/c$^2$ from 0.4937 GeV/c$^2$ [14] was tagged as a Kaon candidate. Figure 3.3 shows the probability distributions of the

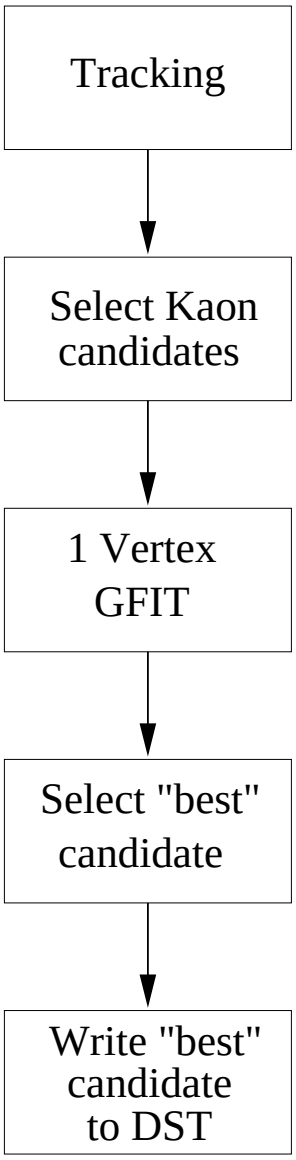


Figure 3.1: Flow chart of first pass of raw data.

reconstructed track multiplicity of Kaon events for the same data samples as in Figure 3.2.

Even though we have all the parameters of a track (slopes and intercepts of the upstream and downstream track segment) from the track-finding process, better estimation of these parameters can be obtained by using a constrained fit that reflects the topology in the $\tau$ decay of a charged Kaon. The topology involves a single vertex, and three tracks segments. Since the fit is purely geometric, we call it a single-vertex geometric fit (GFIT1V) and is described in detail in Appendix B. GFIT1V was performed on each Kaon candidate.

In some occasion, the candidate did not conform to the topology of the fit. As a result the fit did not converge and the candidate was rejected. In addition, sometimes an event could contain more than one OS track and/or more than two SS tracks. In this case, due to the combinatorial, there could be more than one Kaon candidates passing GFIT1V. Figure 3.4 shows the probability distribution of the number of Kaon candidates in an event for the positive and negative runs. As shown in Figure 3.4, only about 6% of the Kaon candidate events have more than one candidate. If there was more than one Kaon candidate in the event, the following criteria was used to select the "best" candidate from the surviving GFIT1V candidates:

- For each candidate, a likelihood was calculated as the joint probability of the reconstruted $3\pi$ invariant mass and the chi-square $\chi^2$ from GFIT1V.

$$\mathcal{L} = \mathcal{P}_{mass} \cdot \mathcal{P}_{\chi^2} \tag{3.1}$$

  where $\mathcal{P}_{mass}$ is given by a Gaussian probability density function,

$$\mathcal{P}_{mass}(x;\mu,\sigma^2) = \frac{1}{\sigma\sqrt{2\pi}} e^{\frac{-(x-\mu)^2}{2\sigma^2}} \tag{3.2}$$

  where $\mu = 0.493677$ GeV/c$^2$ and $\sigma = 0.002$ GeV/c$^2$. The value of $\sigma$ was determined from reconstructed Monte Carlo events (see Figure B.4). The function $\mathcal{P}_{\chi^2}$ is given by

$$\mathcal{P}_{\chi^2}(z;n) = \frac{z^{n/2-1}e^{-z/2}}{2^{n/2},\ (n/2)} \tag{3.3}$$

  where $n$ is the number of degrees of freedom.

- The "best" candidate was the one with the largest value for $\mathcal{L}$.

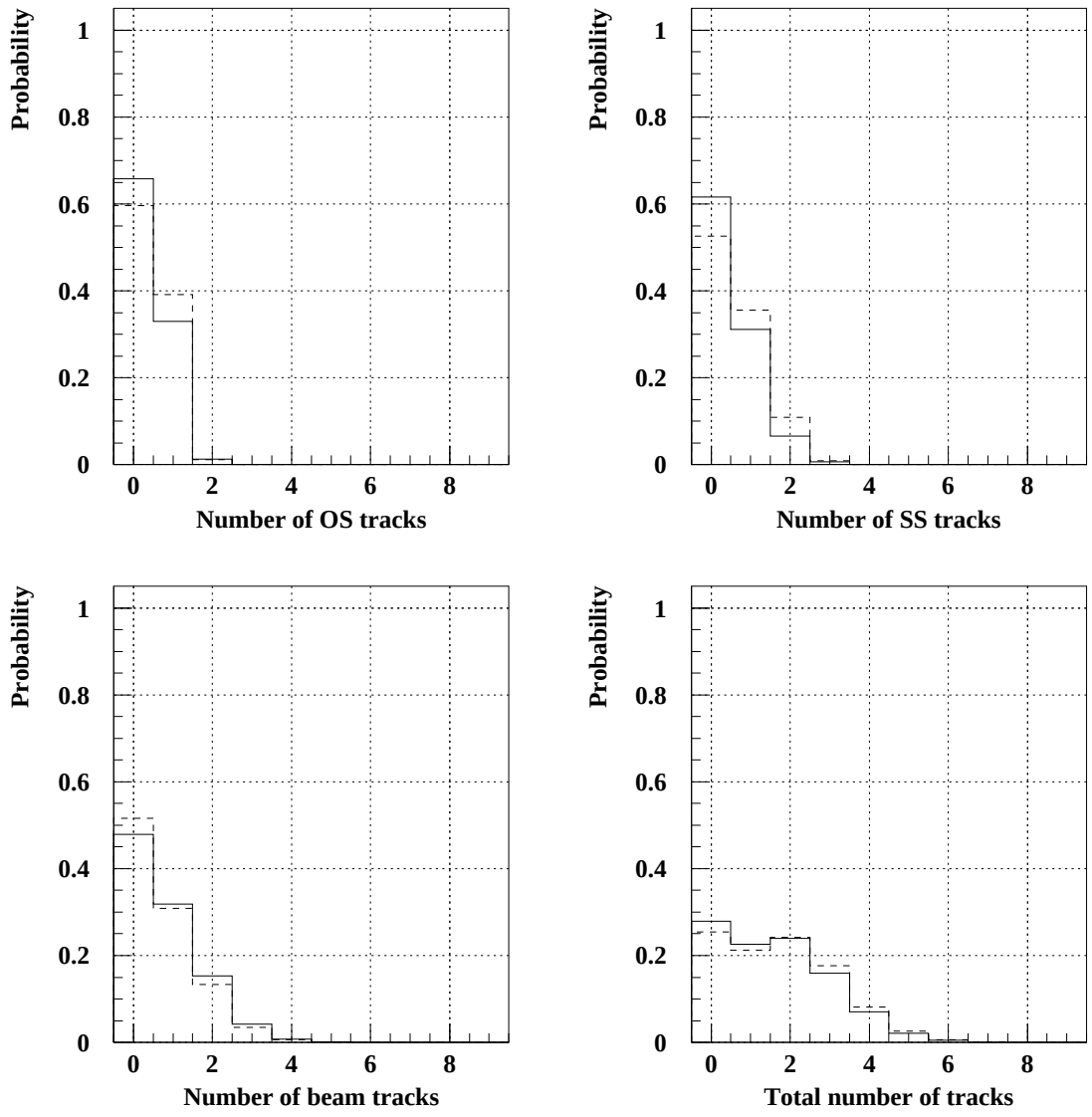


Figure 3.2: Probability distributions of multiplicity of reconstructed tracks for a typical sample of raw data from all trigger components for positive (solid) and negative (dash) runs. The average proton beam intensities for the positive and negative data were about $1.43 \times 10^{11}$ protons/spill and $1.35 \times 10^{11}$ protons/spill respectively. The probability distributions for reconstructed OS tracks, SS tracks, beam tracks, and total tracks are shown. The statistical errors are small and are not visible in the plots.

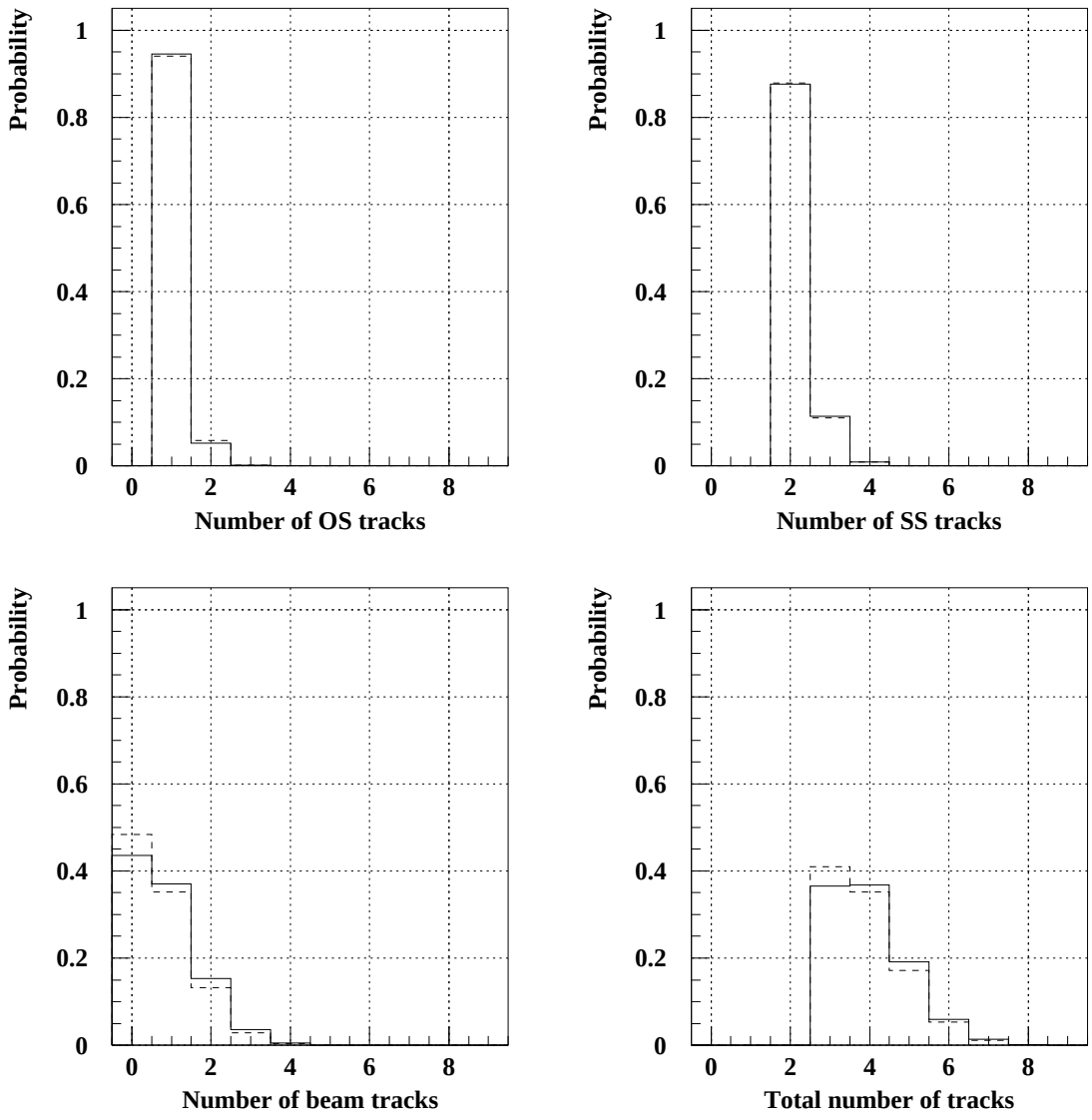


Figure 3.3: Probability distributions of multiplicity reconstructed tracks for Kaon events in the first pass for positive (solid) and negative (dash) runs. The average proton beam intensities for the positive and negative data were about $1.43 \times 10^{11}$ protons/spill and $1.35 \times 10^{11}$ protons/spill respectively. The probability distributions for reconstructed OS tracks, SS tracks, beam tracks, and total tracks are shown. The statistical errors are small and are not visible in the plots.

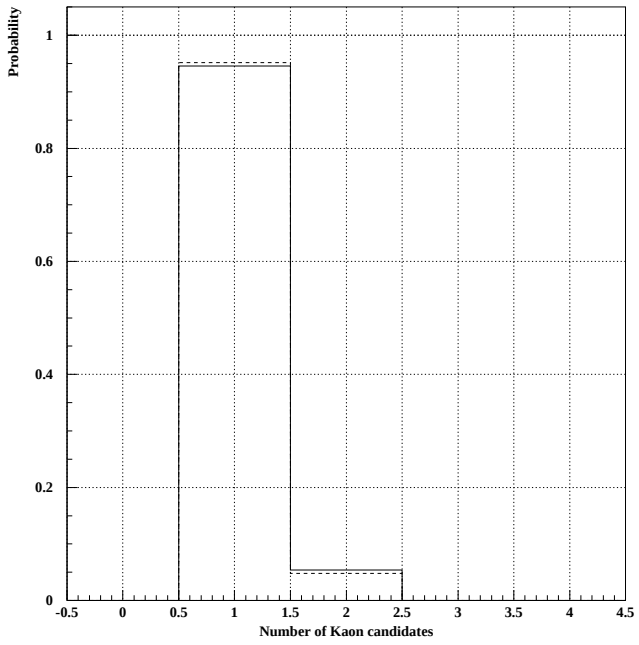


Figure 3.4: Probability distribution of number of Kaon candidates in an event for positive (solid) and negative (dash) runs. Events with more than one Kaon candidates is assigned a value 2.

| DST word descriptions | Number of words (4 bytes/word) |
|---|---|
| Trigger bits | 5 |
| ADC data | 4 |
| Slopes and intercepts of downstream tracks | 12 |
| Momentum of tracks before GFIT1V | 9 |
| Momentum of tracks after GFIT1V | 9 |
| Decay vertex from GFIT1V | 3 |
| One of the beam momentum if any | 3 |
| Slopes and intercepts of downstream beam tracks | 4 |
| Tracks hit pattern | 4 |
| Number of OS tracks | 0.25 |
| Number of SS tracks | 0.25 |
| Number of beam tracks | 0.25 |
| Number of hits used in GFIT1V | 0.25 |
| Number of hits in each wire plane | 8 |
| GFIT1V $\chi^2$ | 1 |
| $\mathcal{L}$ from second Kaon candidate if any | 1 |
| Total number of words | 64 |

Table 3.1: Contents of an event on DST.

### 3.1.1 Data Summary Tapes (DST)

The "best" Kaon candidate events from the first pass were recorded on Exabyte tapes for later stage of processing. These tapes are called Data Summary Tapes. Each DST events contained information obtained from the first pass that were labeled as the DST block of the event. The contents of the DST block are listed in Table 3.1. Two sets of Kaon DST tapes called stream 3 and stream 6 were output. Stream 3 contained both the raw data and the DST block. On the other hand, stream 6 contained only the DST block. The raw data were also recorded just in case that we require information from the raw data in the later stage of analysis.

In addition to the Kaon DST tapes, there were another set of DST tapes on which only the raw data of the events with at least one OS track and at least two OS tracks were recorded. This set of DST tapes is called stream 2. Clearly, the Kaon DST tapes is a subset of the stream 2 DST tapes. The number of stream 2 tapes was approximately 10% of the number of the raw data tapes, a significant reduction of the number of events in the first pass.

## 3.2 Second Pass

The second pass processed data on the stream 2 DST tapes. The MWPC alignment that was used in the track-finding process of the first pass did not include the rotations of the MWPCs about the X-axis and Y-axis. In the second pass, all the MWPC rotations were included in reconstructing events on stream 2. As in the first pass, Kaon DST tapes were output as well. There were 188 million events in 121 positive runs and 104 million events in 62 negative runs.

## 3.3 Third Pass

The third pass of the data operated on 28 stream 6 tapes created in the second pass. This stage consisted of correcting the momenta of the tracks with the magnetic field readings from the Hall probes in the BM109s, selecting preliminary good Kaon candidates, measuring the wire efficiencies of the MWPCs, measuring the efficiencies of the trigger counters, and measuring the efficiency of the calorimeter trigger. All the measurements were done on a run-by-run basis.

### 3.3.1 Momentum Correction with Hall Probes Readings

As described in Appendix A, the momenta of the tracks were calculated with a single bend-plane approximation using a fixed kick. Because it would be too time consuming to trace the trajectories of each track through the analysis magnet using the full knowledge of the magnetic field, the single bend-plane approximation was used. This approach is further justified by the fact that any biases resulting from the appoximation would be the same for the positive and negative data and would cancel out in the asymmetry measurement. However, we can correct for the variation of the absolute scale of the kick using the readings from the Hall probes. This variation can be due to a variation in the current of the analysis magnet caused by temperature fluctuation and other parasitic variations. In addition, even though care was taken to minimize any hysteresis effect in the magnet when switching between positive and negative runs, the procedure might not be perfect. Thus, correcting the momentum with the Hall probe readings would be necessary. Figures 3.5 and 3.6 show the significance of this correction. In the top plot of each figure, the $3\pi$ invariant mass distributions of two large samples of good positive Kaon candidates are superimposed. In

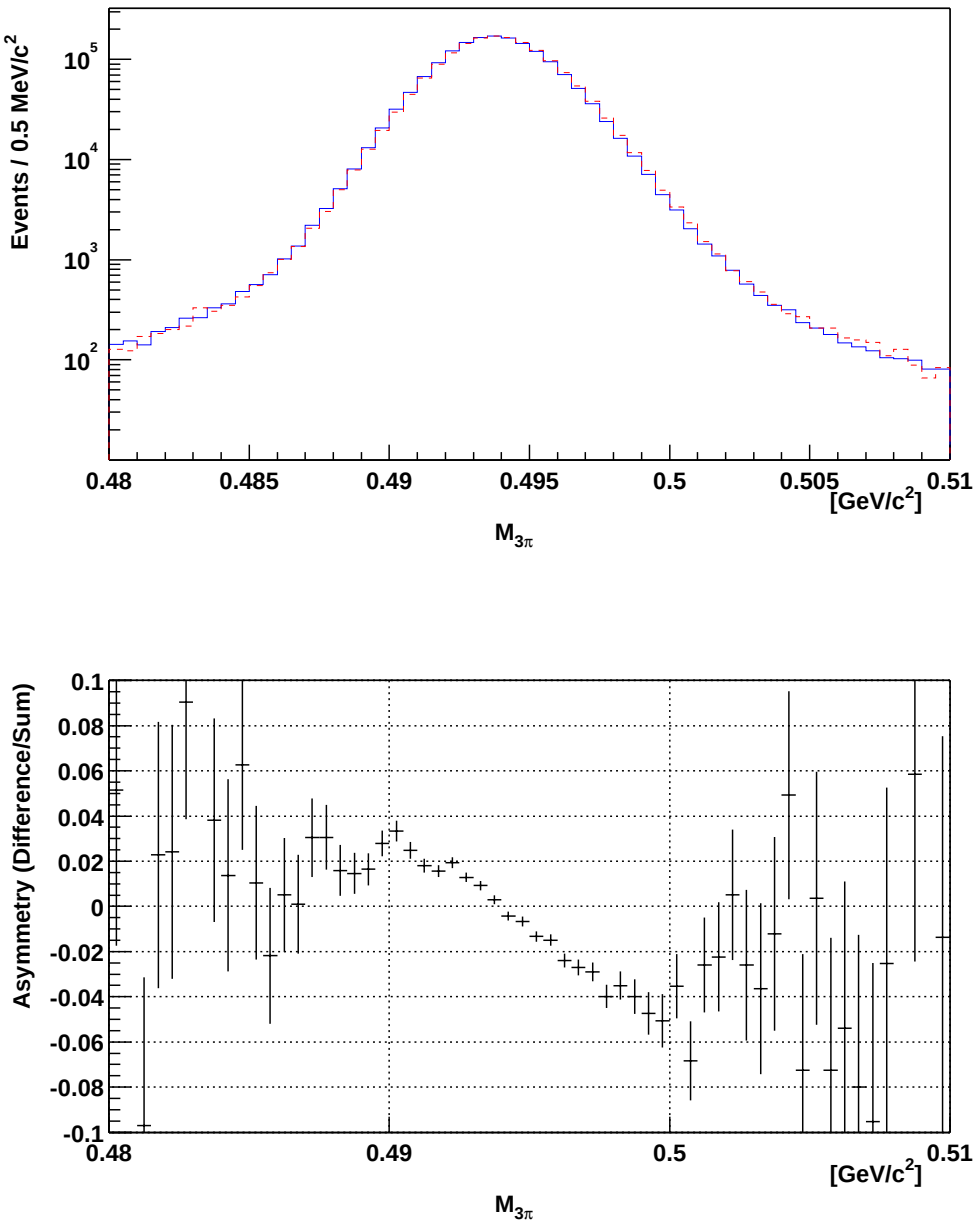


Figure 3.5: Comparison of $3\pi$ invariant mass distribution for two samples of good positive Kaon candidates. Momenta of the tracks did not include correction from the Hall probe readings. The top plot shows the superposition of the distributions. The bottom plot shows the asymmetry of the distributions.

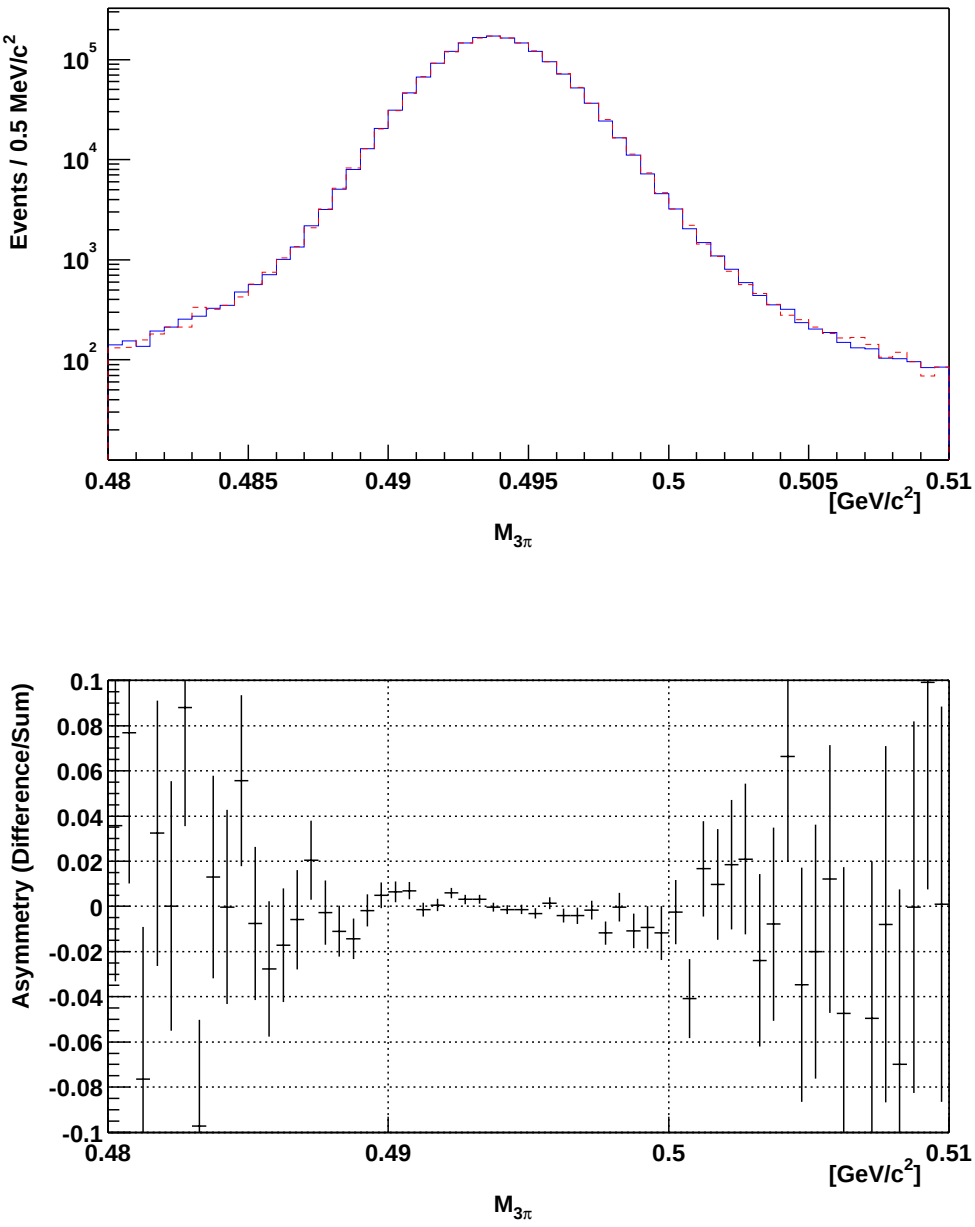


Figure 3.6: Comparison of $3\pi$ invariant mass distribution for two samples of good positive Kaon candidates. Momenta of the tracks included correction from the Hall probe readings. The top plot shows the superposition of the distributions. The bottom plot shows the asymmetry of the distributions.

| Cuts |
|---|
| exclude 1.318 GeV/c$^2$ $< m_{\Lambda\pi} <$ 1.326 GeV/c$^2$ |
| GFIT1V $\chi^2_{DF} < 2.5$ |
| 115 GeV/c $< p_K <$ 255 GeV/c |
| 0.484 GeV/c$^2$ $< m_{3\pi} <$ 0.504 GeV/$c^2$ |
| -50 cm $< z_{decay} <$ 1350 cm |
| -1.2 cm $< x_{collimator} <$ 1.2 cm |
| -0.8 cm $< y_{collimator} <$ 0.8 cm |
| -0.35 cm $< x_{target} <$ 0.35 cm |
| 0.15 cm $< y_{target} <$ 1.05 cm |

Table 3.2: Cuts used for selecting preliminary good Kaon candidate in the third pass.

the bottom plot, the asymmetry of the distributions is shown. The asymmetry is defined as the difference in the number of events in a given bin in the two histograms divided by the sum. Figure 3.5 shows the distributions without the correction from the Hall probes readings. Figure 3.6 shows the distributions after the correction, the asymmetry is signicantly reduced. However, a small residual asymmetry still remains after the correction. This residual asymmetry corresponds to a difference in kick of about $2 \times 10^{-4}$ GeV/c, which in turn corresponds to a difference in the magnetic field of about $1.7 \times 10^{-4}$ T in each of the analysis magnet. This number is approximately the precision of the Hall probes. We will study the systematic effect due to this asymmetry in the analysis section.

### 3.3.2 Preliminary Selection of Good Kaon Candidate

A number of criteria was used to select events that were qualified as good Kaon candidate events. This was done to maximize the signal-to-background ratio and to further reduce the number of events from which detail analysis would be performed. The parameters used were $\Lambda\pi$ invariant mass ($m_{\Lambda\pi}$), reduced GFIT1V $\chi^2$ ($\chi^2_{DF}$), momentum of the reconstructed secondary beam ($p_K$), $3\pi$ invariant mass ($m_{3\pi}$), decay vertex Z, projection of the secondary beam track at the exit of the collimator, and projection of the secondary beam track at the target. Table 3.2 summarizes the actual cuts used. Candidate events that passed all the cuts were recorded in run-by-run DST files with each event containing the DST block only. After the cuts, the numbers of events were reduced to 77 million positive events and 24 million negative events. All the DST files occupied about 40 GB of disk space.

Tighter criteria were used in selecting the final Kaon candidates for the analysis. These tighter criteria will be described in Section 3.4.

### 3.3.3 Efficiencies of Detectors

Using events selected with the tighter criteria to be described in Section 3.4, the efficiencies of the MWPCs, hodoscope counters and calorimeter trigger were calculated. The efficiencies between a positive and a negative run were compared to check for any significant difference in the detector performance between the two polarities.

#### Wire Efficiencies of MWPCs

The efficiency of a wire in an MWPC was measured using the hit pattern of the tracks associated with the Kaon candidates. The hit pattern was made up of 32 bits corresponding to the 32 wire planes. For each bit, a binary one represented a hit on the wire plane used for reconstructing the track and a binary zero meant a missing hit. The track was projected to each wire plane and the expected wire number was calculated. The efficiency of a particular wire labeled as $j$ in plane $i$ was calculated as follows:

$$\epsilon_i(j) = \frac{number\ of\ expected\ wire\ number\ j\ with\ the\ bit\ of\ plane\ i\ set\ to\ one}{number\ of\ tracks\ transvering\ plane\ i\ with\ expected\ wire\ number\ j} \qquad (3.4)$$

The wire efficiencies of the MWPCs for a positive run are shown in Figures 3.7, 3.8, 3.9, 3.10, 3.11, 3.12, 3.13 and 3.14. Most of the wires are fairly efficient except around the secondary beam region which has a large particle flux. The difference in the wire efficiencies between a positive and a negative run that were taken 44 days apart are shown in Figures 3.15, 3.16, 3.17, 3.18, 3.19, 3.20, 3.21 and 3.22. The proton intensities and live times for these runs were approximately the same. The differences are fairly small and uniform across the wire plane, the largest difference is around half a percent.

#### Efficiencies of OS Counters

The efficiency of the OS counters was measured using Kaon candidates that satisfied the SSW·CalCas trigger. The OS track associated with the Kaon candidate was projected to the location of the OS hodoscope to determine the counter that the track was expected to transverse. To eliminate any tracking uncertainty, only tracks with projection at least 1 cm away from all four edges of the counter were used in the efficiency measurement. Then the

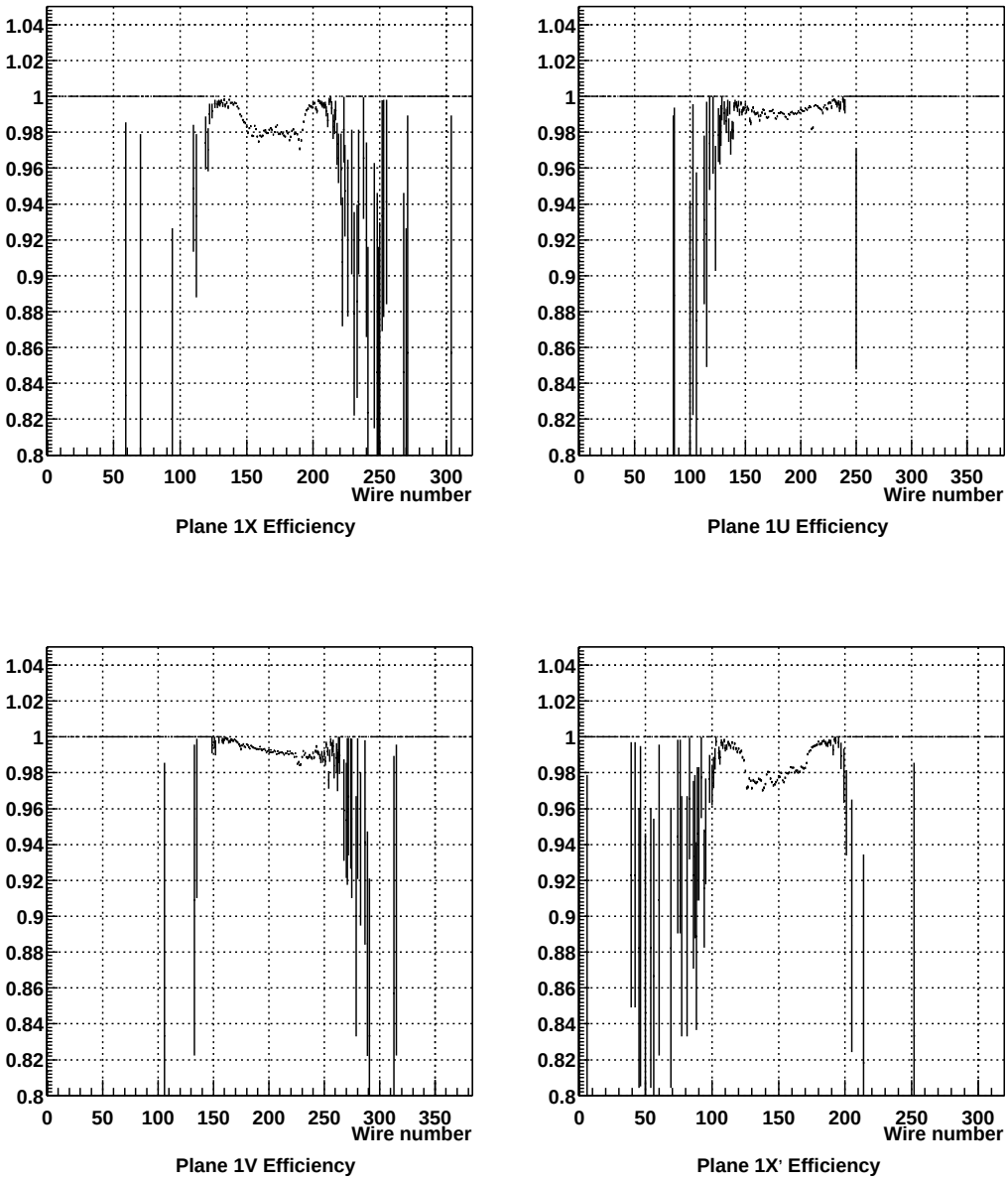


Figure 3.7: Wire efficiency of C1 for positive run 2179.

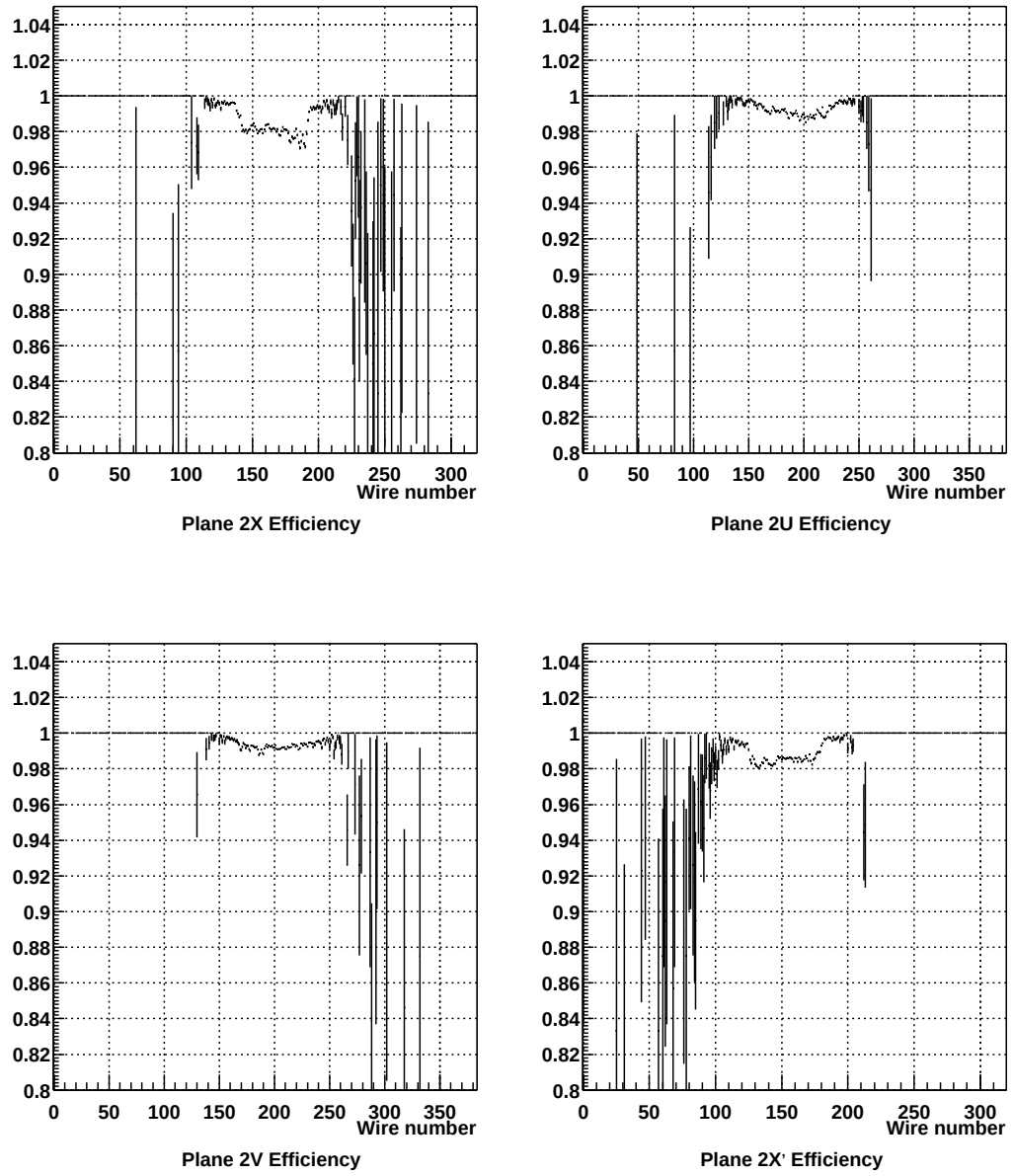


Figure 3.8: Wire efficiency of C2 for positive run 2179.

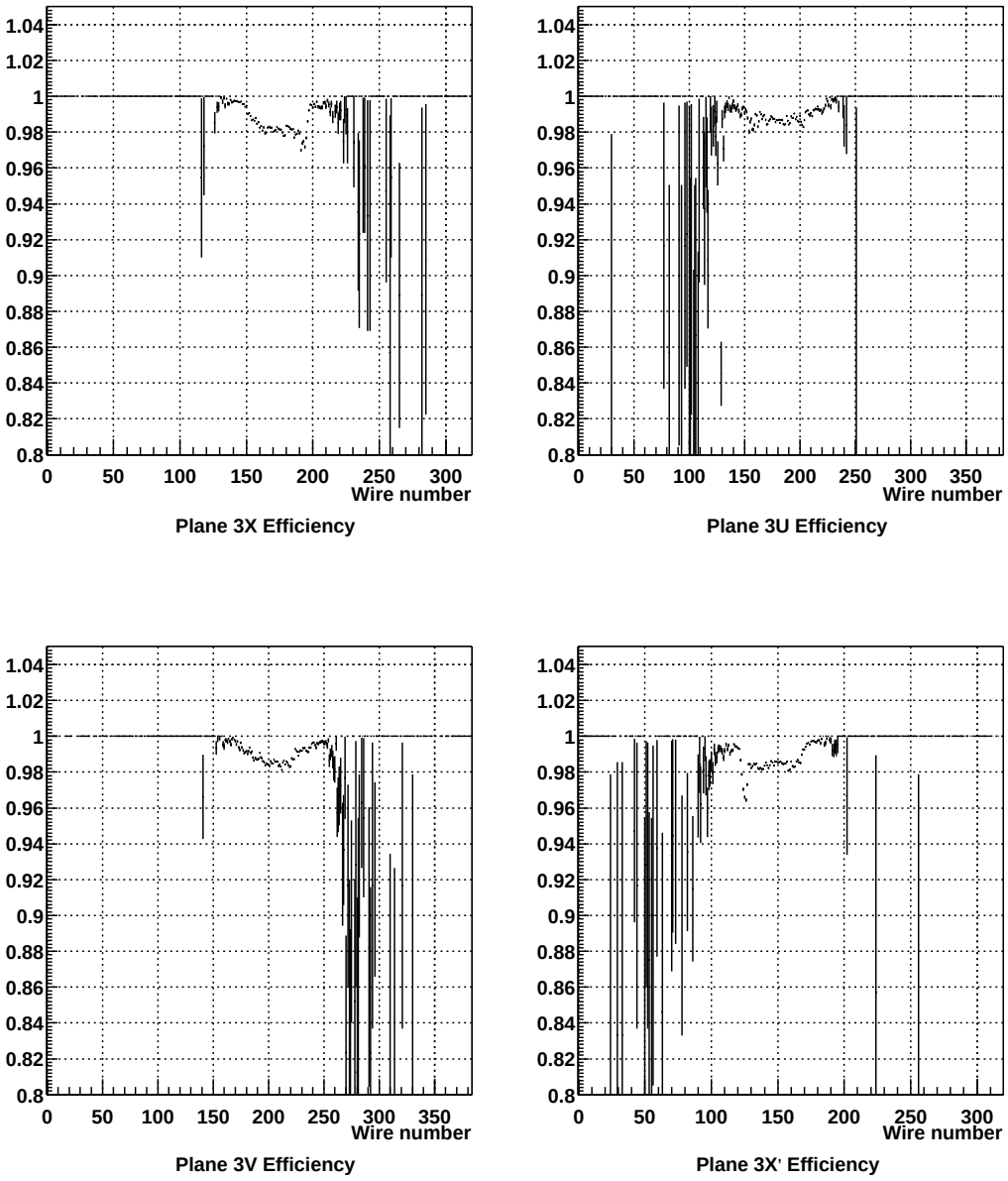


Figure 3.9: Wire efficiency of C3 for positive run 2179.

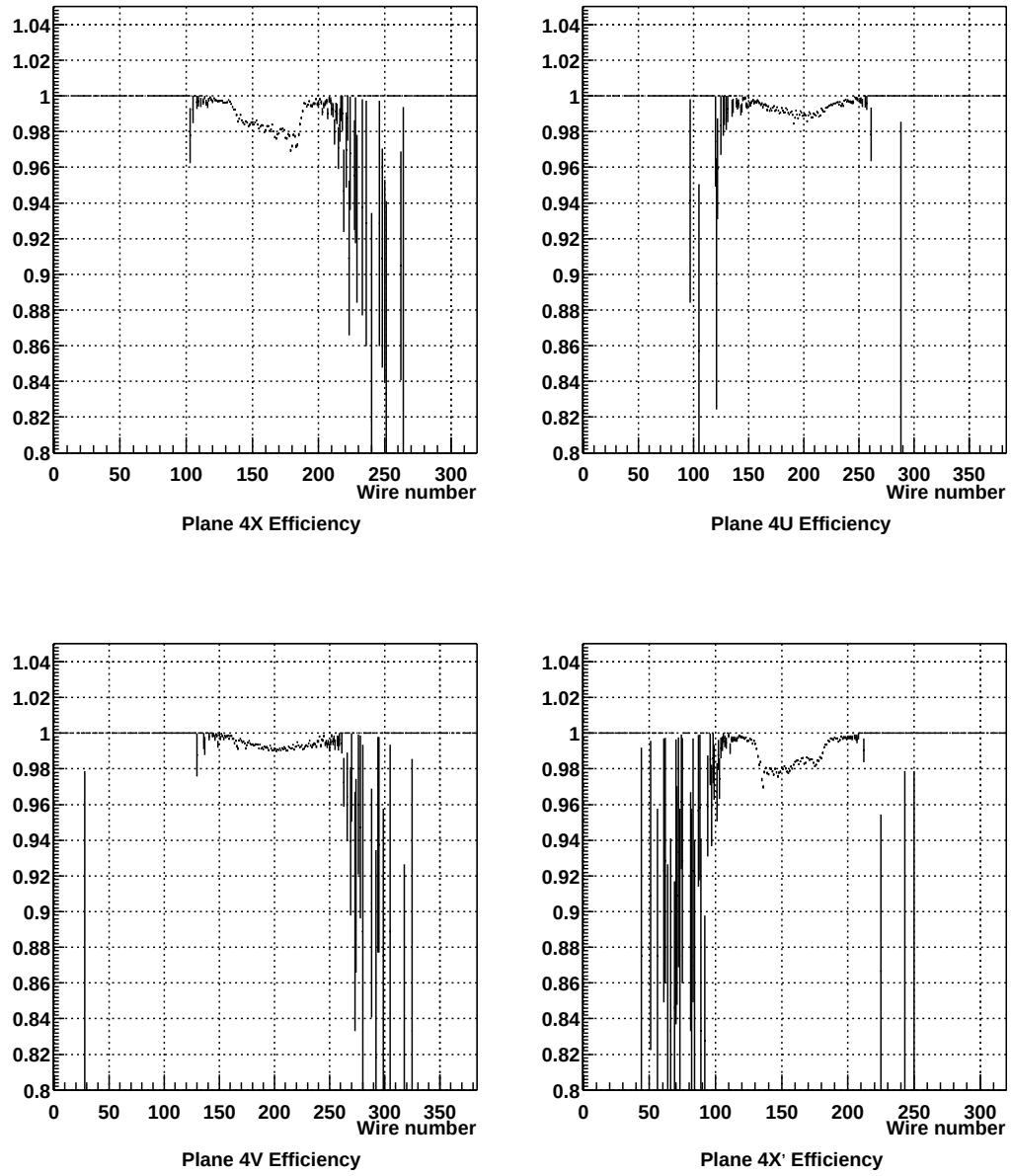


Figure 3.10: Wire efficiency of C4 for positive run 2179.

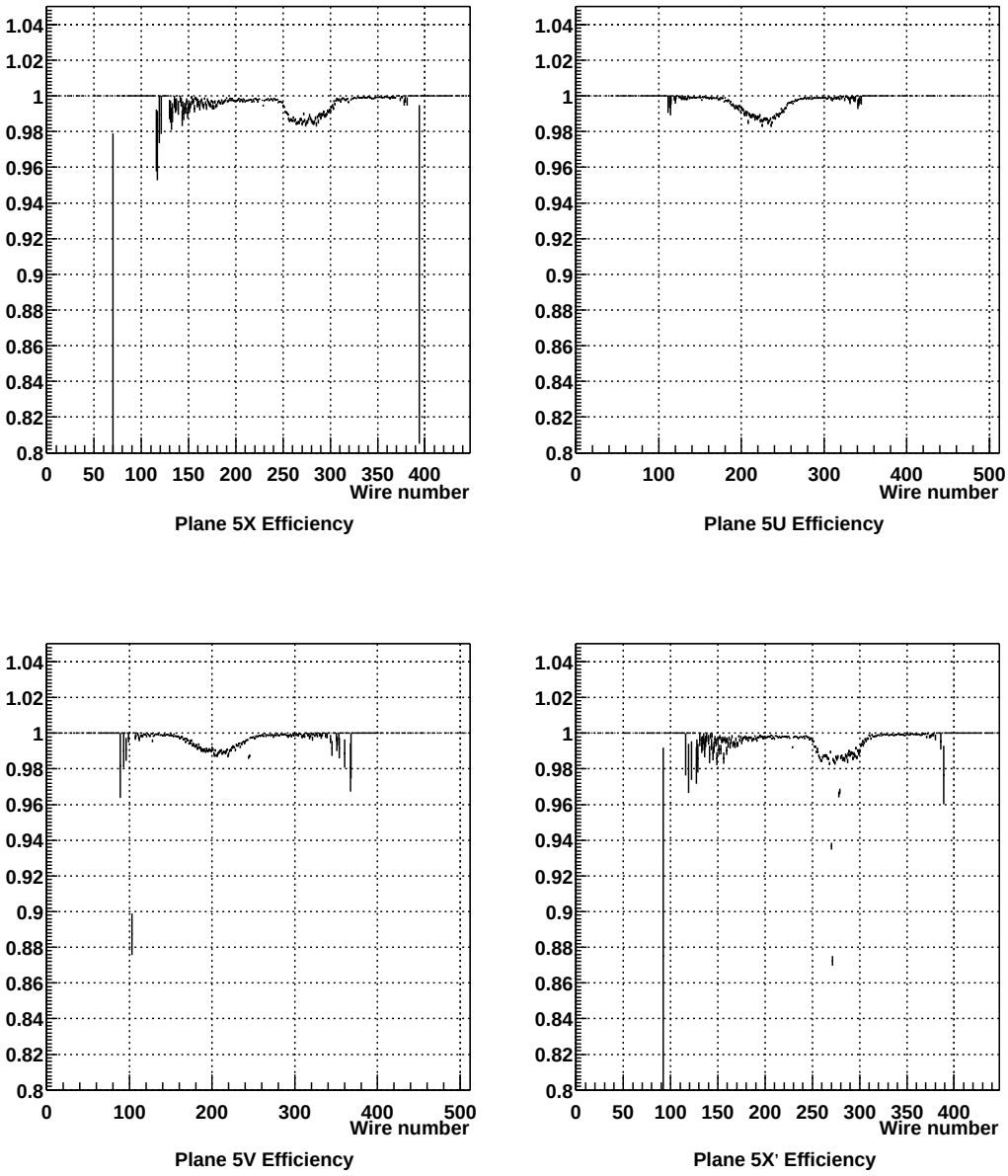


Figure 3.11: Wire efficiency of C5 for positive run 2179.

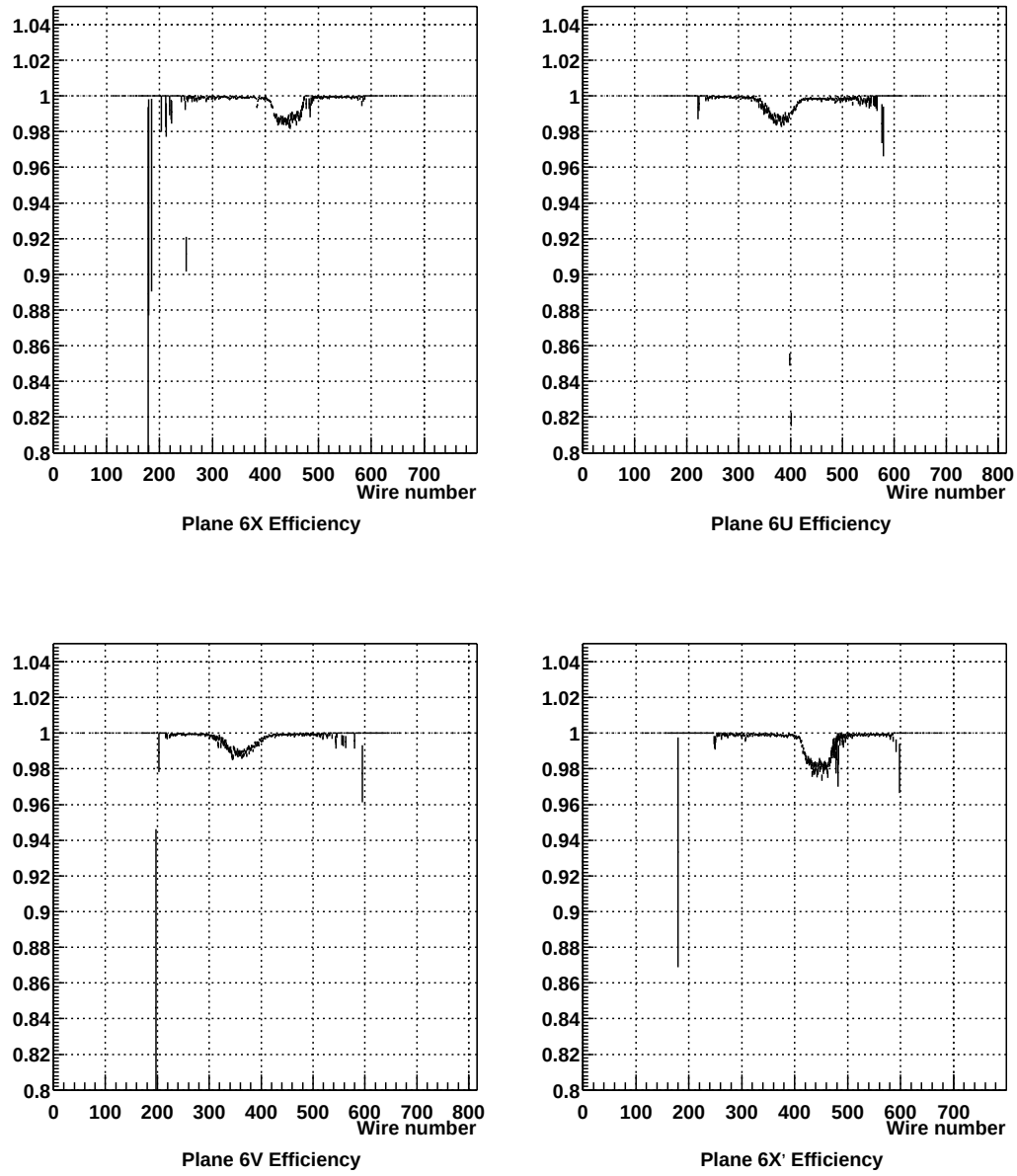


Figure 3.12: Wire efficiency of C6 for positive run 2179.

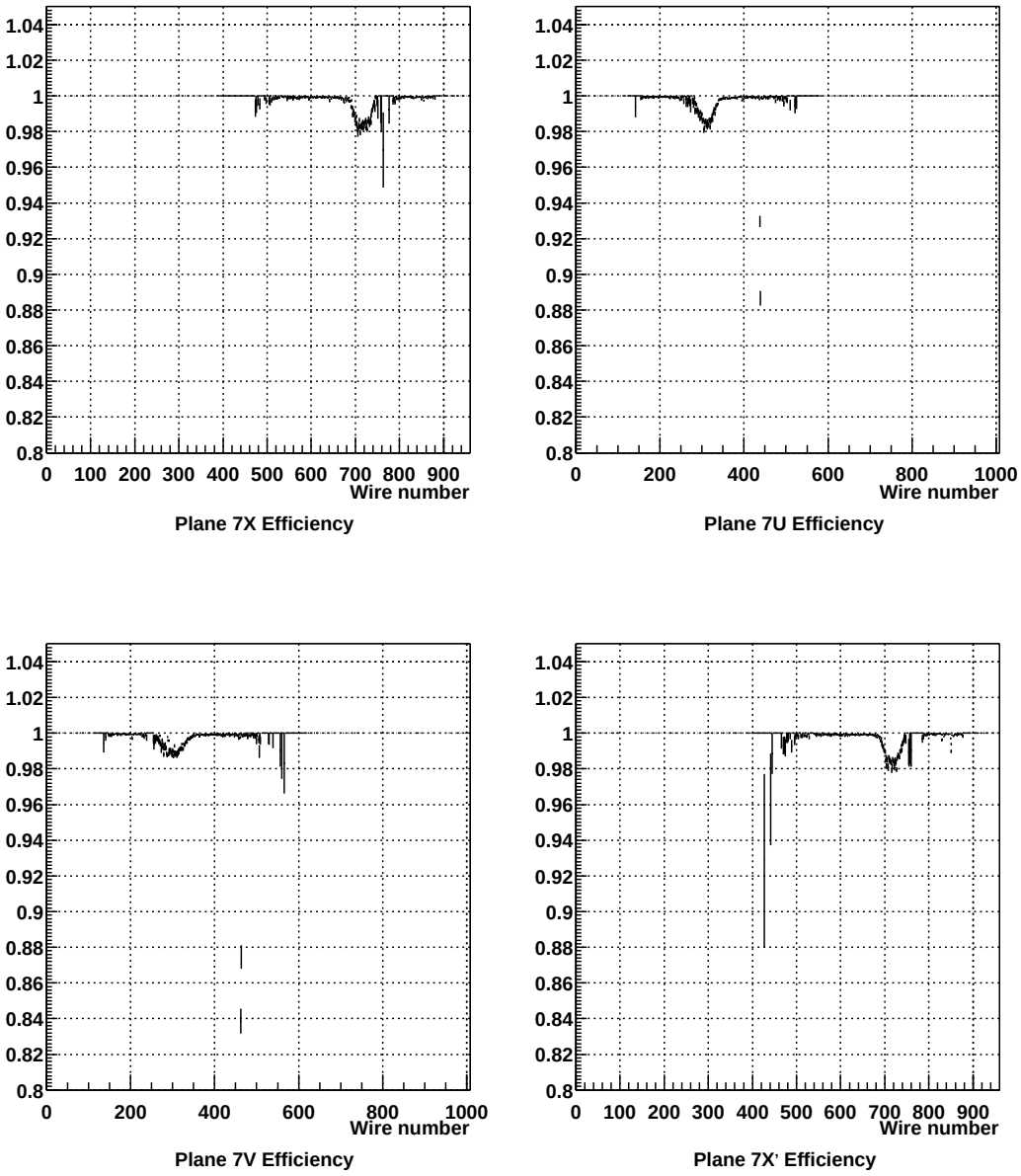


Figure 3.13: Wire efficiency of C7 for positive run 2179.

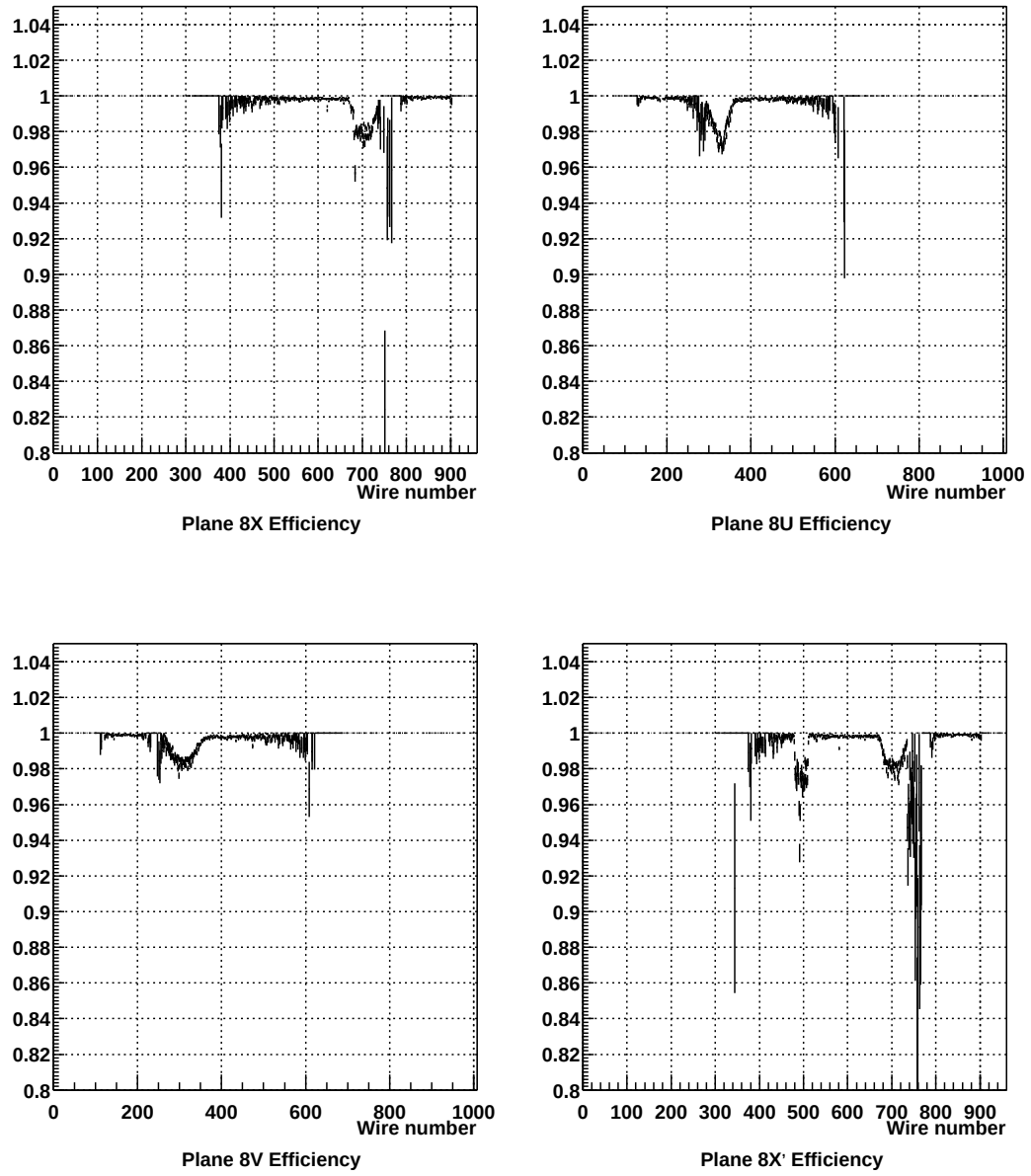


Figure 3.14: Wire efficiency of C8 for positive run 2179.

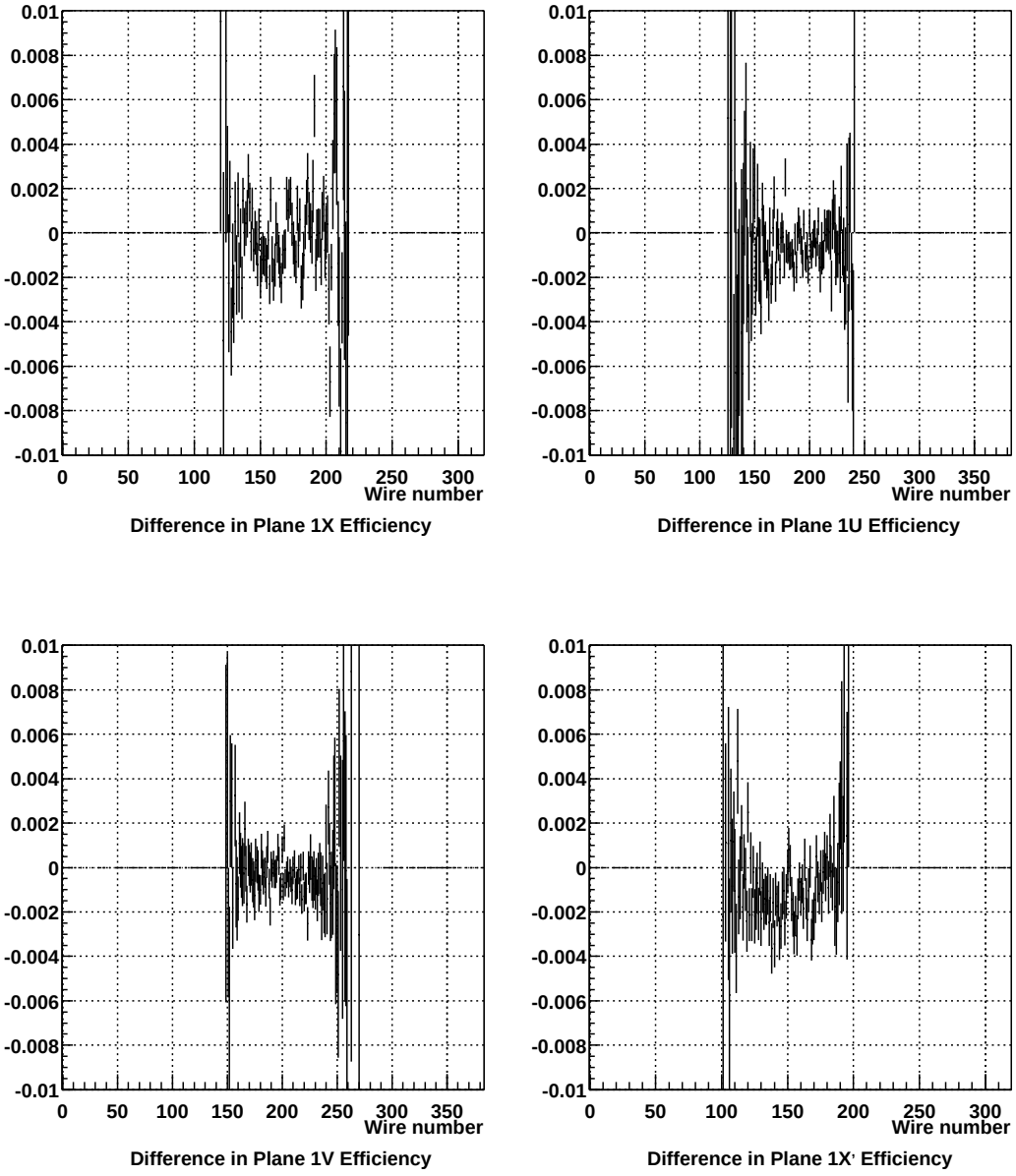


Figure 3.15: Difference in wire efficiency for C1 between positive run 2179 and negative run 2369.

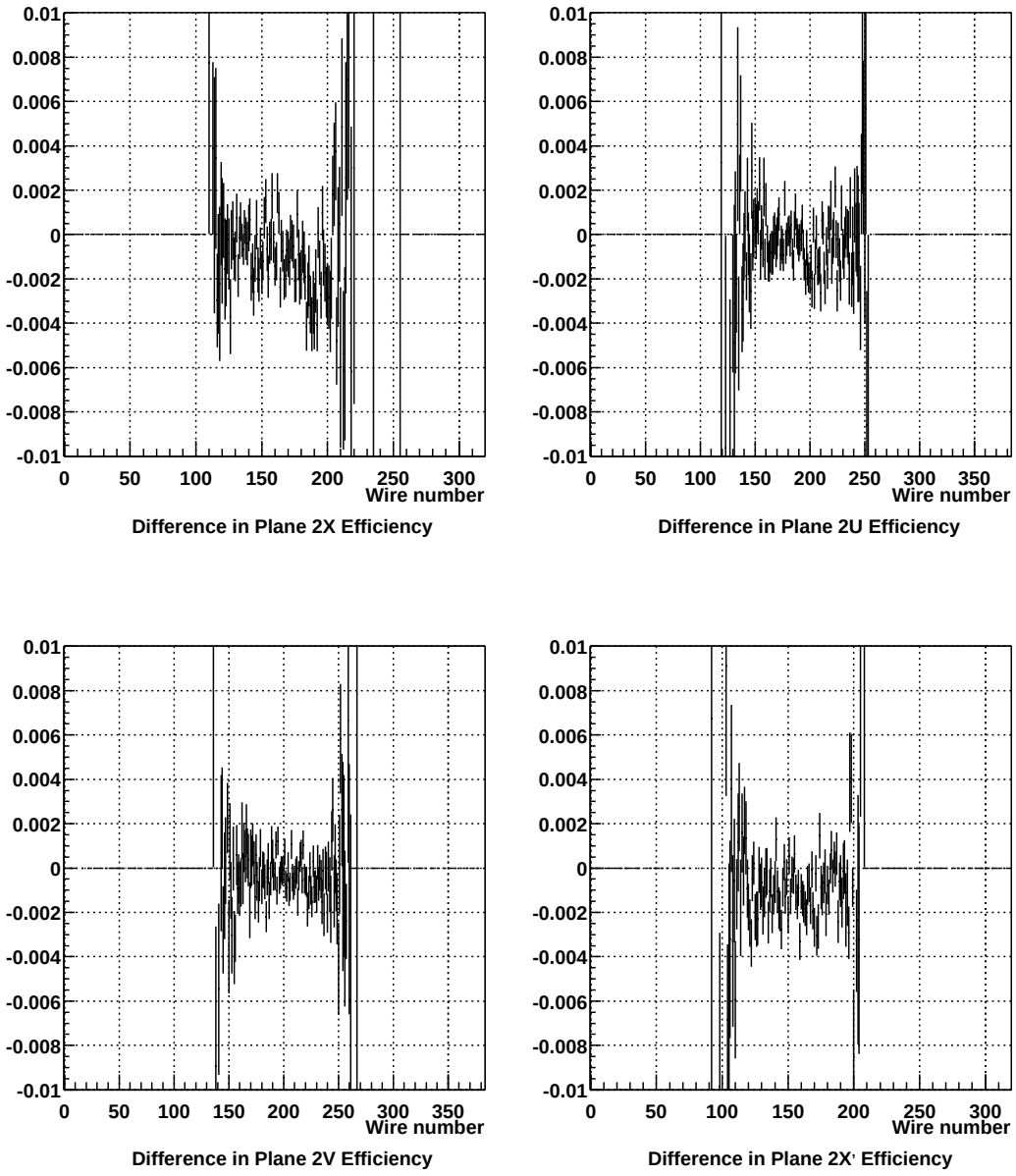


Figure 3.16: Difference in wire efficiency for C2 between positive run 2179 and negative run 2369.

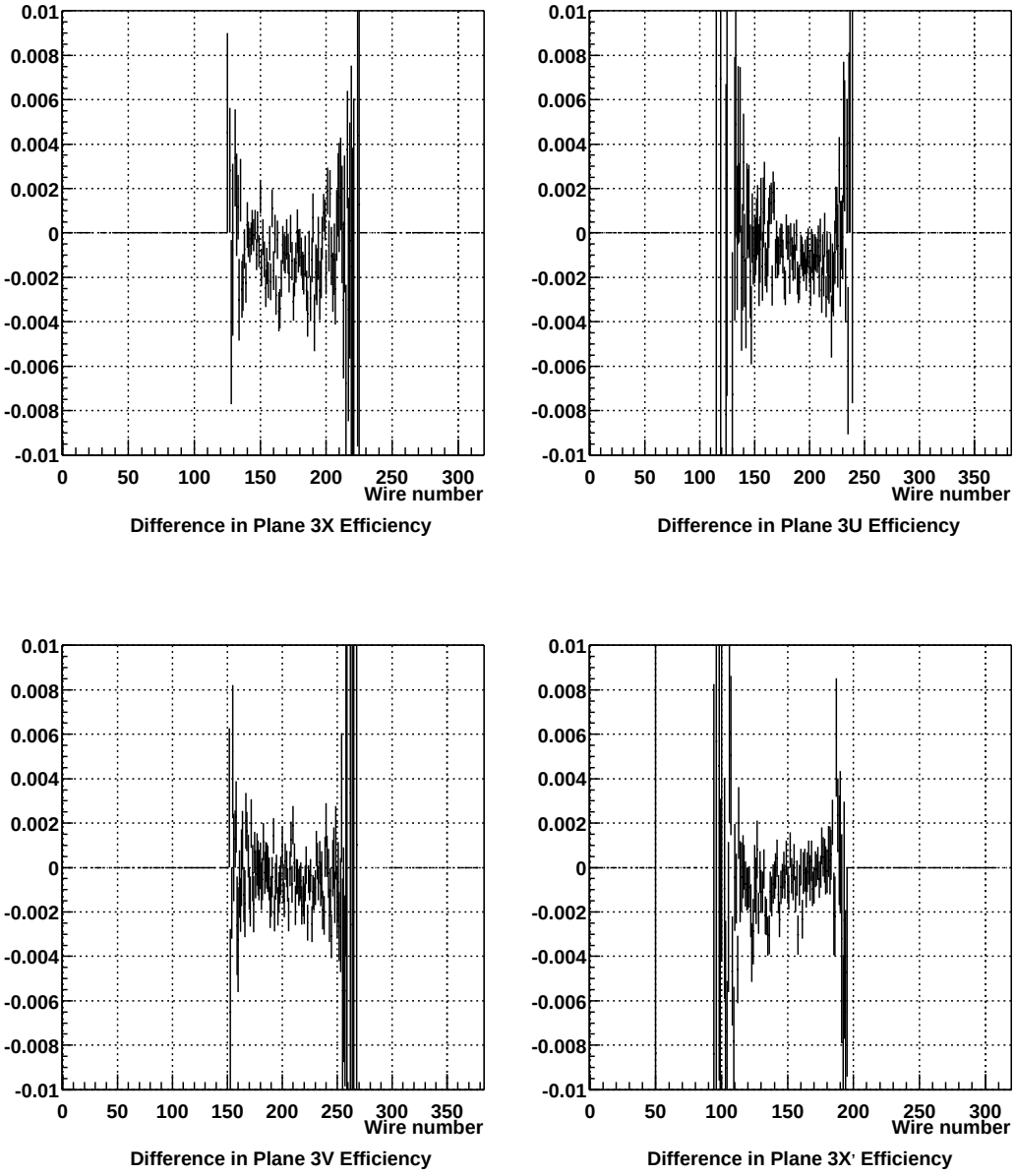


Figure 3.17: Difference in wire efficiency for C3 between positive run 2179 and negative run 2369.

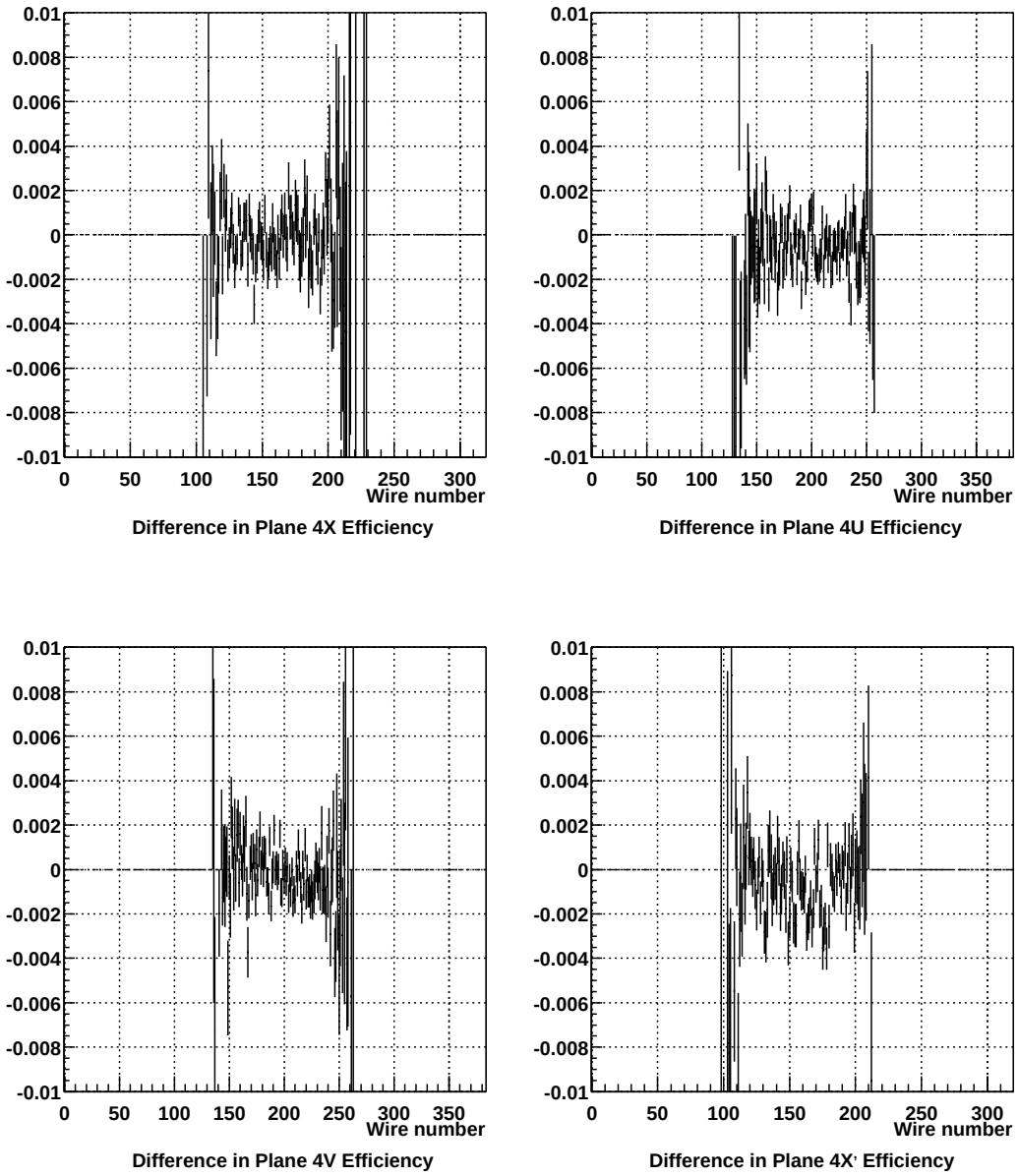


Figure 3.18: Difference in wire efficiency for C4 between positive run 2179 and negative run 2369.

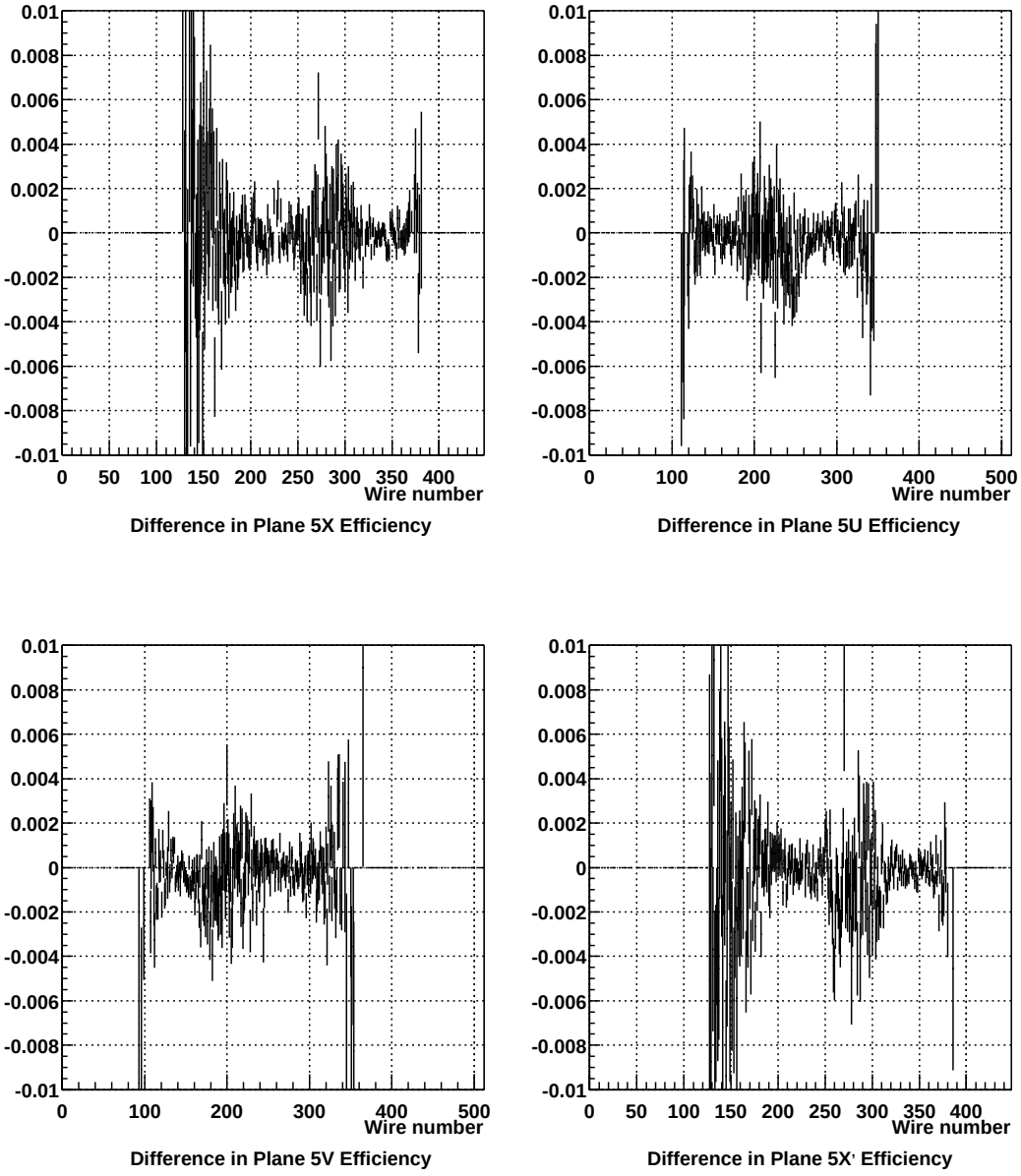


Figure 3.19: Difference in wire efficiency for C5 between positive run 2179 and negative run 2369.

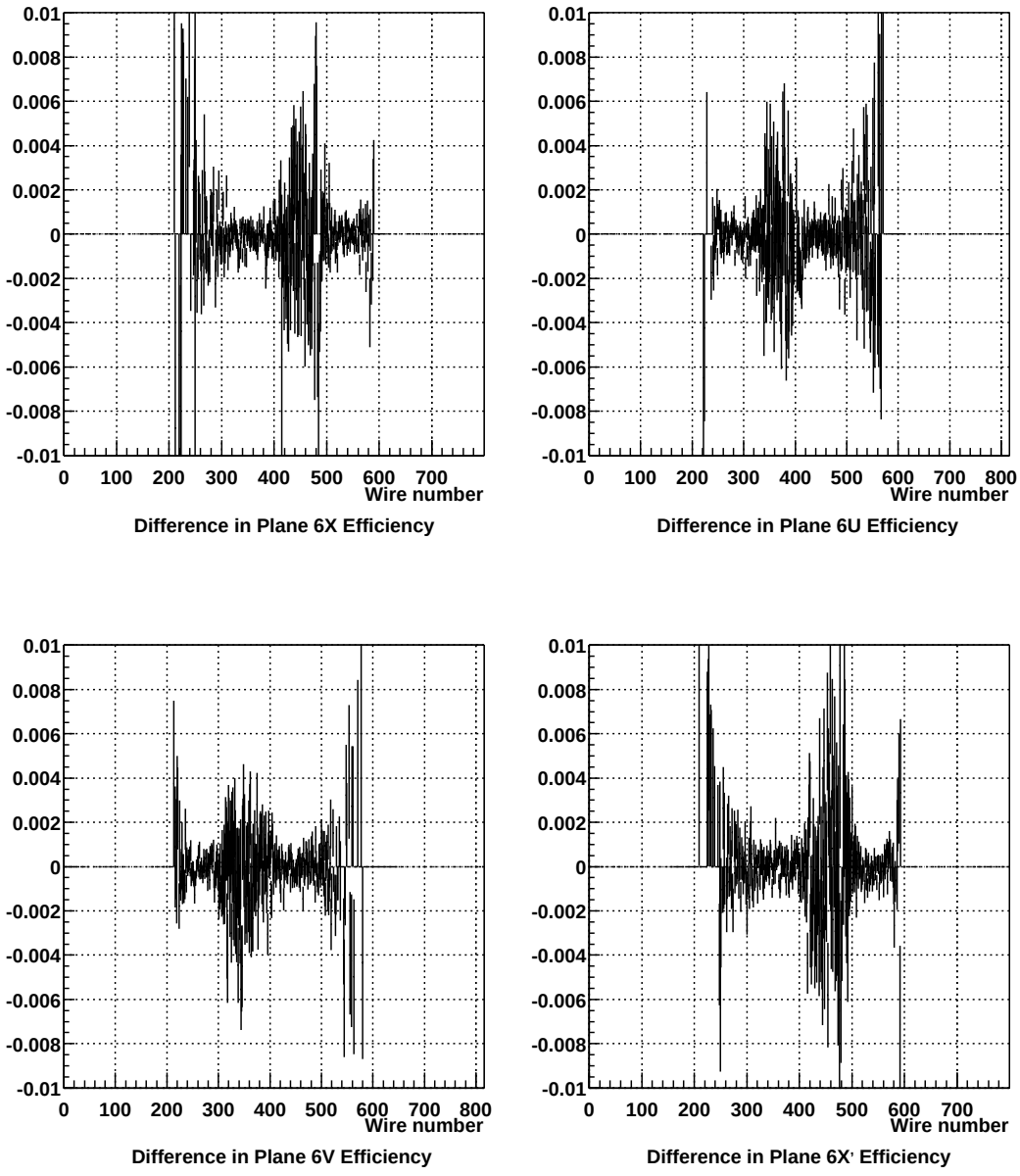


Figure 3.20: Difference in wire efficiency for C6 between positive run 2179 and negative run 2369.

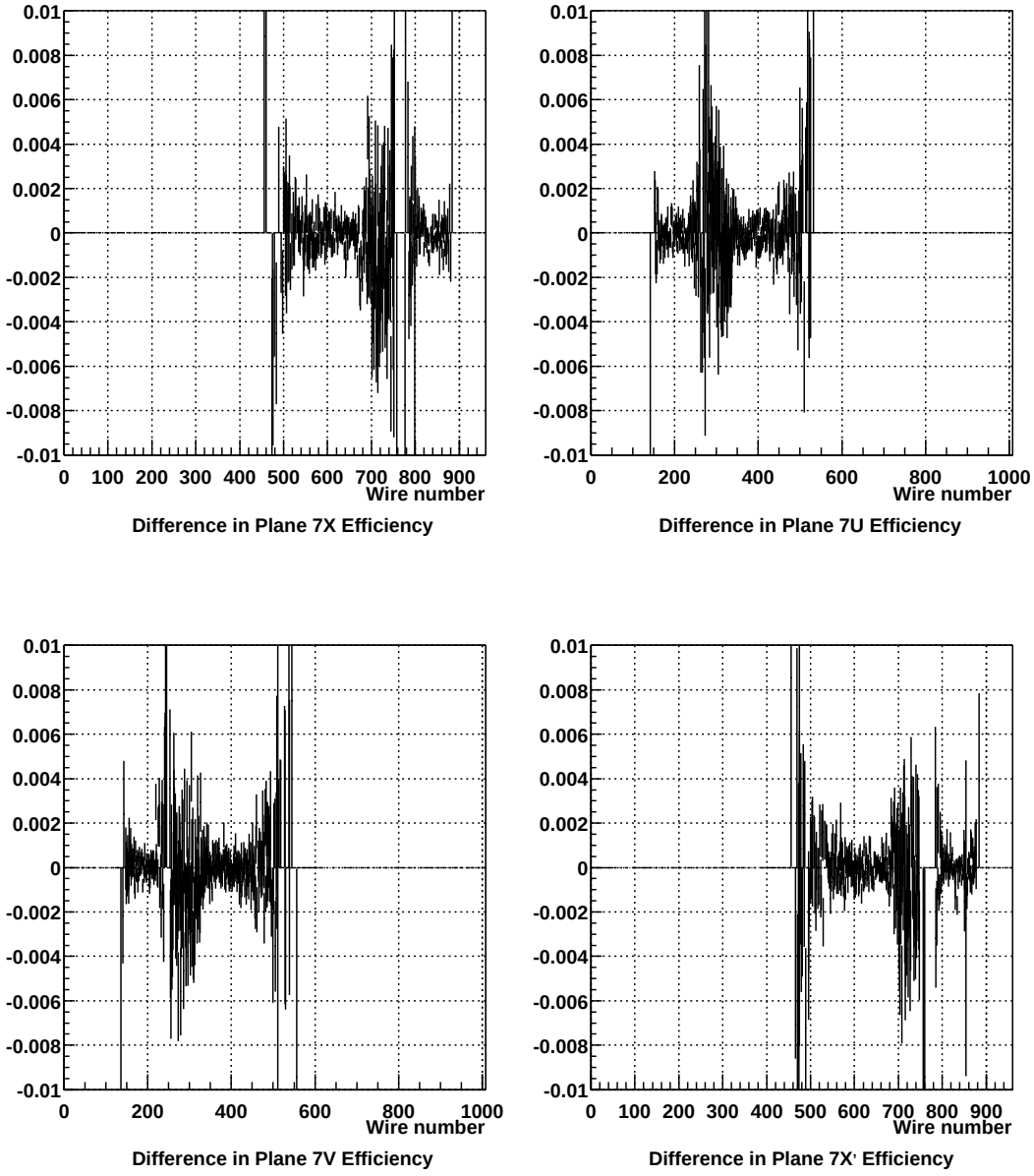


Figure 3.21: Difference in wire efficiency for C7 between positive run 2179 and negative run 2369.

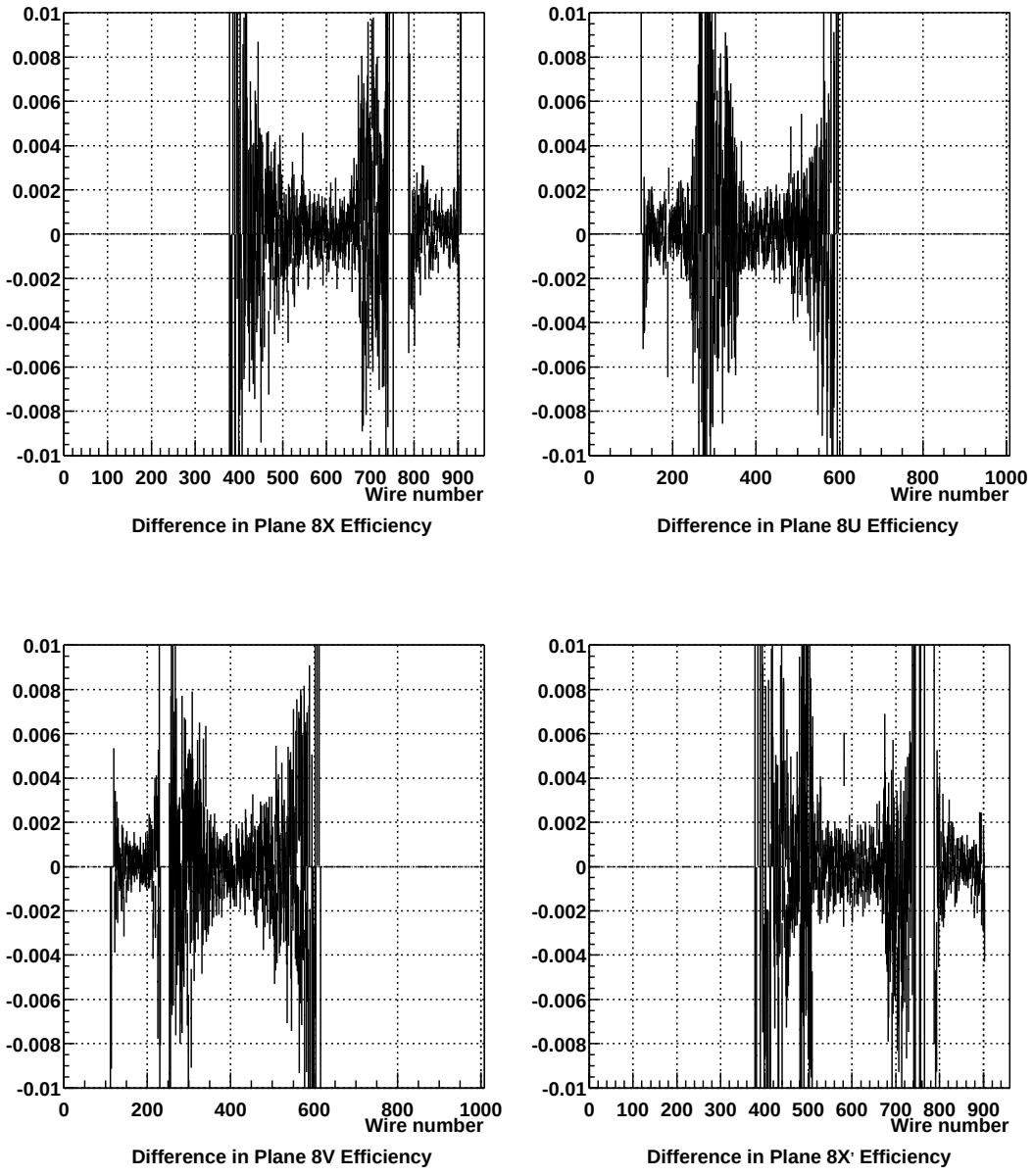


Figure 3.22: Difference in wire efficiency for C8 between positive run 2179 and negative run 2369.

latched information of that counter was checked. The efficiency of a particular OS counter labeled as $i$ was calculated as follows:

$$\epsilon_{OS}(i) = \frac{number\ of\ tracks\ transvering\ counter\ i\ with\ latch\ set}{number\ of\ tracks\ transvering\ counter\ i} \tag{3.5}$$

The efficiencies of the OS counters for a positive run and the difference in the efficiencies between a positive and a negative run that were separated by 44 days are shown in Figure 3.23.

**Efficiencies of SS Counters**

The efficiency of the SS counters was measured using the fact that there are two SS tracks associated with a Kaon candidate. The two SS tracks were projected to the location of the SS hodoscope to determine the corresponding counters that the tracks were expected to transverse, and only tracks with projection at least 1 cm away from all four edges of the counter were accepted. The counter matching one of the SS tracks must have its latch set since the event must satisfy the trigger requirement. Then the other SS track was used to measure the SS counter efficiencies in the same way as it was being done for the OS counters. The efficiencies of the SS counter for a positive run and the difference in efficiencies between a positive and a negative run that were separated in time by 44 days are shown in Figure 3.24.

**Efficiency of CALK Trigger**

The efficiency of the CALK trigger was measured using Kaon candidates that satisfied the LRW trigger. The efficiency was determined as a function of the momentum of the OS track, integrated over the fiducial of the calorimeter. It was also measured as a function of the X-position of the OS track at the upstream face of the calorimeter, intergrated over the momentum of the track. Since the cross-section of the calorimeter did not cover the whole phase space of the odd pion from the charged Kaon decay, the momentum and X-position at which CALK turns on could also be measured.

For a Kaon candidate satisfying the LRW trigger, its OS track was projected to the upstream face of the calorimeter and was required to be within the vertical (Y) extent of the calorimeter. Two distributions were histogramed: one with the momentum of the OS track, the other with the momentum of the OS track with the CALK trigger set. The

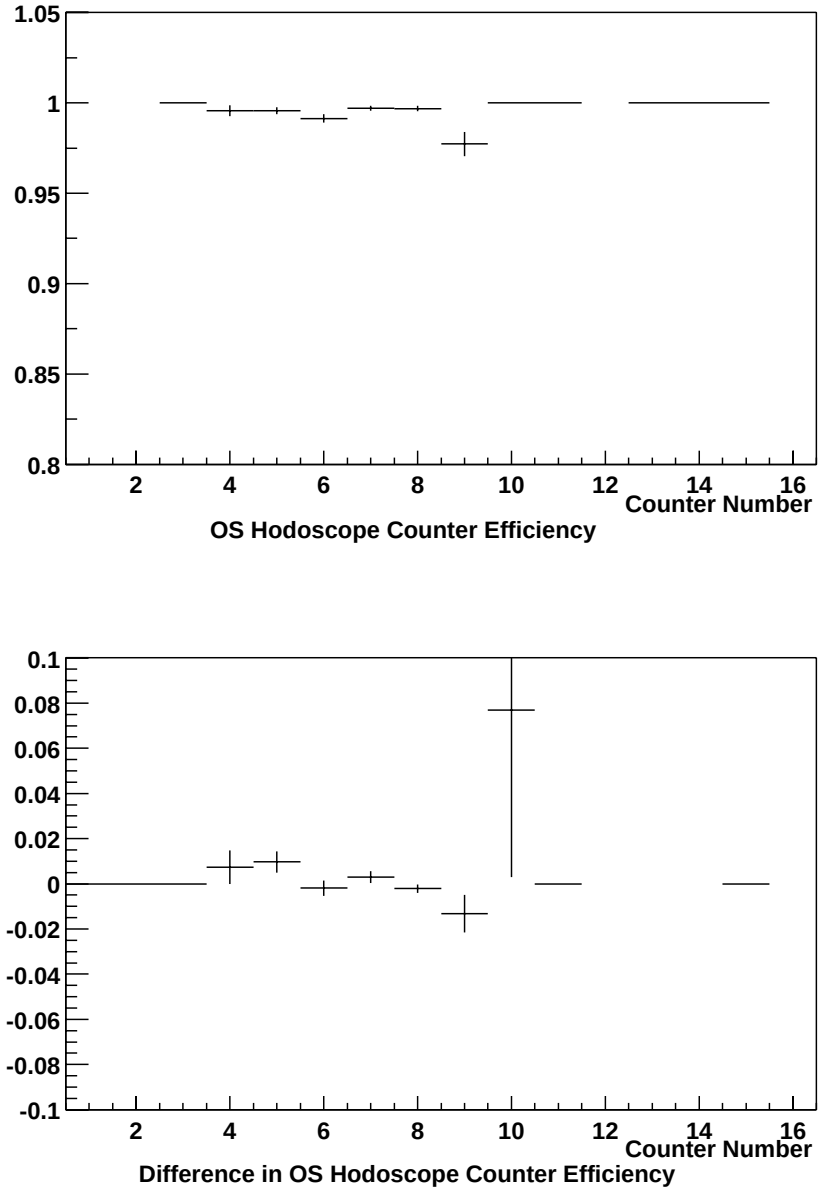


Figure 3.23: Efficiency of OS counters for positive run 2179 is shown in the top plot. Difference in the efficiencies of the OS counters between positive run 2179 and negative run 2369 is shown in the bottom plot. There are points missing the plots because they are outside the scale of the plots due to low statistics.

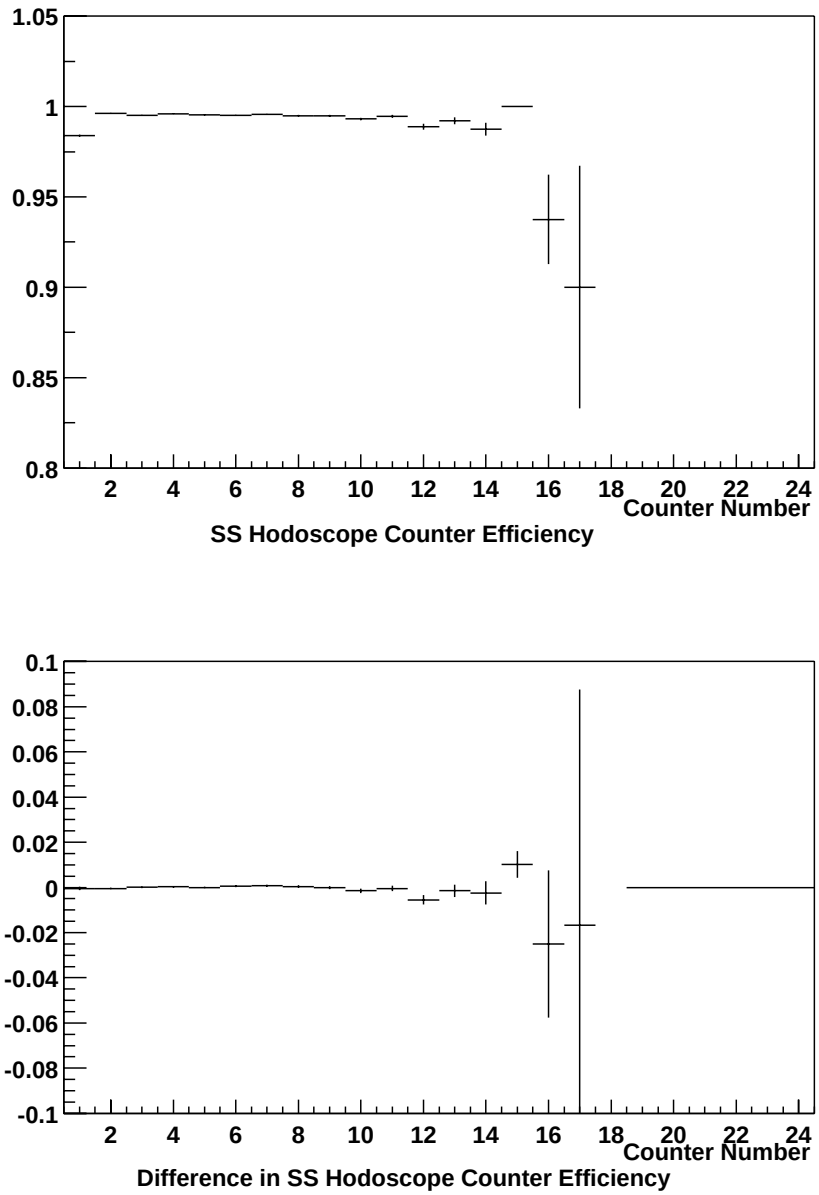


Figure 3.24: Efficiency of SS counters for positive run 2179 is shown in the top plot. Difference in the efficiencies of the SS counters between positive run 2179 and negative run 2369 is shown in the bottom plot.

efficiency as a function of the OS track momentum is the ratio of these two distributions. Similarly, instead of the momentum of the OS track, the X-position of the OS track at the upstream face of the calorimeter were histogramed. The ratio of these distributions gives the efficiency as a function of the X-position of the OS track at the upstream face of the calorimeter. Figure 3.25 shows the efficiency of the CALK trigger as a function of the momentum and the X-position of the OS track for a positive run. The curve is a parametrization of the efficiency with the following function:

$$f_{eff}(x) = 0.5 \times A_0 \times (tanh(A_1 \times (x - A_2)) + 1) \tag{3.6}$$

where $x$ is the momentum or the X-position of the OS track at the upstream face of the caloriemter, $A_0$ is the efficiency of the CALK trigger when it is fully efficient, $A_1$ is a measure of the width of the turn-on region and $A_2$ is the momentum or X-position at which the efficiency is 50%. The difference in the CALK efficiency as a function of the momentum and X-position of the OS track between a positive and a negative run that were separated by 44 days are shown in Figure 3.26.

## 3.4 Final Event Selection

The Kaon candidates resulting from the third pass are not necessarily genuine $\tau$ decays of charged Kaon. A large fraction of the events are background events from hyperons decays, and interactions along the walls of the collimator near the exit and in the spectrometer. In order to remove these background events and optimize the signal-to-background ratio, the following set of cuts was applied:

1. $m_{\Lambda\pi}$ Cut

   The decay chain of $\Xi \to \Lambda + \pi$ followed by $\Lambda \to p + \pi$ produces three charged tracks that can result in an invariant mass under the three-pion hypothesis consistent with the charged Kaon mass. Figure 3.27 show the mass distribution of Kaon candidates under the $\Lambda\pi$ hypothesis. A cut was applied to exclude events with the reconstructed $\Lambda\pi$ mass within 10 MeV/c$^2$ of the mean reconstructed $\Xi$ mass of 1.322 GeV/c$^2$.

2. $m_{\Lambda K}$ Cut

   Similar to the $\Xi$ decay, the decay $\Omega \to \Lambda + K$ followed by $\Lambda \to p + \pi$ is potentially a background to the Kaon candidates. However, based on Monte Carlo simulation, when

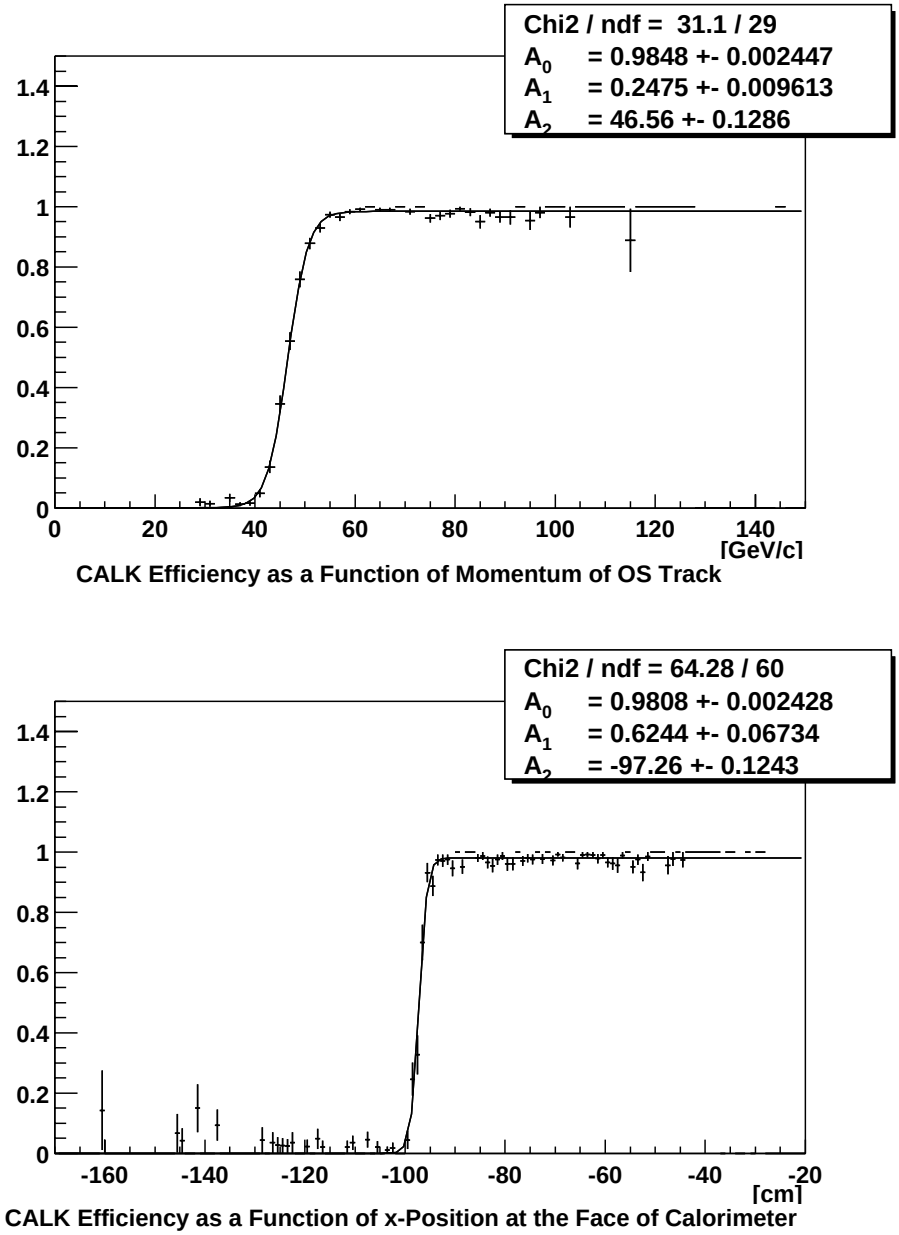


Figure 3.25: Efficiency of CALK trigger as a function of momentum (top) and X-position (bottom) of the OS track at the upstream face of the calorimeter for positive run 2179. The parametrization is also shown.

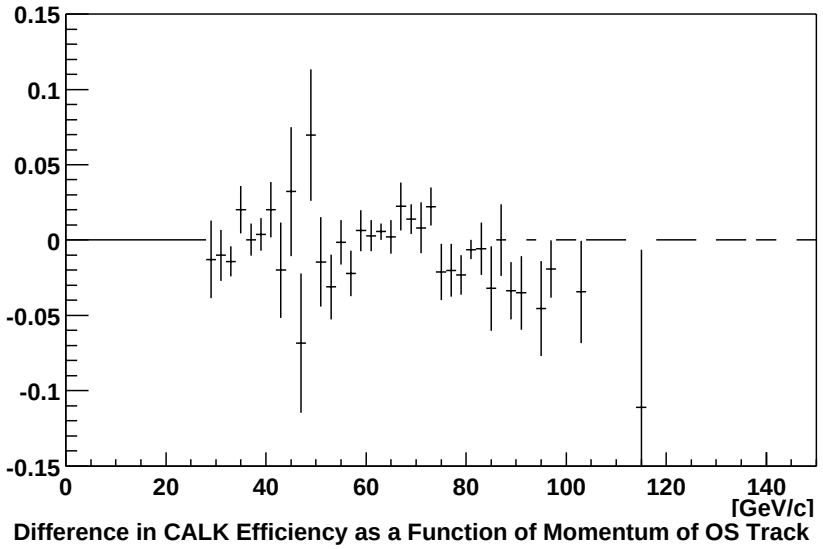


Figure 3.26: Difference in CALK trigger efficiency as a function of momentum (top) and X-position (bottom) of the OS track at the upstream face of the calorimeter between positive run 2179 and negative run 2369.

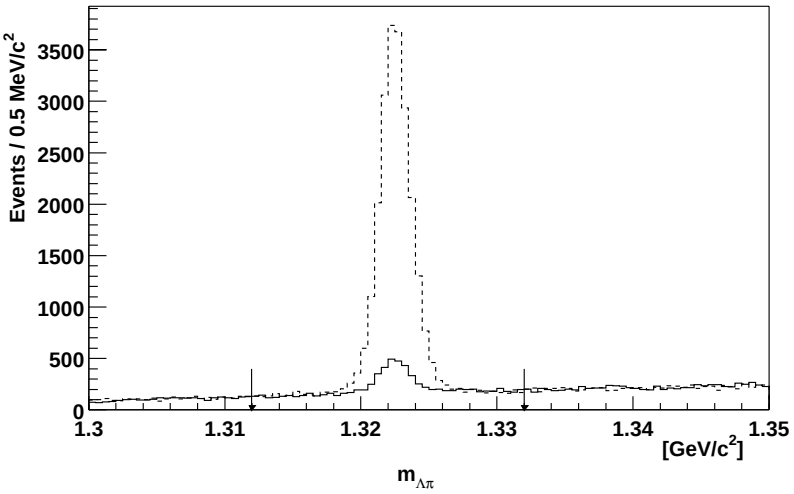


Figure 3.27: Distribution of reconstructed $\Lambda\pi$ invariant mass for Kaon events with all cuts applied except the $m_{\Lambda\pi}$ cut for a positive (line) and a negative (dash) run. The arrows show the location of the cut.

the $\Omega$ events are reconstructed under the $3\pi$ hypothesis, only the tail of the three-pion invariant mass distribution falls inside the charged Kaon mass region. Thus, the $\Omega$ background is significantly smaller than that of the $\Xi$ background. Furthermore, the yield of $\Omega$ is much smaller than $\Xi$. Figure 3.28 shows the mass distribution of Kaon candidates under the $\Lambda K$ hypothesis. A cut was applied to exclude events with the reconstructed $\Lambda K$ mass within 7 MeV/c$^2$ of the mean reconstructed $\Omega$ mass of 1.672 GeV/c$^2$.

3. $\chi^2_{DF}$ Cut

   Figure 3.29 is a distribution of the reduced GFIT1V $\chi^2$ of good Kaon candidates. The number of degrees of freedom was typically 84 corresponding to three charged tracks with 32 measurements for each track and 12 fitting parameters. It was required that the reduced GFIT1V $\chi^2$ be less than 2.2.

4. Kaon Momentum Cut

   The acceptance of the collimator as a function of the momentum of the secondary beam is shown in Figure 2.4. The accepted momentum range of the Kaon candidates was slightly higher than the designed value with the target centered on the aperture

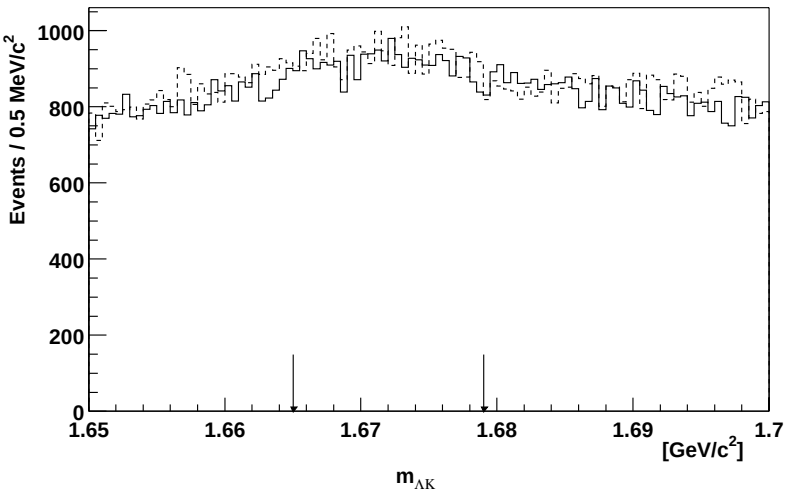


Figure 3.28: Distribution of reconstructed $\Lambda K$ invariant mass for Kaon events with all cuts applied except the $m_{\Lambda K}$ cut for a positive (line) and a negative (dash) run. The arrows show the location of the cut.

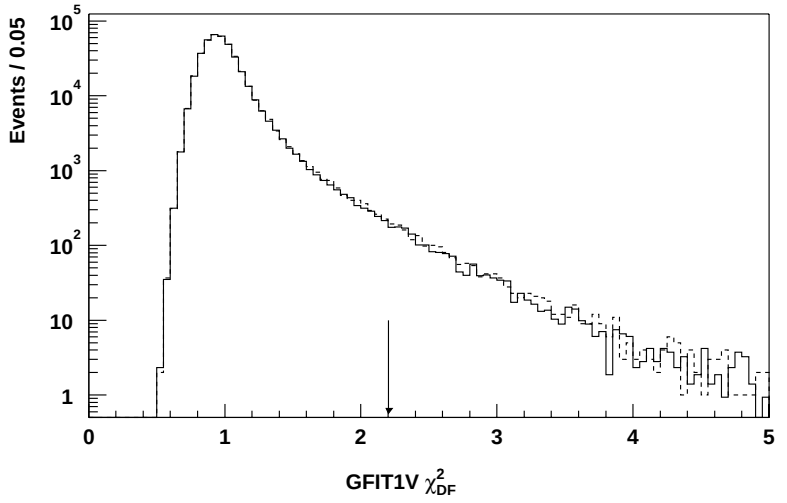


Figure 3.29: Distribution of reduced GFIT1V $\chi^2$ for Kaon candidate events with all cuts applied except the $\chi^2_{DF}$ cut for a positive (line) and a negative (dash) run. The arrow shows the location of the cut.

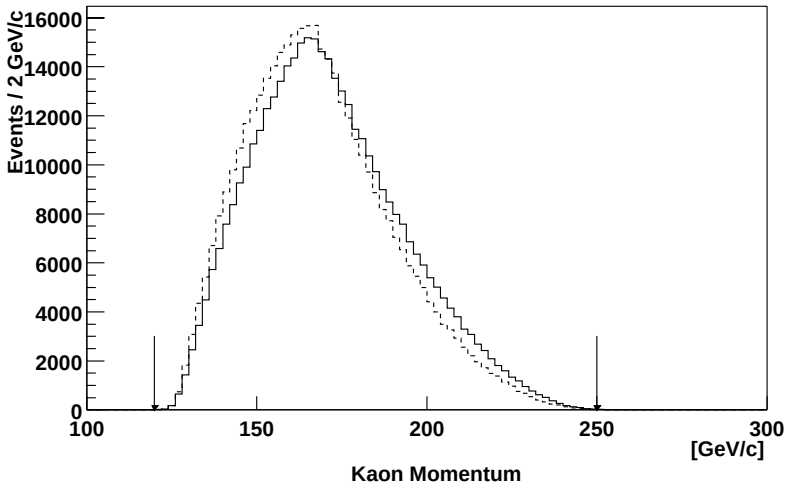


Figure 3.30: Distribution of reconstructed momentum of Kaon candidates with all cuts applied except the Kaon momentum cut for a positive (line) and a negative (dash) run. The arrows show the location of the cut.

at the entrance of the collimator. However the observed momentum distribution could be reproduced in the Monte Carlo simulation with the target lowered by 1.3 mm from the center of the aperture. It was required that the reconstructed momentum of the Kaon candidates be in the range between 120 GeV/c and 250 GeV/c as indicated in Figure 3.30.

5. Collimator Exit Cut

   The aperture at the exit of the collimator was 2 cm in the horizontal direction and 1 cm in the vertical direction. Figures 3.31 and 3.32 show the X ($x_{collimator}$) and Y ($y_{collimator}$) projections of the reconstructed Kaon track at the exit of the collimator. The width of the distribution of the x projection is significantly less than the expected physical aperture because the target was not completely centered on the aperture of the collimator at the entrance but was located at $x \approx +5$ mm. It was required that the $x_{collimator}$ and $y_{collimator}$ of the events must satisfy the conditions $-0.90$ cm $< x_{collimator} < 0.90$ cm and $-0.60$ cm $< y_{collimator} < 0.65$ cm.

6. Target-pointing Cut

   Figures 3.33 and 3.34 show the X ($x_{target}$) and Y ($y_{target}$) positions of the recon-

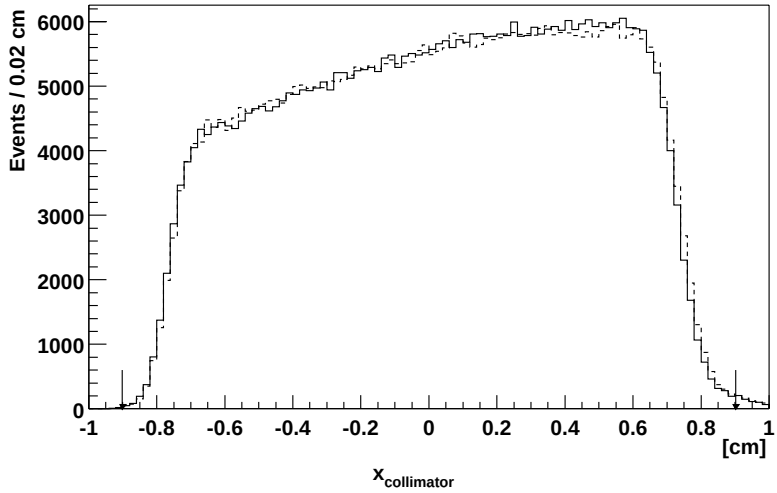


Figure 3.31: Distribution of X projection of reconstucted Kaon track at the exit of the collimator with all cuts applied except the cut at the collimator exit for a positive (line) and a negative (dash) run. The arrows show the location of the cut.

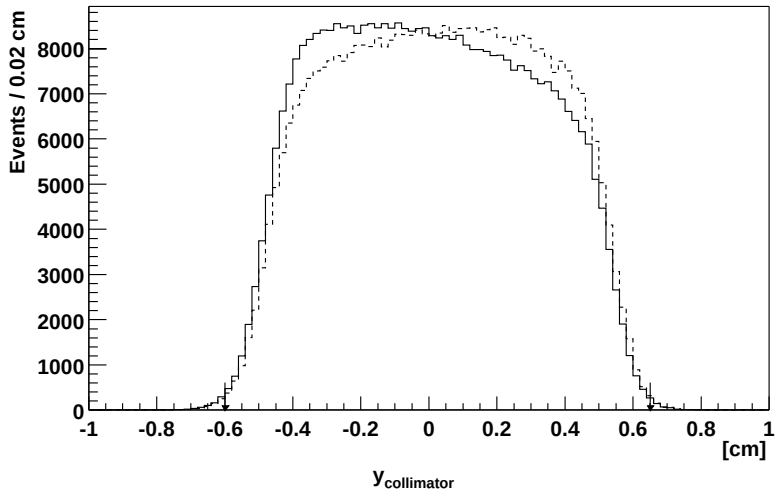


Figure 3.32: Distribution of Y projection of reconstucted Kaon track at the exit of the collimator with all cuts applied except the cut at the collimator exit for a positive (line) and a negative (dash) run. The arrows show the location of the cut.

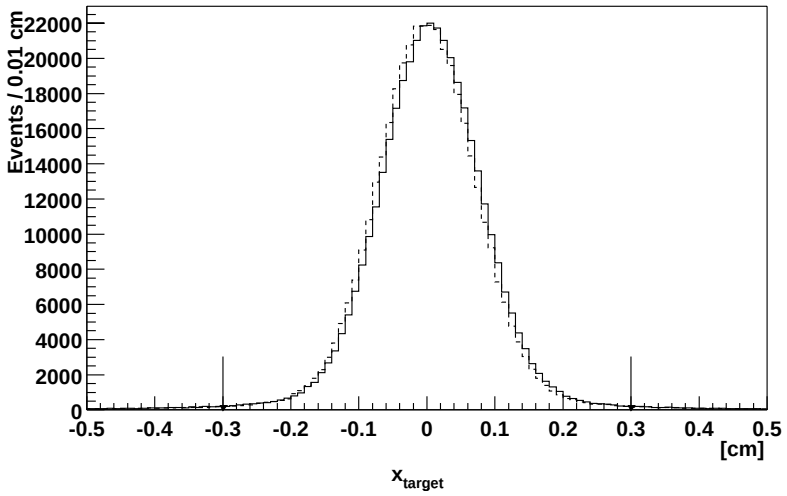


Figure 3.33: Distribution of X position for Kaon events at the target with all cuts applied except the target-pointing cut for a positive (line) and a negative (dash) run. The arrows show the location of the cut.

structed Kaon track after tracing back to the Z location of the center of the target (see Appendix C). It was found that the incident proton beam at the target could vary as much as 0.5 mm from run to run in the X and Y direction . In order to account for this variation, a modest cut on $x_{target}$ and $y_{target}$ was applied: $-0.30$ cm $< x_{target} < 0.30$ cm and $-0.20$ cm $< y_{target} < 0.96$ cm.

7. Decay Vertex Z Cut

   The distribution of the Z position of the decay vertex ($z_{decay}$) for Kaon candidates with all cuts applied except the decay vertex Z cut is shown in Figure 3.35. A majority of the events from interactions of the secondary beam particles with the material in the spectrometer has been removed with the target-pointing cut. The peaks at the Z positions where wire chambers C1 and C2 were located are Kaon decays after transversing the wire chambers. These events produced a single hit at C1 and C2 by the parent track. Since the tracking algorithm allowed multiple tracks to share a hit, the reconstructed decay vertex was pulled towards the location of the wire chamber, hence creating the peaks. The Z position of the decay vertex was required to be between 100 cm and 1250 cm to reject events due to interactions at the windows of

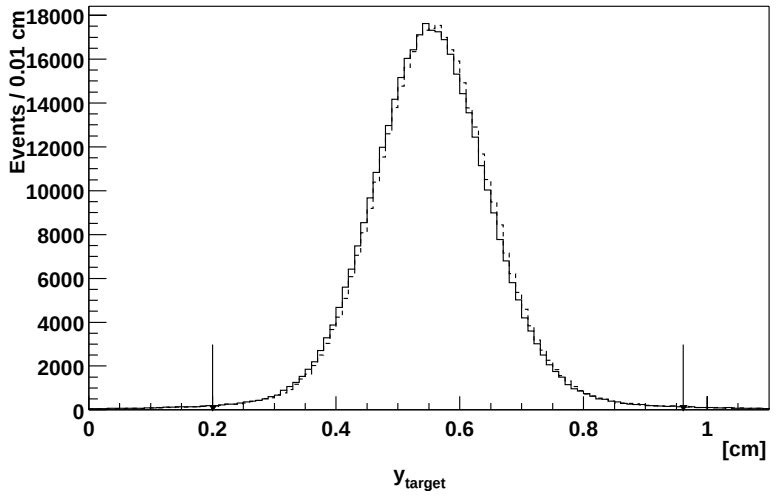


Figure 3.34: Distribution of the Y position for Kaon events at the exit of the collimator with all cuts applied except the target-pointing cut for a positive (line) and a negative (dash) run. The arrows show the location of the cut.

the decay pipe.

8. Photon Conversion Cut

   There were numerous photons from interactions and decays transversing the spectrometer. Such a photon could convert to an electron-positron pair which when combined with another charged track could produce a three-pion invariant mass consistent with the charged Kaon mass. Figure 3.36 shows the distribution of the smaller dielectron invariant mass ($m_{ee}$) among the combinations of two SS tracks and an OS track under the hypothesis of dielectron. A cut was applied on the dielectron invariant mass, requiring $m_{ee} > 0.006 GeV/c^2$.

9. Calorimeter Fiducial Cut

   It is found that the calorimeter was efficient up to around x = -95 cm. Allowing for statistical fluctuation, it was required that the X projection ($x_{calorimeter}$) of the OS track at the upstream face of the calorimeter be greater than -90 cm.

10. MWPC Fiducial Cut

    Tracks were projected to each MWPC location and were required to be within the

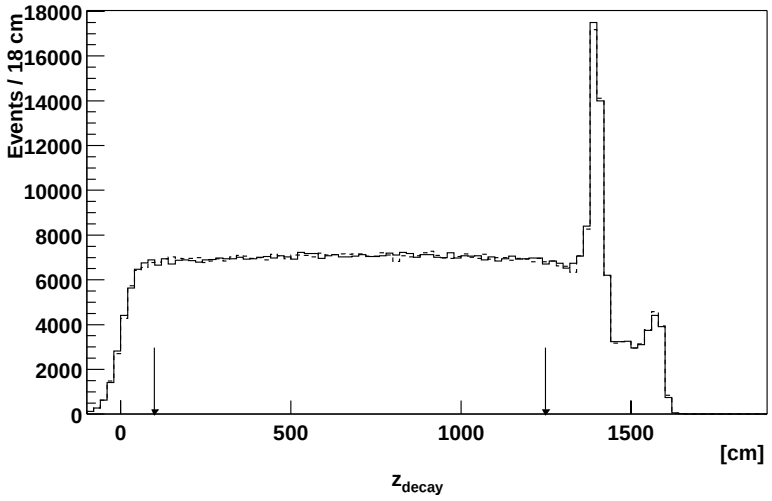


Figure 3.35: Distribution of Z position of decay vertex for Kaon candidate events with all cuts applied except the decay vertex Z cut for a positive (line) and a negative (dash) run. The arrows show the location of the cut.

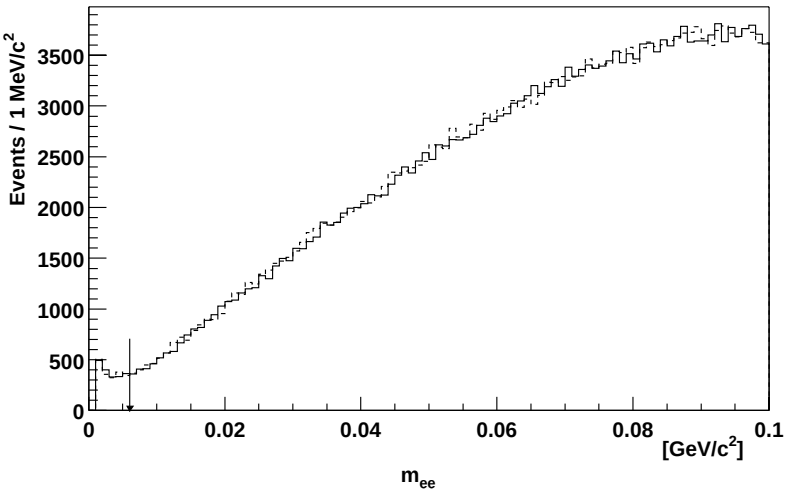


Figure 3.36: Distribution of smaller dielectron invariant mass among the combinations of two SS tracks and an OS track under the hypothesis of dielectron for Kaon events with all cuts applied except the photon conversion cut for a positive (line) and a negative (dash) run. The arrow shows the location of the cut.

MWPC active region.

11. Analysis Magnet Aperture Cut

    Tracks were projected to the downstream end of the two analysis magnets and were required to fall within a fiducial aperture defined by a rectangle with its edges 1 cm inside the actual aperture. This cut was applied to remove events with tracks near the edge of the magnet.

12. Single-Kaon Cut

    Figure 3.4 shows the probability distribution of the number of Kaon candidates in a single event. Only about 6% of the Kaon candidate events have more than one candidate. Since the sensitivity of the asymmetry measurement was not significantly lowered, events with more than one Kaon candidate were removed in order to avoid any ambiguity in selecting the Kaon candidate selection.

13. K Trigger Cut

    Only events that satisfied the K trigger set were accepted. The efficiency of the K trigger was about 99.6%.

Figure 3.37 shows the three-pion invariant mass of Kaon candidates after all the above cuts are applied. Only candidates with the reconstructed $3\pi$ invariant mass between 0.486 GeV/$c^2$ and 0.502 GeV/$c^2$ were accepted. The signal-to-background ratio in this region is estimated to be 400. In addition, the Dalitz plot of $\tau$ decay of charged Kaon for a positive run is shown in Figure 3.38.

The final selection criteria described above are summarized in Table 3.3. These cuts were applied to the Kaon candidate events to select the final event sample for systematic studies and physics measurements to be presented in Chapter 4. The total number of events passing all cuts is about 41.8 million positive Kaons and 12.4 million negative Kaons.

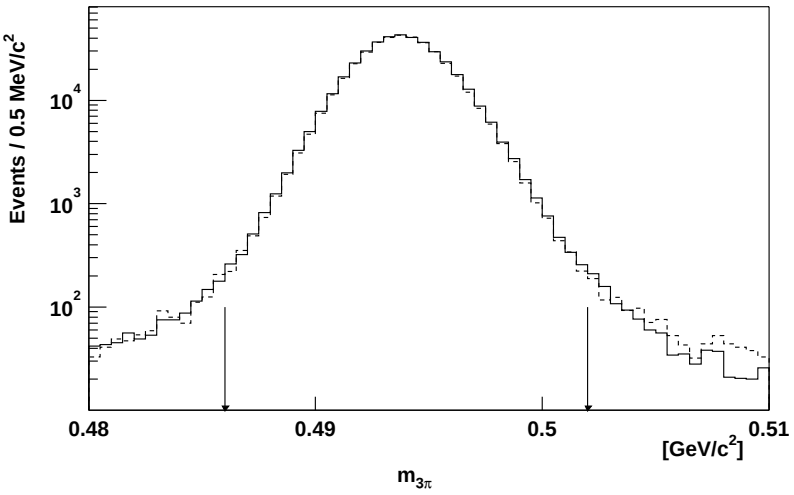


Figure 3.37: Distribution of $3\pi$ invariant mass for Kaon events with all cuts applied except the $m_{3\pi}$ cut for a positive (line) and a negative (dash) run. The arrow shows the location of the cut.

| Cut Characteristic | Requirement |
|---|---|
| $m_{\Lambda\pi}$ | exclude $1.312 < m_{\Lambda\pi} < 1.332$ GeV/c$^2$ |
| $m_{\Lambda K}$ | exclude $1.665 < m_{\Lambda K} < 1.679$ GeV/c$^2$ |
| GFIT1V $\chi^2_{DF}$ | $0 < \chi^2_{DF} < 2.2$ |
| Kaon Momentum | $120 < p_K < 250$ GeV/c |
| Collimator Exit | $-0.90$ cm $< x_{collimator} < 0.90$ cm<br>$-0.60$ cm $< y_{collimator} < 0.65$ cm. |
| Target-pointing | $-0.30$ cm $< x_{target} < 0.30$ cm<br>$-0.20$ cm $< y_{target} < 0.96$ cm |
| Decay Vertex Z | 100 cm $< z_{decay} < 1250$ cm |
| Photon Conversion | $m_{ee} > 0.006$ GeV/c$^2$ |
| Calorimeter Fiducial | $x_{calorimeter} > -90$ cm |
| MWPC Fiducial | Tracks inside the active region |
| Analysis Magnet Fiducial | Tracks more than 1 cm away from edges of magnet |
| Single-Kaon | Events with more than one candidate are removed |
| K Trigger | Only events with K trigger are accepted |
| $m_{3\pi}$ | $0.486 < m_{3\pi} < 0.502$ GeV/c$^2$ |

Table 3.3: List of cuts for selecting the final Kaon candidate.

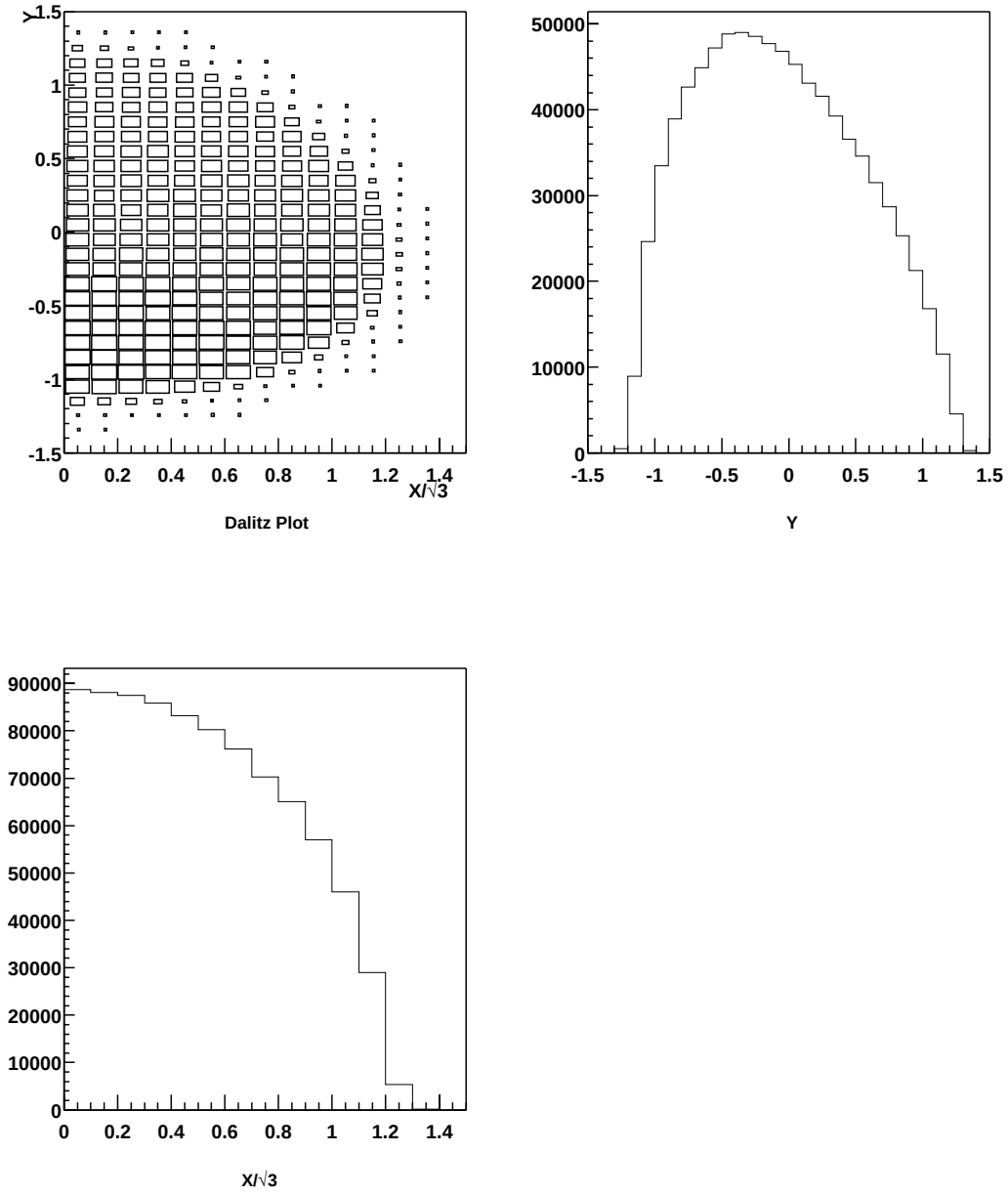


Figure 3.38: Dalitz plot of $K^+ \to \pi^+\pi^+\pi^-$ decay (top left) for a positive run with all cuts applied. The size of each box in the plot is proportional to its contents. The $X/\sqrt{3}$ and $Y$ projections are also shown.

# Chapter 4

# Analysis

The CP asymmetry analysis entails comparing the linear slopes $g$ of the Dalitz distributions between $\tau^+$ and $\tau^-$ decays of charged Kaons. The total number of events passing all cuts is about 41.8 million positive Kaons and 12.4 million negative Kaons. The statistical error of the asymmetry $\delta g$ is about $1.5 \times 10^{-3}$. The goal of this analysis is to demonstrate that the total systematic error from all possible sources is comparable to or below the statistical sensitivity of the measurement. It is important to note that any systematic effect common to both positive and negative data will cancel in the asymmetry measurement. Thus, the strategy of this analysis is to show that any difference between the positive and negative data which can result in a fake asymmetry is comparable to or below the sensitivity of the measurement.

## 4.1 Temporal Variations

In Section 3.3.3, we have studied the differences in the efficiencies of the MWPCs, hodoscopes, and calorimeter trigger between a positive and a negative run that were taken 44 days aparts. The differences in the efficiencies between the two runs were small. As will be discussed in Section 4.5, the mean of the differences in the efficiencies of the detectors were calculated. The results were then used in the Monte Carlo simulation for systematic studies.

To gain a better understanding of any potential difference between the positive and negative data, a number of parameters characterizing the stability of the incident proton beam and the performance of the spectrometer were examined on a run-by-run basis.

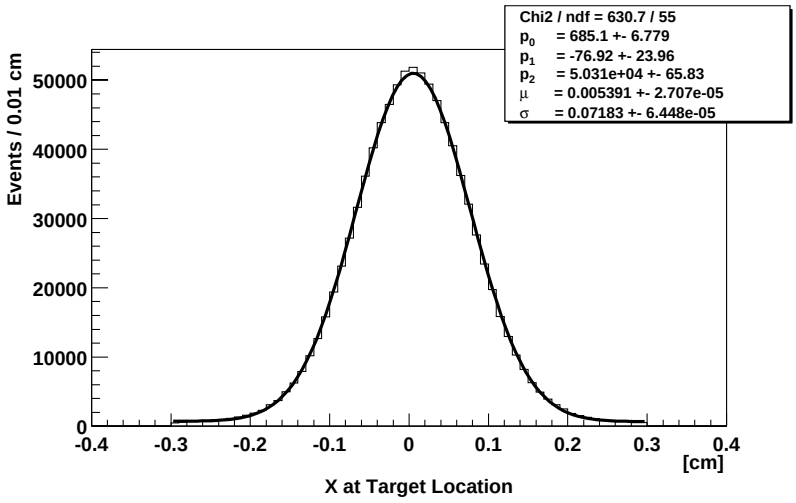


Figure 4.1: Distribution of X position of Kaon candidates at the target location for postive run 2179. The distribution is fitted with a Gaussian plus a linear function. Parameters $p_0$ and $p_1$ are the coefficients of the linear function, $p_2$, $\mu$ and $\sigma$ are the scale factor, mean and standard deviation of the Gaussian respectively.

### 4.1.1 Targeting

The reconstructed Kaon candidates were traced back to the Z-position of the target (defined to be the center of the target) through the hyperon magnet using the algorithm described in Appendix C. As a result, the distribution of the Kaon candidates at the target was determined. Variations in the targeting led to variations in the beam momentum and in the position of the Kaons at the exit of the collimator. These variations could in turn affect the acceptance, hence creating an asymmetry between the positive and negative data.

The distributions of the transverse positions of the Kaon candidates at the target position are shown in Figures 4.1 and 4.2 for a positive run. Each distribution is fitted with a Gaussian plus a linear function to determine the mean and width of the distribution for a given run. Figures 4.3 and 4.4 show the mean of the X and Y positions as a function of run number respectively. A better way to look at the variation is the distribution of the mean which are shown in the same figures. The range of the variations of the mean is about 0.5 mm in both X and Y positions. In addition, the mean of the Y position tends to increase slightly with time. However, the method used in the analysis, to be described in Section 4.2, will automatically correct for any variations in the momentum and positions of

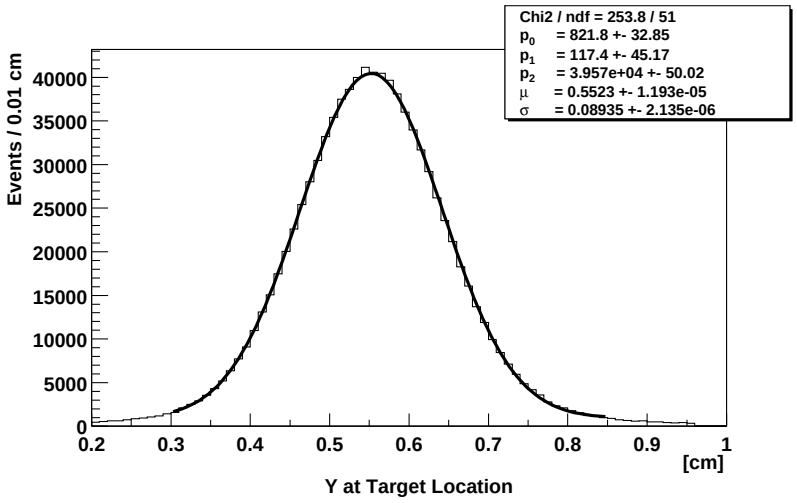


Figure 4.2: Distribution of Y position of Kaon candidates at the target location for postive run 2179. The distribution is fitted with a Gaussian plus a linear function. Parameters $p_0$ and $p_1$ are the coefficients of the linear background, $p_2$, $\mu$ and $\sigma$ are the scale factor, mean and standard deviation of the Gaussian respectively.

the Kaons.

### 4.1.2 Reconstructed Kaon Mass

Figure 4.5 shows the distribution of the $3\pi$ invariant mass for a positive run. It can be described by an expression consisted of two Gaussian distributions and a linear function:

$$f(x) = p_0 + p_1 x + p_2 e^{-(x-m_1)^2/2\sigma_1^2} + p_3 e^{-(x-m_2)^2/2\sigma_2^2} \tag{4.1}$$

where $p_0$ and $p_1$ are the coefficients of the linear function, $p_2$ and $p_3$ are the scale factors of the two Gaussians, $m_1$ and $m_2$ are the means of the Gaussians, and $\sigma_1$ and $\sigma_2$ are the standard deviations of the Gaussians. The reconstructed Kaon mass is taken as the average of the two Gaussian means.

Figure 4.6 shows the reconstructed Kaon mass as a function of run number for both positive and negative runs. The range of the variation in the reconstructed Kaon mass is about 0.2 MeV/$c^2$. The is remarkably small considering that only a single bend-plane approximation is used to calculate the momentum. In addition, the mean was obtained from a fit that did not represent the distribution particularly well. Depending on the

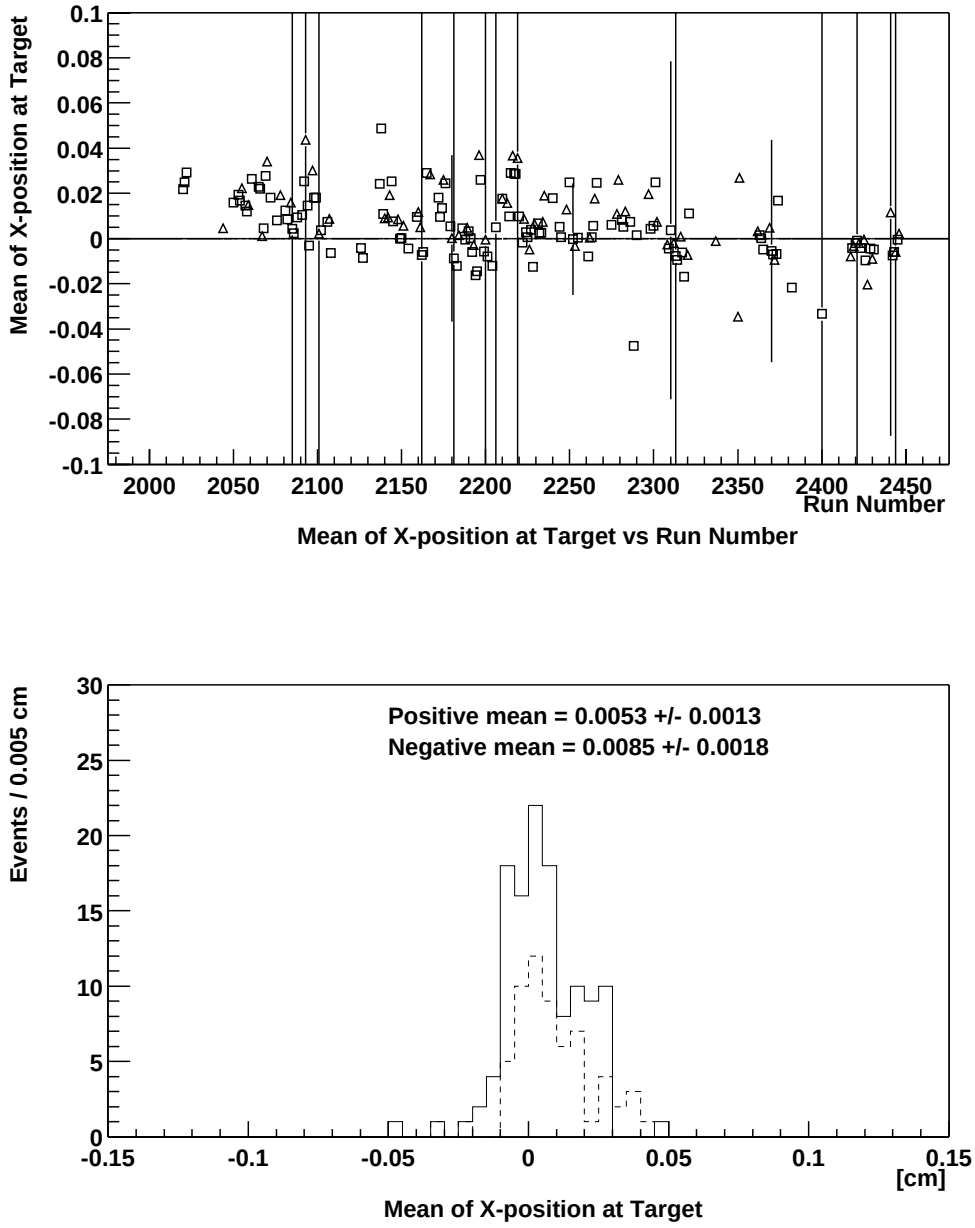


Figure 4.3: Mean X-position of Kaon at the target. The top plot shows the mean X-position versus the run number for positive (open square) and negative (open triangle) runs. The bottom plot shows the distributions of the mean X-position for positive (line) and negative (dash) runs. The mean numbers in the bottom plot are the averages of the measurements assuming no errors.

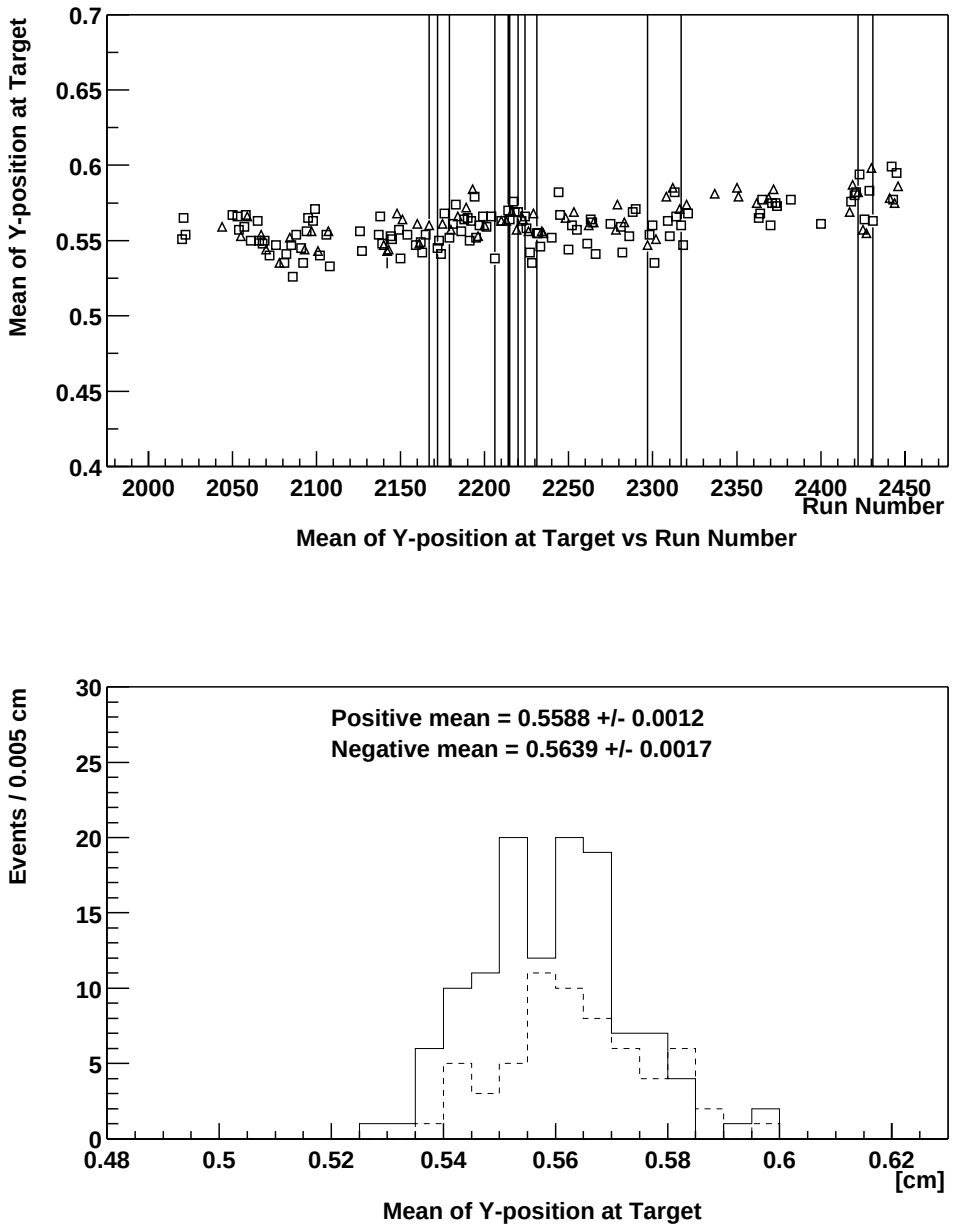


Figure 4.4: Mean Y-position of Kaon at the target. The top plot shows the mean Y-position versus the run number for positive (open square) and negative (open triangle) runs. The bottom plot shows the distributions of the mean Y-position for positive (line) and negative (dash) runs. The mean numbers in the bottom plot are the averages of the measurements assuming no errors.

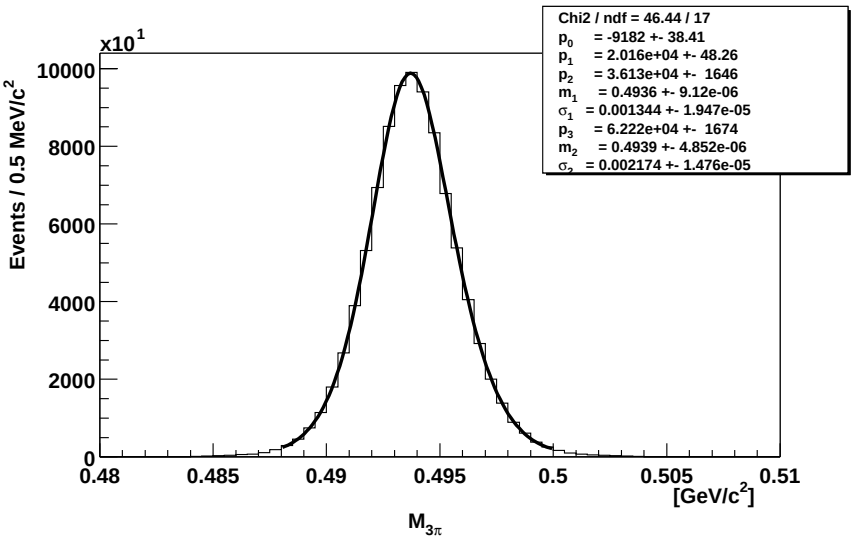


Figure 4.5: Distribution of $3\pi$ invariant mass for postive run 2179. The distribution is fitted to two Gaussians plus a linear function.

starting values of the parameters, the mean could move as much as 0.1 MeV/$c^2$. So, this variation could be artificially introduced by the fit. However, in the early run numbers, the reconstructed Kaon masses were systematically higher which might be attributed to the settlement of the spectrometer.

Even though correction to the overall scale of the magnetic field has been applied using the Hall probes readings of the BM109s, there was still some residual variation which could lead to variation in the reconstructed Kaon mass. However, as shown in Figure 4.6, the reconstructed Kaon masses are normally distributed and the means of the recontructed Kaon mass for the positive and negative runs agree very well implying that any differences in the positive and negative runs causing the variation in the reconstructed Kaon mass would be diluted in the asymmetry measurement.

### 4.1.3 Efficiencies of OS and SS Counters

Figures 4.7 and 4.8 show the efficiency of each OS counter as a function of run number for the positive and negative runs. The distributions of the OS counter efficiency are shown in Figures 4.9 and 4.10. Similar plots for the SS counter efficiency are shown in Figures 4.11, 4.12, 4.13, 4.14, 4.15, and 4.16. As discussed in Section 3.3.3, the efficiency of a counter was

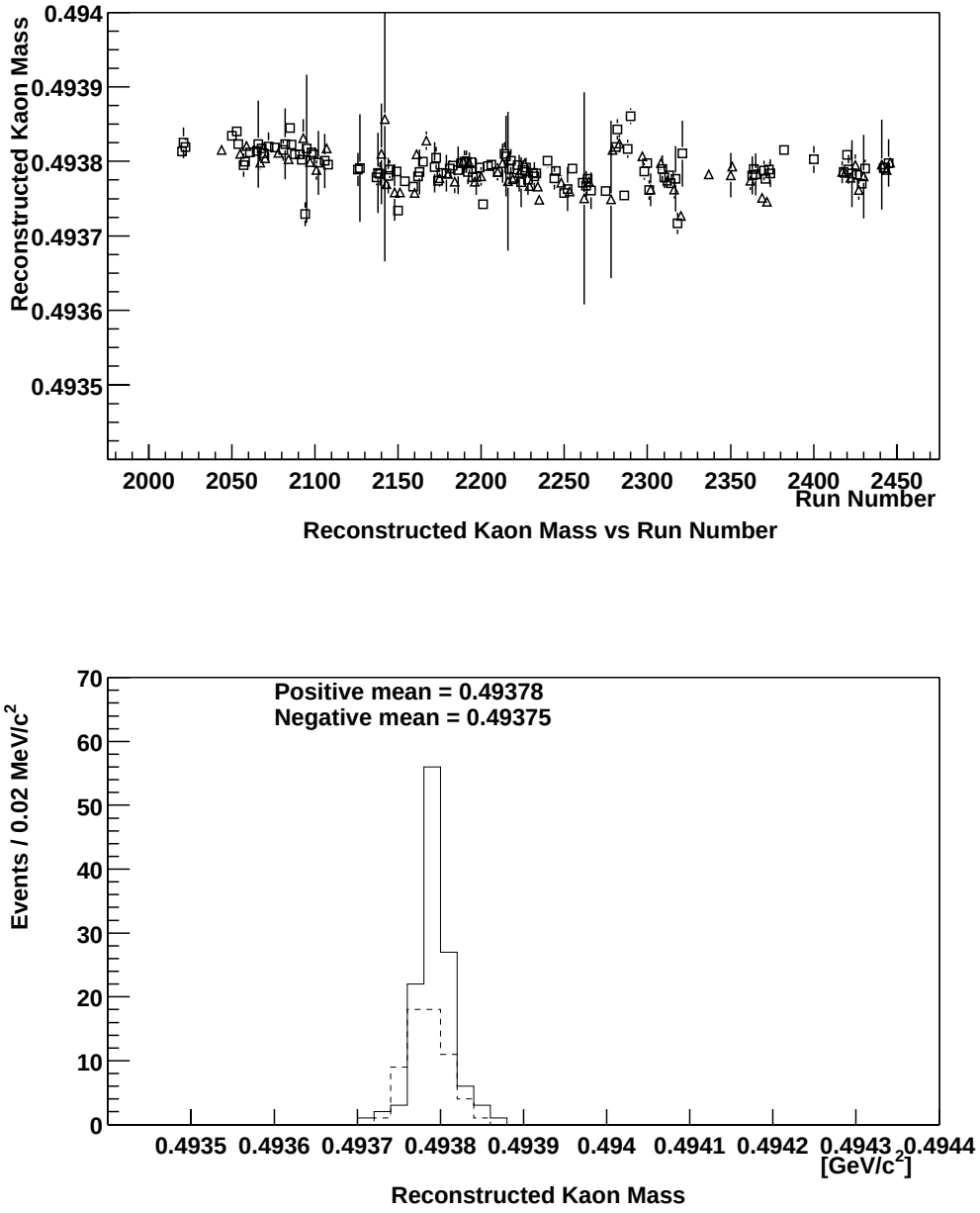


Figure 4.6: Reconstructed Kaon mass. The top plot shows the reconstructed Kaon mass versus the run number for positive (open square) and negative (open triangle) runs. The bottom plot shows the distributions of the reconstructed Kaon mass for positive (line) and negative (dash) runs. The mean numbers in the bottom plot are the weighted averages.

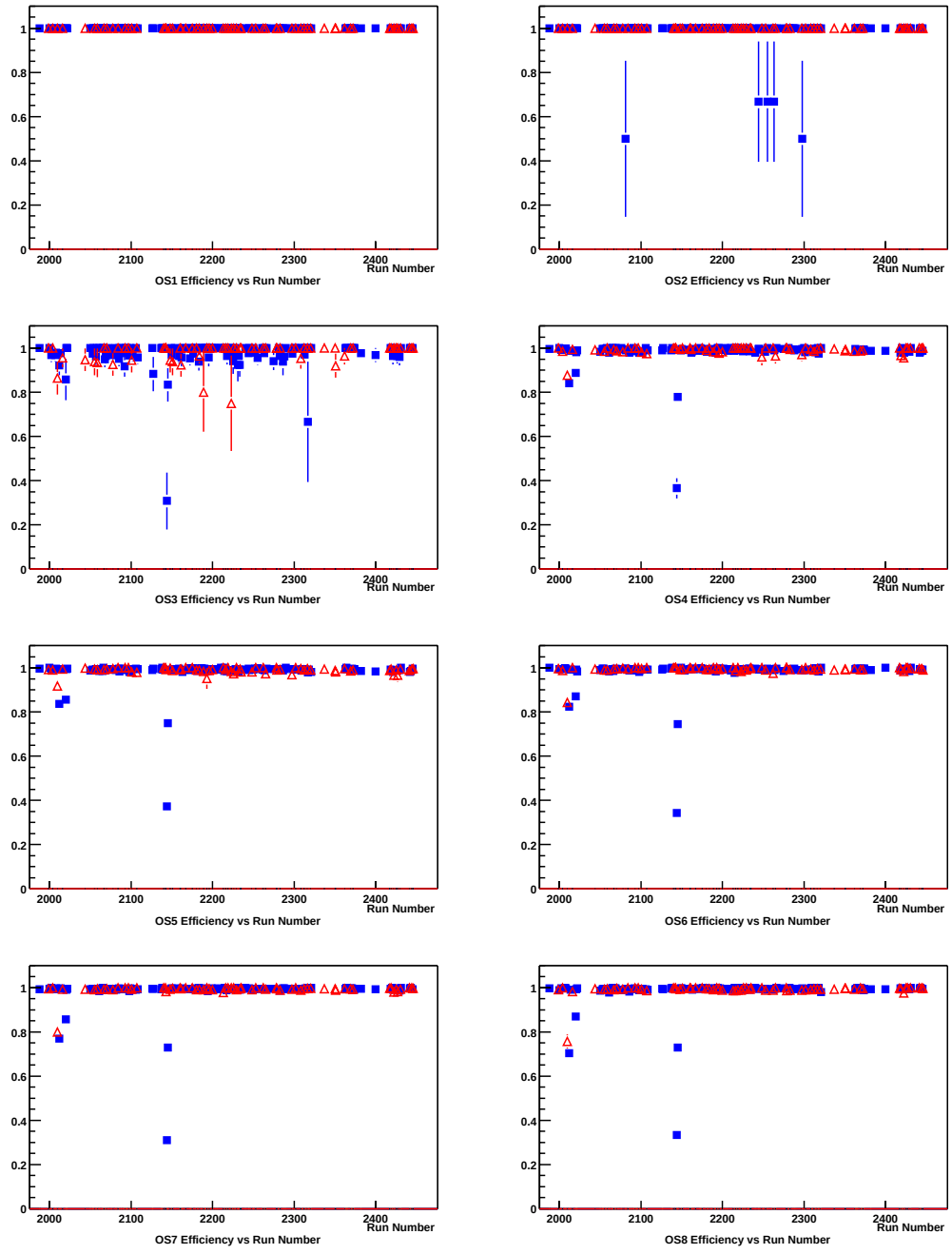


Figure 4.7: Efficiency of OS1 to OS8 versus run number for positive runs (square) and negative runs (open triangle).

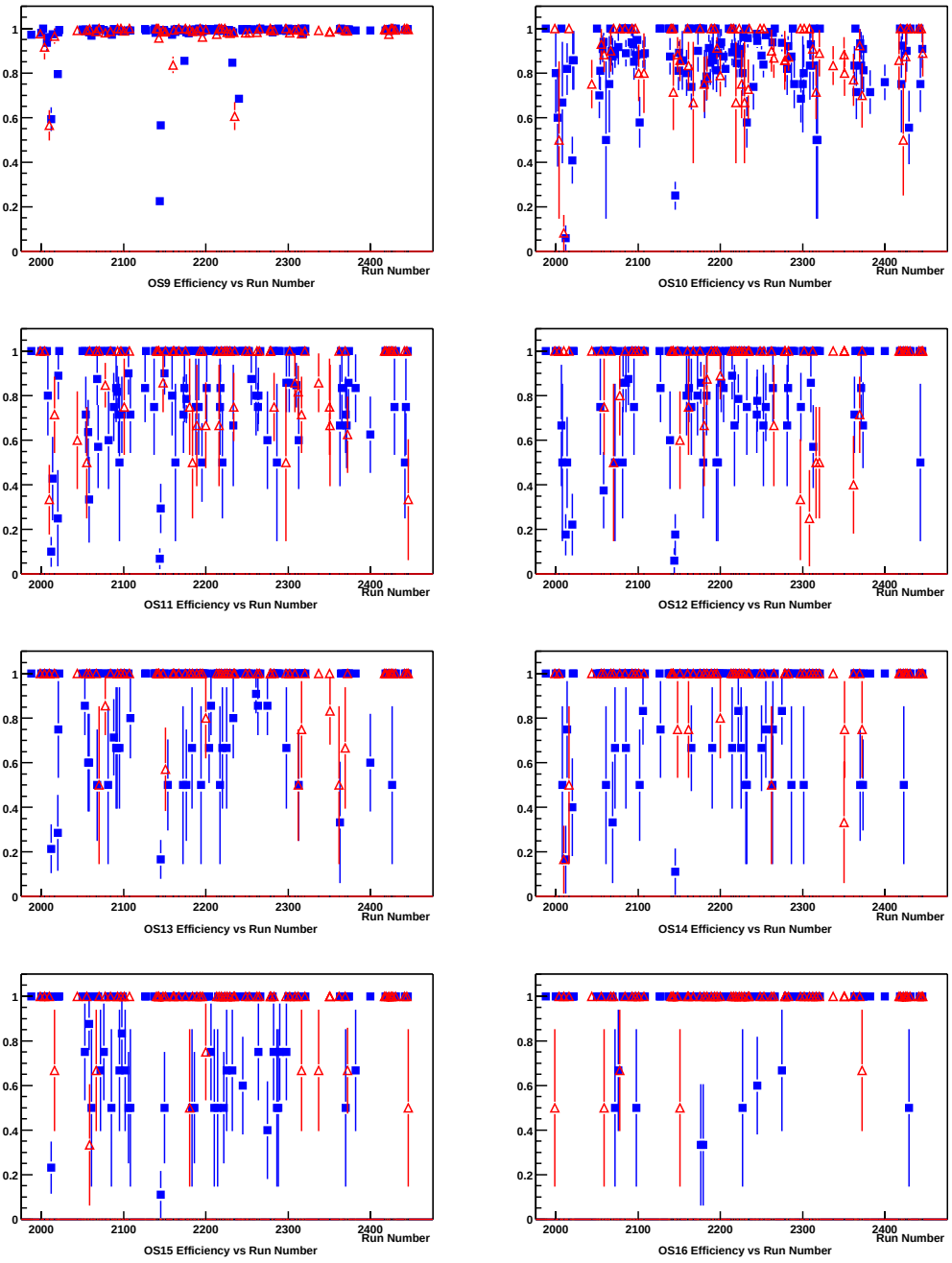


Figure 4.8: Efficiency of OS9 to OS16 versus run number for positive runs (square) and negative runs (open triangle).

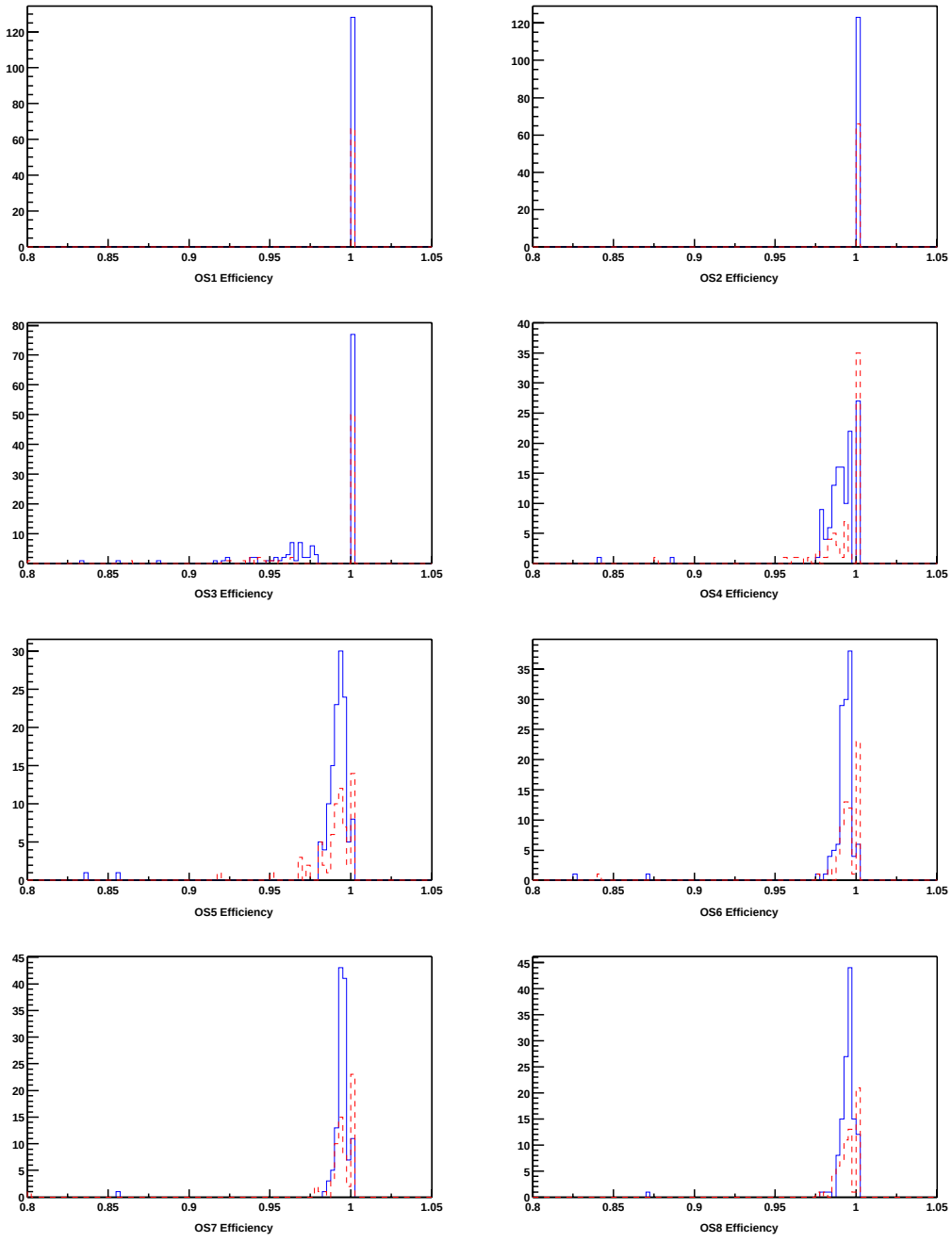


Figure 4.9: Distributions of OS1 to OS8 efficiency for positive runs (line) and negative runs (dash).

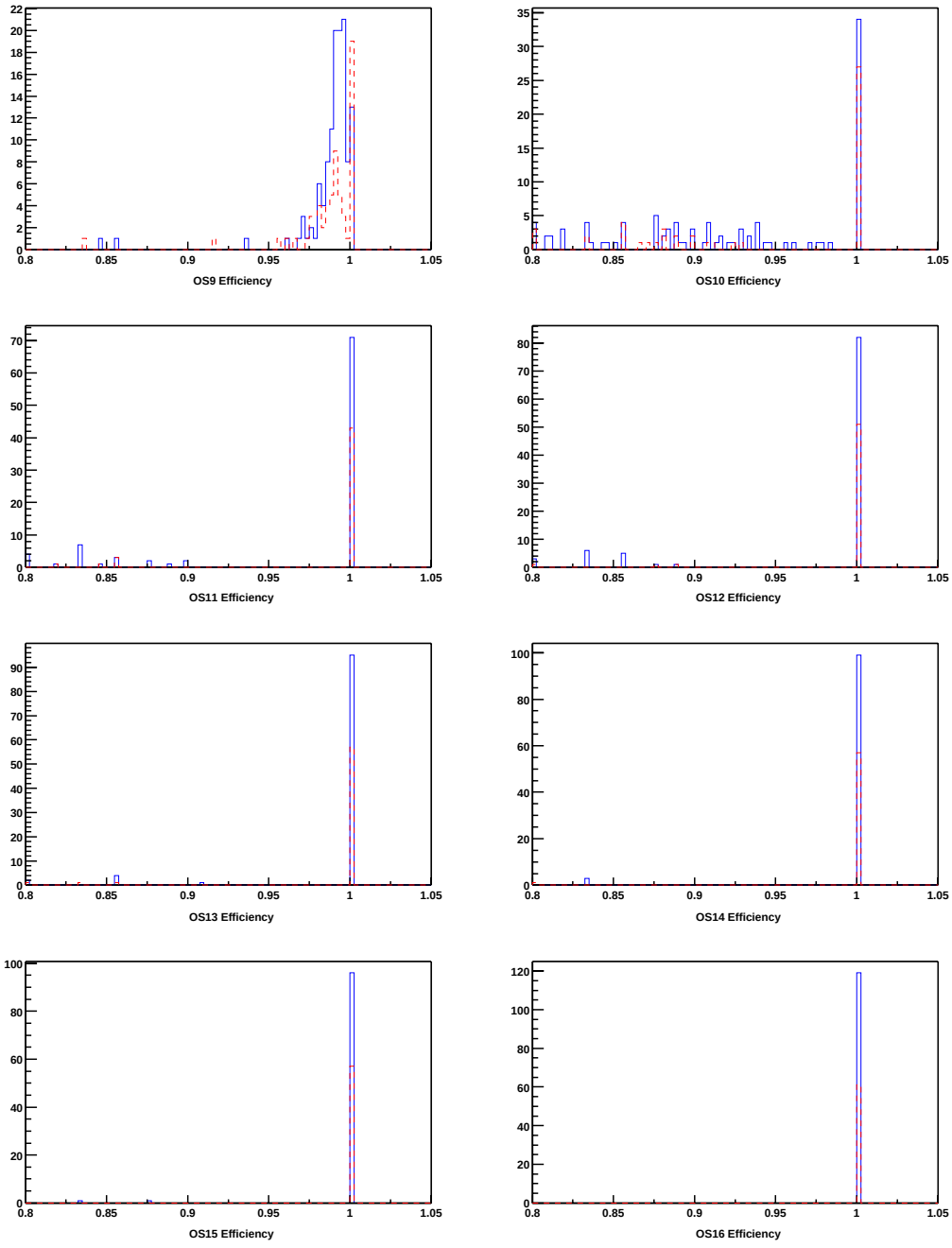


Figure 4.10: Distributions of OS9 to OS16 counter efficiency for positive runs (line) and negative runs (dash) superimposed.

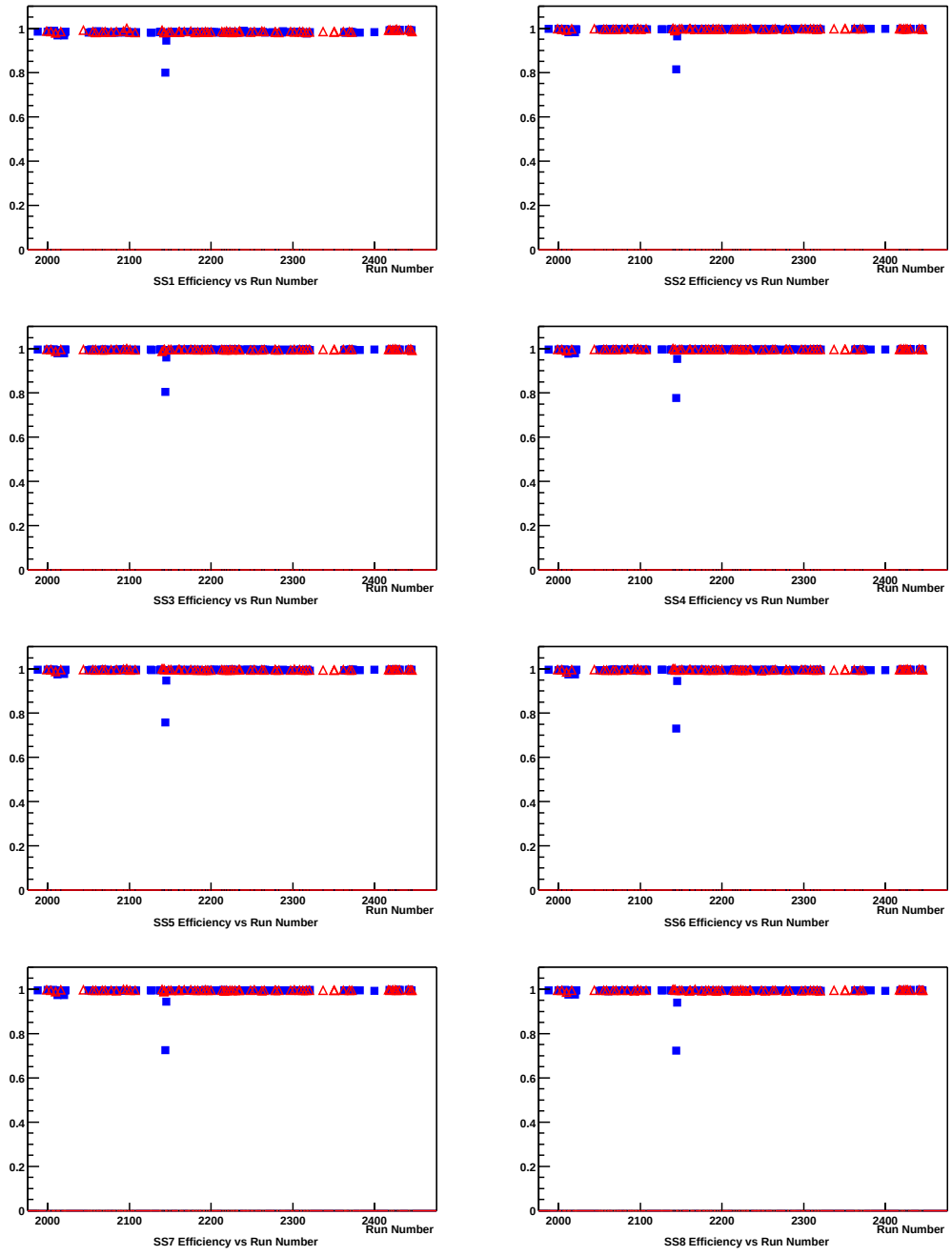


Figure 4.11: Efficiency of SS1 to SS8 versus run number for positive runs (square) and negative runs (open triangle).

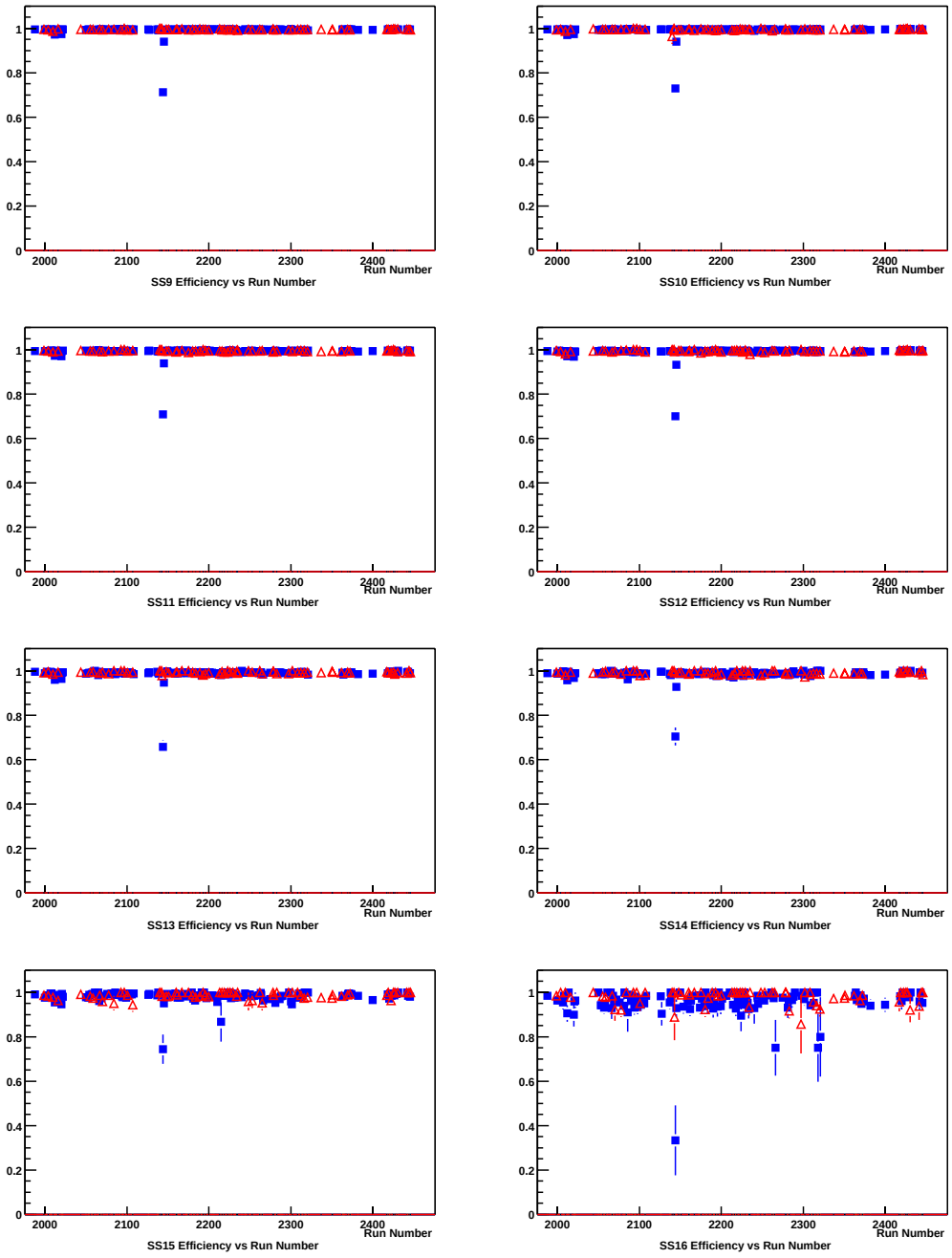


Figure 4.12: Efficiency of SS9 to SS16 versus run number for positive runs (square) and negative runs (open triangle).

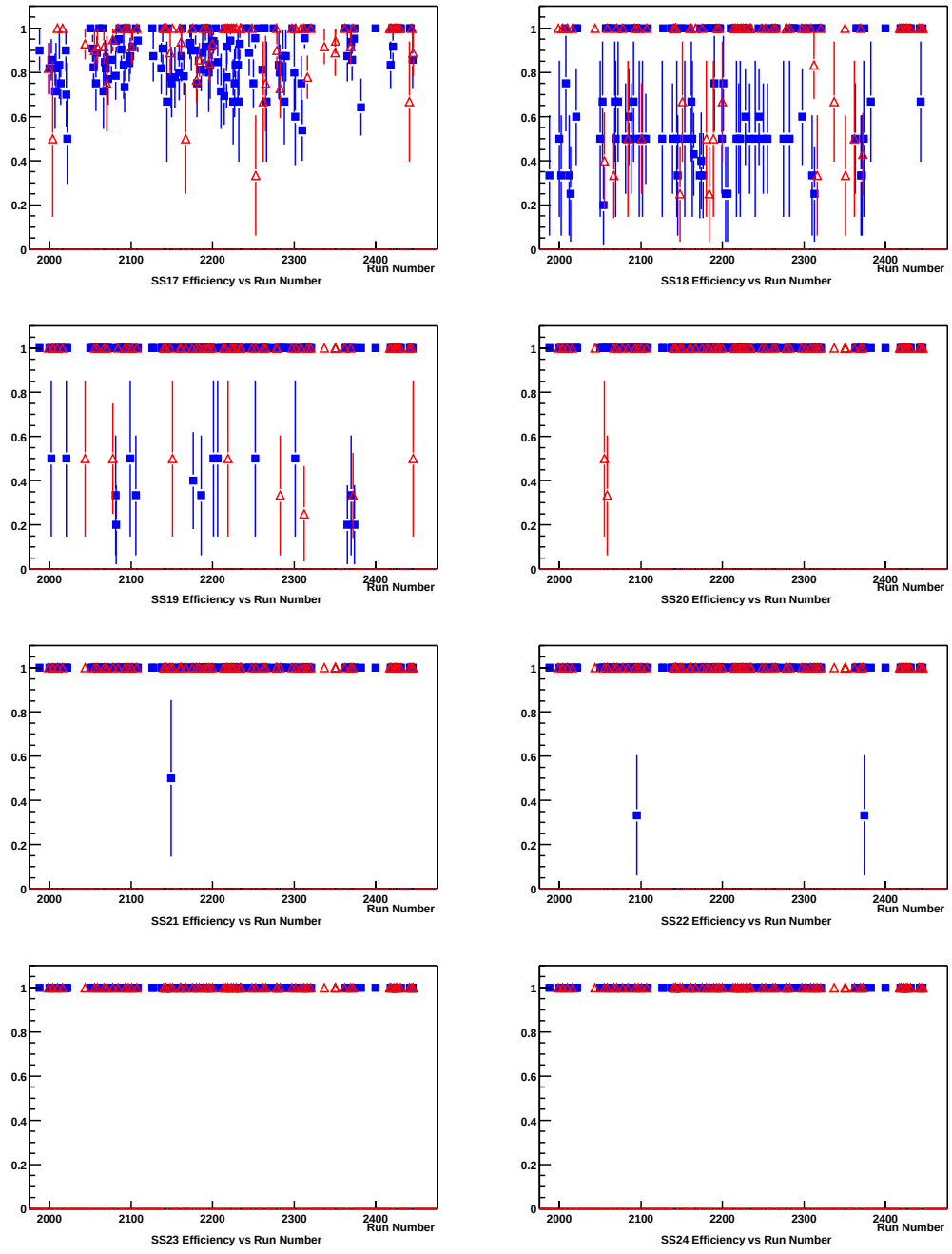


Figure 4.13: Efficiency of SS17 to SS24 versus run number for positive runs (square) and negative runs (open triangle).

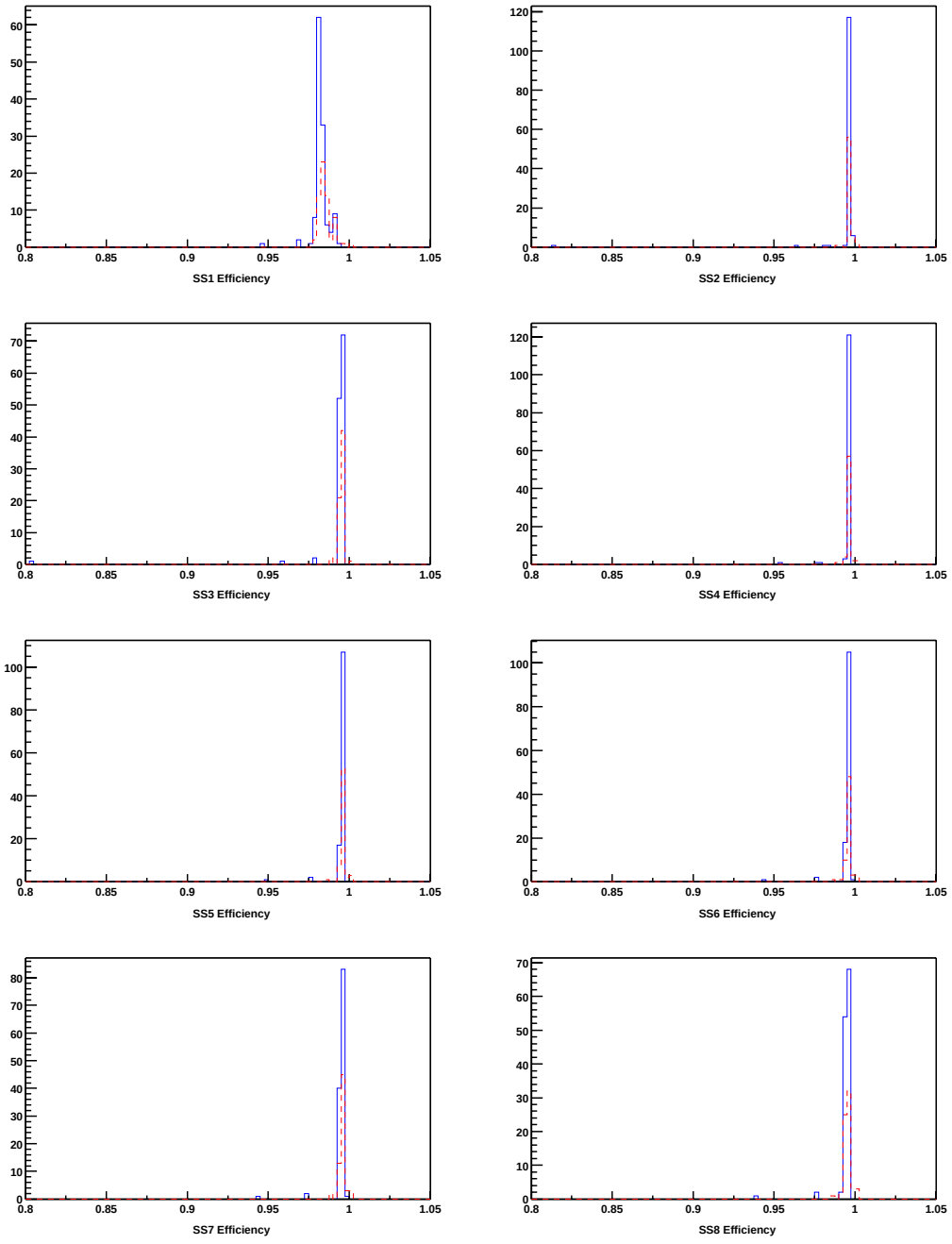


Figure 4.14: Distributions of SS1 to SS8 efficiency for positive runs (line) and negative runs (dash).

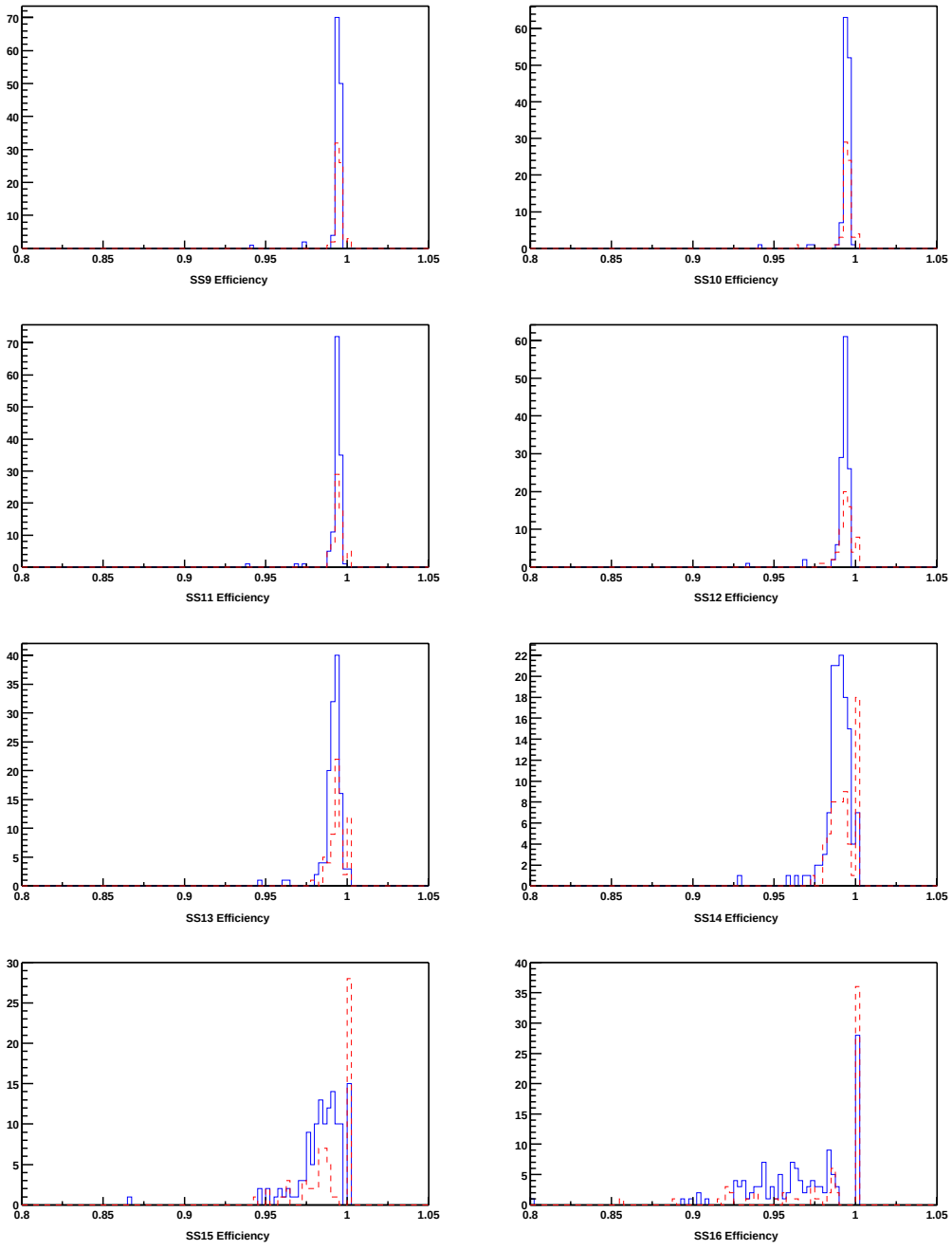


Figure 4.15: Distributions of SS8 to SS16 efficiency for positive runs (line) and negative runs (dash).

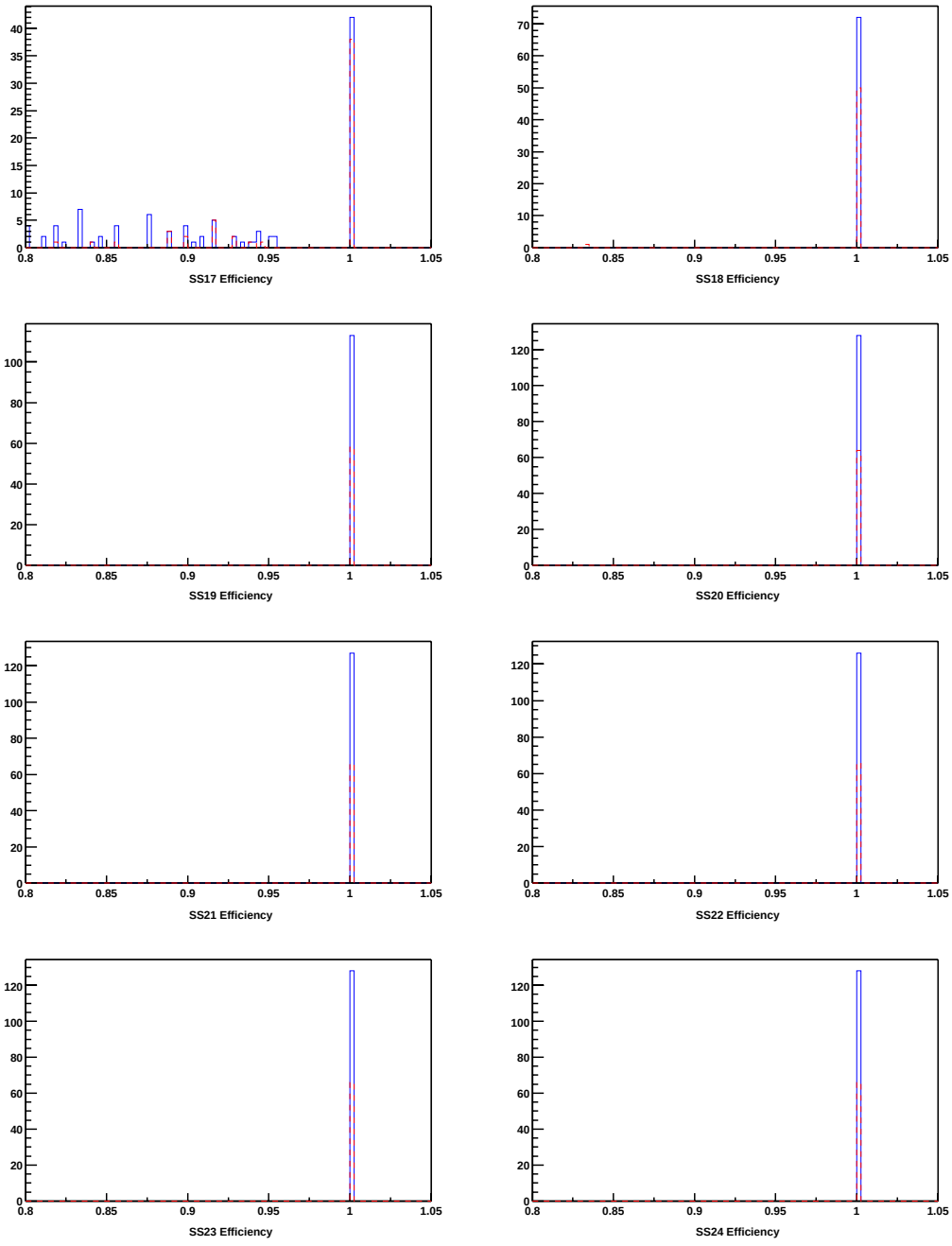


Figure 4.16: Distributions of SS17 to SS24 efficiency for positive runs (line) and negative runs (dash).

calculated by taking the ratio of two numbers. In the limit of large statistic, the variance of the efficiency goes to zero. Because the ratio is bounded by one, low statistic would bias the efficiency toward a lower value. Thus, some of the runs with significantly low statistics have lower efficiencies for the counters. In addition, counters near the edges of the position distributions of the pions at the locations of the hodoscopes have significantly low statistics resulting in lower efficiency. However, the efficiencies between the positive and negative runs seem to agree reasonably well, as shown in Figures 4.9, 4.10, 4.14, 4.15, and 4.16.

### 4.1.4 Efficiency of CALK Trigger

Figure 4.17 shows the efficiency of CALK trigger integrated over the fiducial of the calorimeter versus run number and its distribution. Figure 4.18 shows the turn-on momentum versus run number and its distribution. Similarly, plots for the efficiency of CALK trigger integrated over the momentum of the OS track and the turn-on X-position at the face of the calorimeter are shown in Figures 4.19 and 4.20.

The efficiency of the CALK trigger was around 98% and was fairly constant over the course of the run. In addition, the variations of the turn-on momentum and turn-on X-position at the face of the calorimeter are normally distributed and the standard deviations are about 0.25 GeV/c and 0.25 cm respectively. More importantly, the efficiency and turn-on distributions agrees reasonably well between the positive and negative runs.

## 4.2 Analysis Method

In general, the two most popular methods for parameter estimation in analysis are the Monte Carlo method and the maximum likelihood method. The Monte Carlo method requires detailed simulation of all variables in the experiment. Once a Monte Carlo event is accepted, it is weighted by a factor containing the unknown parameters. The accepted Monte Carlo events are then compared with the real events according to some $\chi^2$ criterion which is a function of the unknown parameters. By minimizing the $\chi^2$, hence requiring that the Monte Carlo data be the same as the real data, the unknown parameters are extracted. An obvious question that comes to mind is how well we can simulate the experiment. A priori, we have to assume some physics processes that closely resemble to what have been observed in the actual experiment. Considerable care must be taken to ensure that the

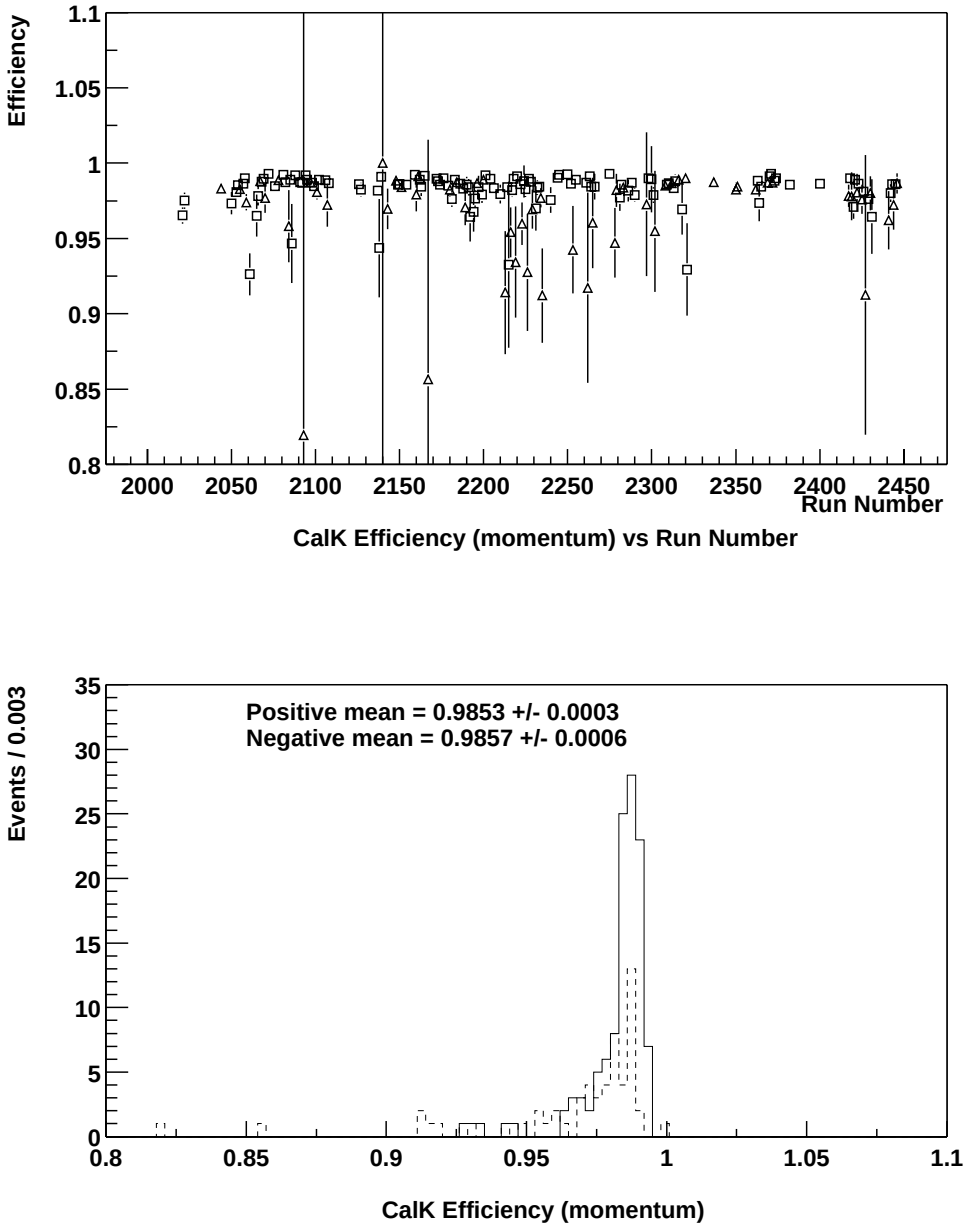


Figure 4.17: Efficiency of CALK trigger integrated over the fiducial of the calorimeter. The top plot shows the CALK efficiency versus run number for positive runs (open square) and negative runs (open triangle). The bottom plot shows their distributions for positive (line) and negative (dash) runs. The numbers are the weighted averages.

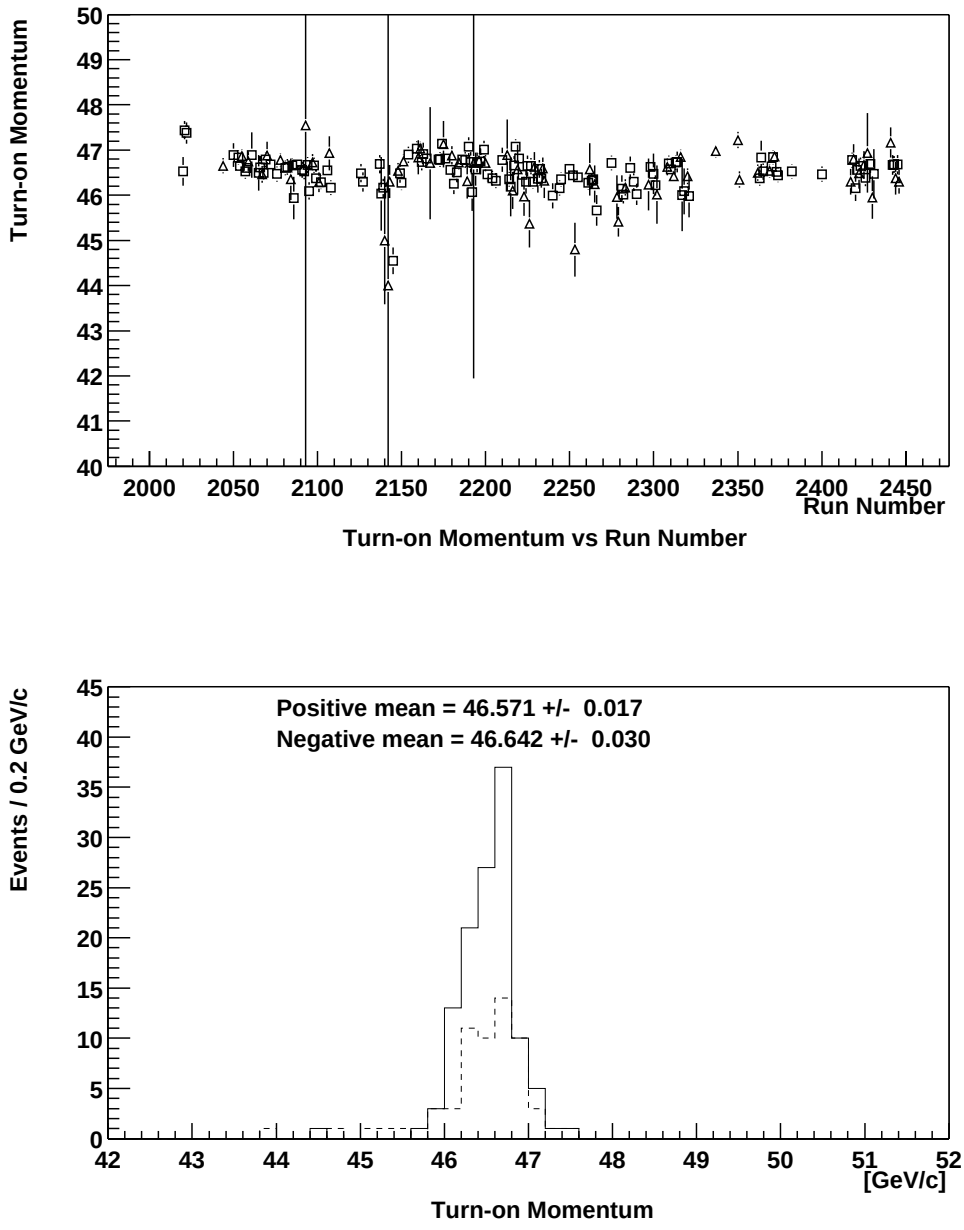


Figure 4.18: Turn-on momentum of CALK integrated over the fiducial of the calorimeter. The top plot shows the turn-on momentum versus run number for positive runs (open square) and negative runs (open triangle). The bottom plot shows the turn-on momentum for positive (line) and negative (dash) runs. The numbers are the weighted averages.

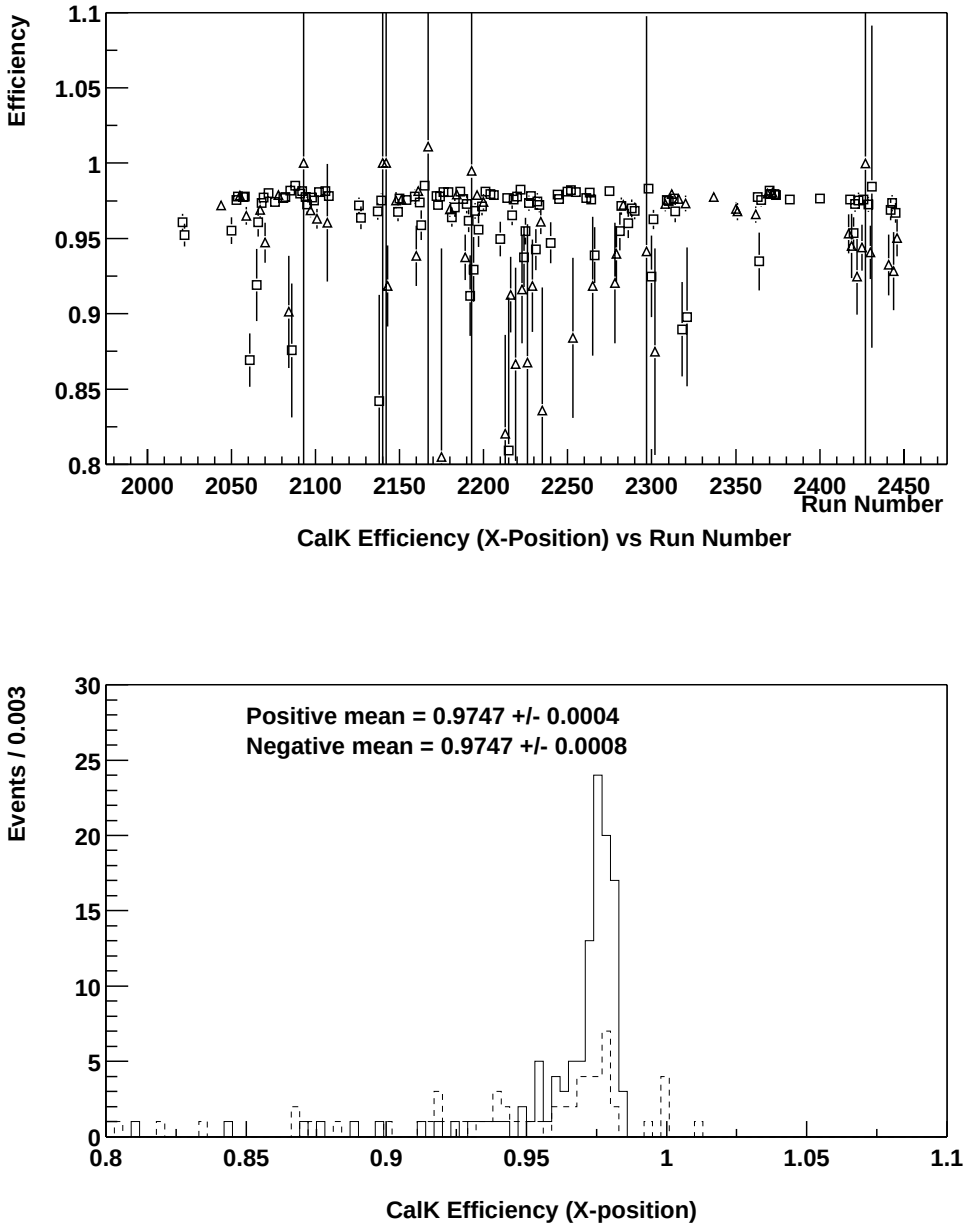


Figure 4.19: Efficiency of CALK trigger integrated over the momentum of the OS track. The top plot shows the efficiency versus run number for positive runs (open square) and negative runs (open triangle) superimposed. The bottom plot shows their distributions for positive (line) and negative (dash). The numbers are the weighted averages.

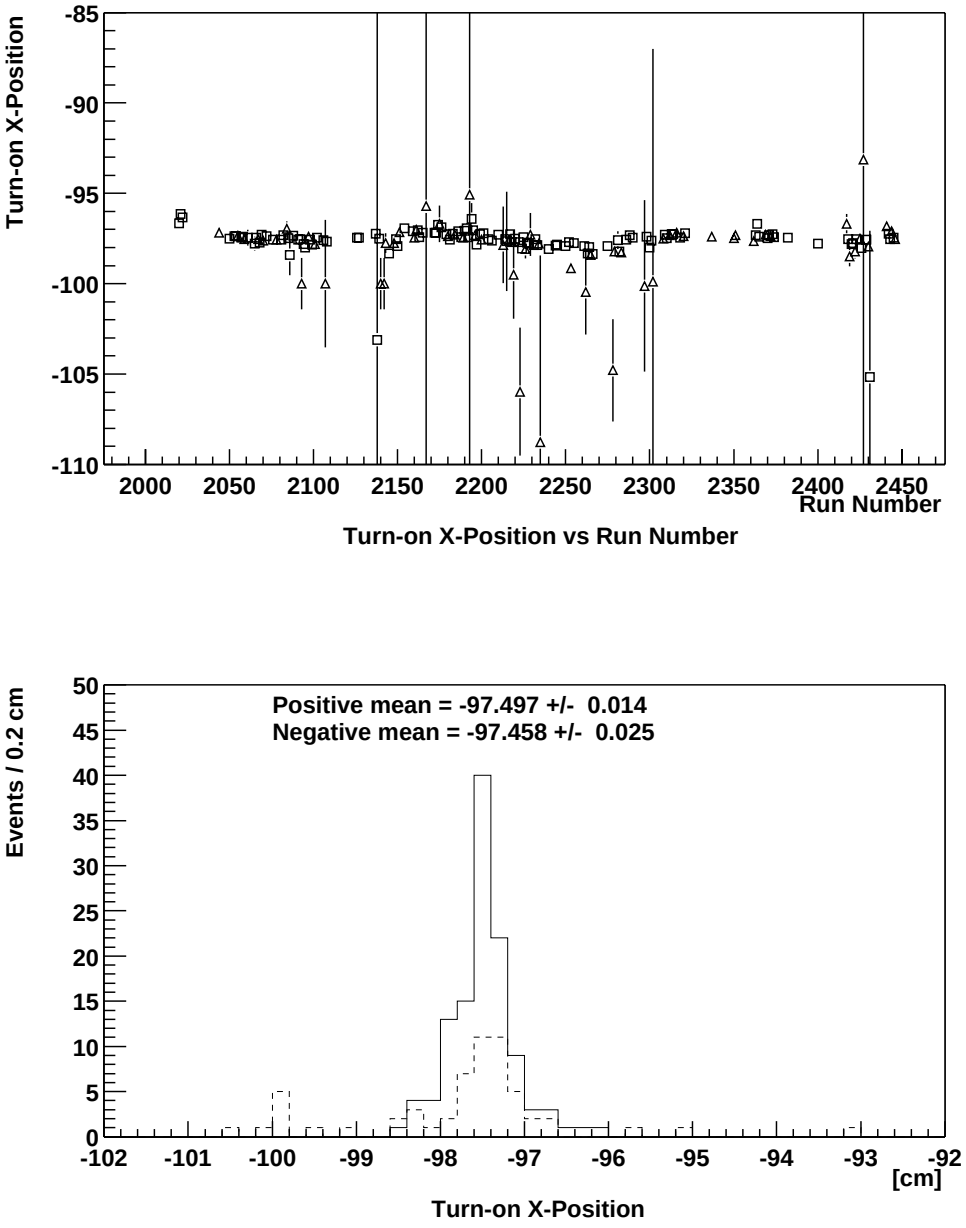


Figure 4.20: Turn-on X-position of CALK integrated over the momentum of the OS track. The top plot shows the turn-on X-position at the face of the calorimeter versus run number for positive runs (open square) and negative runs (open triangle) superimposed. The bottom plot shows their distributions for positive (line) and negative (dash). The numbers are the weighted averages.

simulated distributions match the real distributions well. Thus, a detailed simulation will be very time consuming.

On the other hand, in the maximum likelihood method, a likelihood function is defined as the product of the probability for each real event to occur. The likelihood function is then maximized to extract the unknown parameters. In order to calculate the probability, a Monte Carlo simulation is required to determine the acceptance of each event in the experiment. However, this time the event is simulated using all the variables from the data except the variables associated with the measurement that are varied to determine the acceptance of the event. The disadvantage of this method is that there is no criterion for the quality of the estimated parameters.

The hybrid Monte Carlo method [33] was developed to combine the likelihood and the Monte Carlo method. In the hybrid Monte Carlo method, only the variables associated with the measurement are simulated to determine the associated acceptance. The other variables of the hybrid Monte Carlo event are taken from the data. A $\chi^2$ comparison can then be made between the real and simulated distributions.

### 4.2.1 Hybrid Monte Carlo (HMC) Method

The hybrid Monte Carlo technique has been widely used in measuring the properties of hyperons [34], [35] and [36]. Here we apply the method to the $\tau$ decay of charged Kaon. The distribution of events in the Dalitz plot is represented by Equation 1.16 where the coefficients of the expansion are the unknown parameters that we are trying to estimate. We denote this equation as $P(X, Y; \alpha)$ where $\alpha$ refers to the vector of coefficients. Then the differential distribution can be written as

$$\frac{dN_r}{dX_r dY_r} = k_r A(X_r, Y_r) P(X_r, Y_r; \alpha), \tag{4.2}$$

where $k_r$ is a normalization constant and $A$ is the acceptance function of the spectrometer which we want to unfold before extracting the unknown parameters.

To determine $A$, a sample of HMC events is created by generating $X$ and $Y$ uniformly over their allowed phase space while taking the other parameters (secondary beam momentum, decay vertex and the orientation of the decay particles) from the real event. This HMC distribution can be written as

$$\frac{dN_f}{dX_f dY_f} = k_f A'(X_f, Y_f) \int \frac{dN_r}{dX_r dY_r} dX_r dY_r, \tag{4.3}$$

where $k_f$ is a normalization constant and $A'$ is the acceptance of the HMC events as calculated by the HMC method. Each HMC event should be weighted by $w(X_r, Y_r, X_f, Y_f)$ such that the fake distribution matches the real distribution. Thus, Equation 4.3 becomes

$$\frac{dN_f}{dX_f dY_f} = k_f A'(X_f, Y_f) \int \frac{dN_r}{dX_r dY_r} w(X_r, Y_r, X_f, Y_f) dX_r dY_r. \tag{4.4}$$

In principle, $A = A'$ if the geometric acceptance, trigger requirements and other acceptance requirements are simulated correctly in the HMC method. Since we want the HMC distribution to match the real distribution, Equation 4.4 has to reduce to Equation 4.2 after integrating over all the real events. Thus, the weight $w$ must have the form

$$w(X_r, Y_r, X_f, Y_f) = \frac{P(X_f, Y_f; \alpha)}{P(X_r, Y_r; \alpha)}. \tag{4.5}$$

For each real event, a constant number of accepted HMC events, $N_0$, is generated. In order to compare the real distribution to the HMC distribution, a $\chi^2$ can be formed. By dividing the Dalitz plot into cells (13 divisions along $X/\sqrt{3}$ and 26 divisions along $Y$ with a cell size of 0.1 by 0.1) and take $N_0$ to be much greater than one, the $\chi^2$ has the form

$$\chi^2 = \sum_{i,j} \frac{(N_{r,ij} - W_{ij}/N_\circ)^2}{N_{r,ij}}, \tag{4.6}$$

where $N_{r,ij}$ is the number of real events in the $(i, j)$ cell of the Dalitz plot, $W_{ij}$ is the number of HMC events in the $(i, j)$ cell of the Dalitz plot and is given by

$$W_{ij} = \sum_{r,f} w(X_r, Y_r, X_f, Y_f), \tag{4.7}$$

where the sum is over each real event $r$ and each fake event $f$ such that $X_f$ and $Y_f$ falls in the $(i, j)$ cell of the Dalitz plot.

From Equation 1.16, $w(X_r, Y_r, X_f, Y_f)$ can be written as

$$w(X_r, Y_r, X_f, Y_f) = \frac{1 + gY_f + hY_f^2 + kX_f^2}{1 + gY_r + hY_r^2 + kX_r^2}. \tag{4.8}$$

In order to express the $\chi^2$ as an analytic function of the unknown parameters $(g, h, k)$, $w(X_r, Y_r, X_f, Y_f)$ can be expanded in a Taylor series since $(gY + hY^2 + kX^2) < 1$. Equation 4.8 then becomes

$$\begin{aligned} w(X_r, Y_r, X_f, Y_f) = 1 \quad &+ \quad (Y_r - Y_f) \sum_{m=1,n=0,l=0} (-1)^{m+n+l} \frac{(m+n+l-1)!}{(m-1)!n!l!} Y_r^{m+2n-1} X_r^{2l} g^m h^n k^l \\ &+ \quad (Y_r^2 - Y_f^2) \sum_{m=0,n=1,l=0} (-1)^{m+n+l} \frac{(m+n+l-1)!}{m!(n-1)!l!} Y_r^{m+2n-2} X_r^{2l} g^m h^n k^l \\ &+ \quad (X_r^2 - X_f^2) \sum_{m=0,n=0,l=1} (-1)^{m+n+l} \frac{(m+n+l-1)!}{m!n!(l-1)!} Y_r^{m+2n} X_r^{2(l-1)} g^m h^n k^l. \end{aligned} \tag{4.9}$$

The parameters $(g, h, k)$ are determined by minimizing the $\chi^2$ function.

### 4.2.2 Generating Hybrid Monte Carlo Event

For a given real event, the hybrid Monte Carlo events are produced by generating $X$ and $Y$ uniformly over their allowed phase space. For each HMC event, the variables $X$ and $Y$ are expressed in terms of polar coordinates $r$ and $\phi$ as

$$X = \frac{2}{\sqrt{3}}\frac{m_{3\pi}}{m_\pi^2}Qr sin\ \phi, \tag{4.10}$$

$$Y = -\frac{2}{3}\frac{m_{3\pi}}{m_\pi^2}Qr cos\ \phi, \tag{4.11}$$

where $m_{3\pi}$ is the $3\pi$ invariant mass of the real event, $m_\pi$ is the mass of the pion, and $Q = m_{3\pi} - 3m_\pi$. The boundary of the Dalitz plot is given by

$$1 - (1+\delta)r^2 - \delta r^3 cos\ 3\phi = 0, \tag{4.12}$$

where $\delta = \frac{2Q}{m_{3\pi}}(2 - \frac{Q}{m_{3\pi}})^{-2}$. Only events with $X$ and $Y$ that fall within 90% of the boundary are accepted to avoid any edge effect due to resolution.

The kinetic energies of the decay particles can be calculated as follows:

$$T_3 = \frac{1}{2m_{3\pi}}\left[(m_{3\pi} - m_3)^2 - s_0 - m_\pi^2 Y\right], \tag{4.13}$$

$$T_2 = \frac{1}{2}\left[Q - T_3 + \frac{1}{2m_{3\pi}}\left(m_\pi^2 X + 2m_{3\pi}(m_1 - m_2) - (m_1^2 - m_2^2)\right)\right], \tag{4.14}$$

$$T_1 = Q - T_2 - T_3, \tag{4.15}$$

where $m_1$, $m_2$ and $m_3$ are the masses of the decay particles which are equal to $m_\pi$. The magnitude of the momentum is then calculated using

$$|\mathbf{p}_i| = \sqrt{T_i^2 + 2m_i T_i}\ ,\ i = 1, 2, 3. \tag{4.16}$$

With the magnitudes of the momenta known, the opening angles between the decay particles are given by

$$\theta_{12} = \frac{|\mathbf{p}_3^2| - |\mathbf{p}_1^2| - |\mathbf{p}_2^2|}{2|\mathbf{p}_1^2||\mathbf{p}_2^2|}, \tag{4.17}$$

$$\theta_{13} = \frac{|\mathbf{p}_2^2| - |\mathbf{p}_1^2| - |\mathbf{p}_3^2|}{2|\mathbf{p}_1^2||\mathbf{p}_3^2|}, \tag{4.18}$$

$$\theta_{23} = \frac{|\mathbf{p}_1^2| - |\mathbf{p}_2^2| - |\mathbf{p}_3^2|}{2|\mathbf{p}_2^2||\mathbf{p}_3^2|}. \tag{4.19}$$

So far, we have generated three pions that lies in a plane with known momenta and opening angles in the center-of-mass frame. To complete the generation, we need three Euler angles to put this plane in a uniquely defined orientation. The three Euler angles are taken from the real event. Two of the Euler angles $(\theta_3, \phi_3)$ are taken from the polar angle and the azimuth angle of the opposite-sign pion. To find the final Euler angle, the orientation of the real event is rotated such that the z-axis points in the direction of the opposite-sign pion. In this reference frame, the azimuth angle $(\phi_s)$ of the lower momentum pion of the two like-sign pions is taken as the third Euler angle.

After we achieve the orientation defined by the real event, we have completely generated the HMC event in the center-of-mass frame. Now we can boost this HMC event to the laboratory frame using the momentum of the reconstructed invariant mass. Then, we can assign the reconstructed decay vertex to the HMC event. The HMC event is accepted if the event passes all the simulated geometric apertures of the spectrometer as used in selecting the events for analysis.

## 4.3 Feasibility of Hybrid Monte Carlo Method

### 4.3.1 Monte Carlo (MC) Events

To validate the hybrid Monte Carlo method, a detailed Monte Carlo program was used to generate events under controlled conditions. The charged Kaon was generated at the target using a production model that will be described in Section 4.5.1. The charged Kaon was tranported through the collimator under a constant magnetic field. The decay of the charged Kaon was achieved with a three-body decay generator that was weighted by the square of the transition amplitudes as given in Equation 1.16 with known $g$, $h$ and $k$ values. The decay particles were then propagated through the spectrometer with multiple scattering effects simulated. In addition, when doing the feasibility and systematic studies, detector efficiencies, accidental hits in the MWPCS, interaction of particles with the spectrometer material, and/or trigger simulation were also included in the event generation.

There are three ways in which these MC events can be passed as input to the HMC program. To make matter clearer, we shall distinguish them by the terms:

1. *generated input*

   The generated values of the MC event are passed to the HMC program without any

reconstruction.

2. *biased generated input*

   The generated values of the successfully reconstructed MC event are passed to the HMC program.

3. *reconstructed input*

   The reconstructed values of the MC event are passed to the HMC program.

Using *generated input*, we would be able to demonstrate the working principle of the HMC method. In practice, the reconstruction algorithm is not perfect, even ideal MC events can be mis-reconstructed and rejected. So, in principle the number of events in *biased generated input* must be less than in *generated input*, hence the term *biased*. Using *biased generated input*, the effect of reconstruction on the HMC method can be studied. In addition, by comparing the results of *biased generated input* and *reconstructed input*, the effect of resolution of the spectrometer on the HMC method can be investigated.

Figure 4.21 shows the results for two cases of *generated input*, one with uniform Dalitz distribution, the other with non-zero $g$, $h$ and $k$. The HMC estimates are consistent within the statistical errors with the generated values, thus demostrating the feasibility of the HMC method.

Figure 4.22 shows the results of the three different ways in which MC events were passed to the HMC program. The MC events were generated with a uniform Dalitz distribution. The HMC estimates produced a bias with *biased generated input*. This is not surprising because in the HMC method, reconstruction was not performed, hence creating a bias between the real and the HMC distributions. We will study the effect of reconstructing the HMC event in Section 4.3.2. In addition, when *reconstructed input* was used, the HMC estimates is consistent with the estimates from *biased generated input*. This result indicates that the resolution of the spectrometer did not strongly affect the HMC estimates. We will further reinforce this fact in the Section 4.3.2 when we study the stability of the HMC estimates as a function of the spectrometer resolution.

We note that smearing due to resolution is proportional to the local slope of the distribution. So, one can argue that the HMC estimates in Figure 4.22 are not affected by the resolution of the spectrometer because the MC events are generated with a uniform Dalitz distribution. Figure 4.23 shows the results for a more realistic case. The MC events were

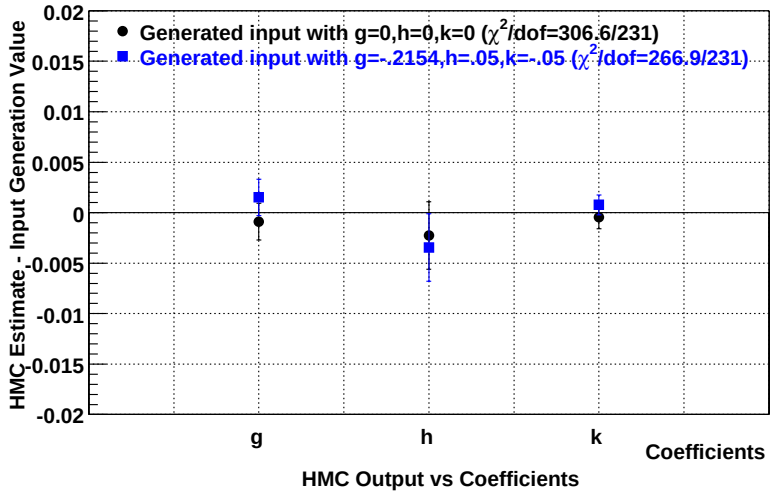


Figure 4.21: Difference between HMC estimates and generated values of coefficients g, h and k of *generated input* MC events.

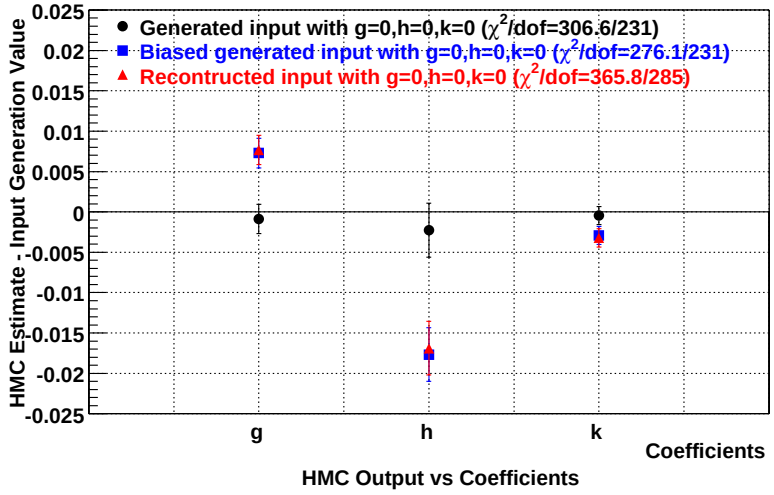


Figure 4.22: Difference between HMC estimates and input values of coefficients $g$, $h$ and $k$ with *generated input*, *biased generated input* and *reconstructed input* MC events for a uniform Dalitz distribution.

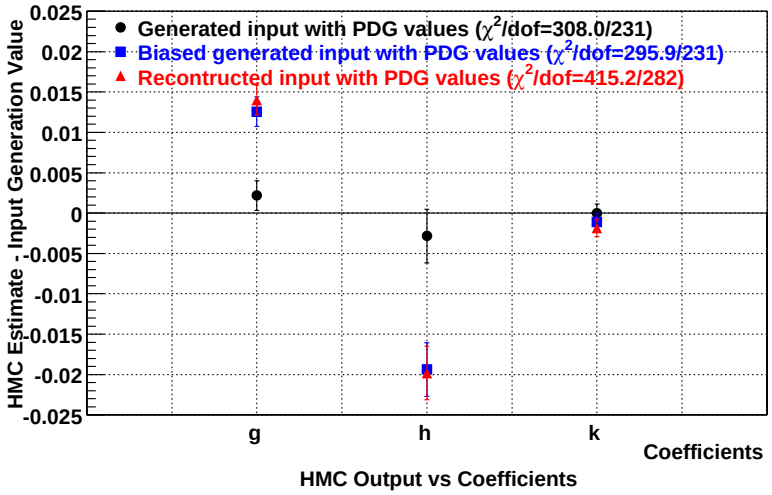


Figure 4.23: Difference between HMC estimates and input values of coefficients $g$, $h$ and $k$ with *generated input* (taken from PDG), *biased generated input* and *reconstructed input* MC events

generated with $g$, $h$ and $k$ values taken from the Particle Data Group (PDG) [14]. The conclusions remain the same, though the bias changes significantly.

### 4.3.2 Effects of Spectrometer Resolution

In Section 4.3.1, there was an indication that the spectrometer resolution did not affect the HMC estimates. In this subsection, we will try to study how robust this fact is by changing the spectrometer resolution and see how it affects the HMC estimates. Ideally, we would just want to change the spectrometer resolution without affecting any other things. But it is impossible to change the spectrometer resolution without affecting reconstruction efficiency. We try to minimize the effect on the reconstruction efficiency by increasing the wire spacing of the downstream wire chambers only. From now on, we shall ignore the coefficients $h$ and $k$. Only the results for the coefficient $g$ are discussed. Figures 4.24 and 4.25 show the difference between the HMC estimate and the generated value as a function of a scale factor used to change the wire spacings of the downstream wire chambers to decrease the resolution. As indicated in the figures, the HMC estimates are the same for *biased generated input* and *reconstructed input* reinforcing the fact that the spectrometer

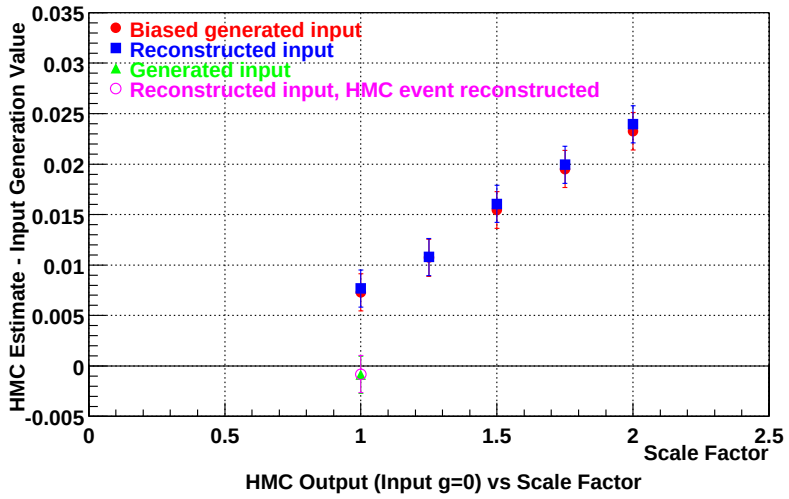


Figure 4.24: Difference between HMC estimates and input value of $g$ as a function of scale factor of wire spacings of downstream wire chambers for a uniform Dalitz distributions.

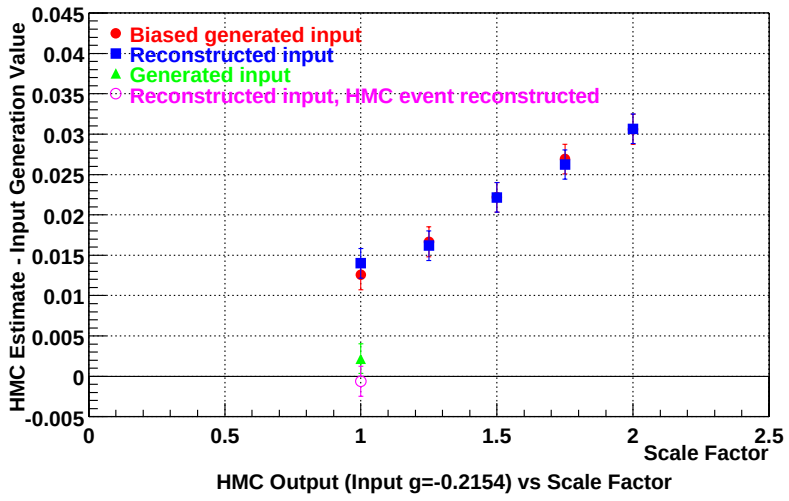


Figure 4.25: Difference between HMC estimates and input value of $g$ taken from PDG as a function of scale factor of wire spacings of downstream wire chambers.

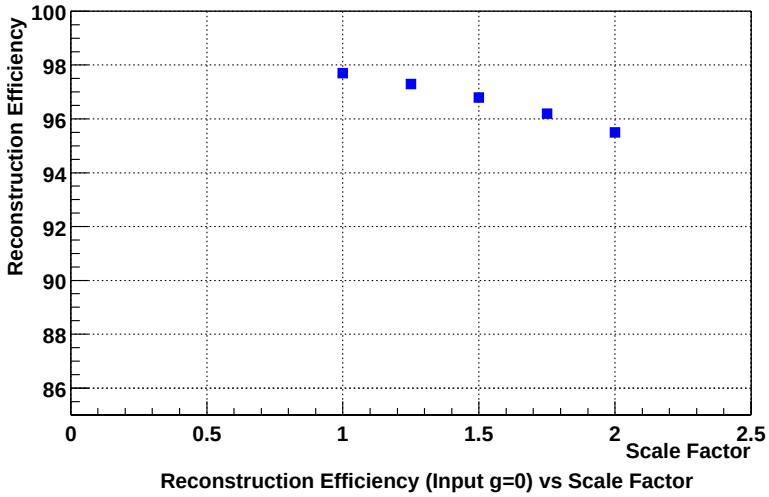


Figure 4.26: Reconstruction efficiency as a function of scale factor of wire spacings of downstream wire chambers for MC events generated with a uniform Dalitz distribution.

resolution does not affect the HMC estimates. On the other hand, the magnitude of the biases from the HMC estimates increases as the spectrometer resolution decreases. As shown in Figures 4.26 and 4.27 the reconstruction efficiency also changes as the wire spacings of the wire chambers are changed. Thus, the magnitude of the bias is correlated with the reconstruction efficiency.

So far, all pieces of evidence suggest that biases of the HMC estimates are related to biases in reconstruction. This fact can be verified by reconstructing the HMC events, hence simulating reconstruction in the HMC method. By reconstructing the HMC events, the HMC estimates are consistent with the generated values as shown by the open circles in Figures 4.24 and 4.25. Thus, the biases can be corrected for by reconstructing the HMC events.

### 4.3.3 Stability of the HMC estimates

#### Number of Accepted Fake Events

In the HMC method, we have to make a choice of how many HMC events to accept per one real event. Figure 4.28 shows the difference between the HMC estimate and the input value as a function of the number of HMC events generated. The bias is insensitive

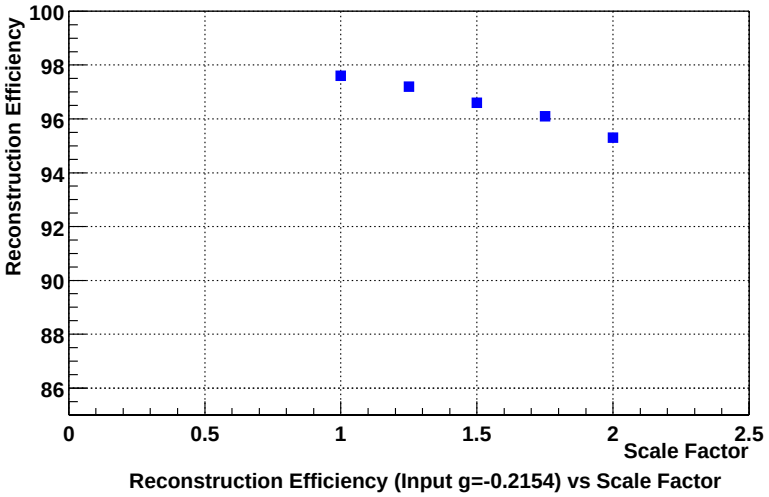


Figure 4.27: Reconstruction efficiency as a function of scale factor of wire spacings of downstream wire chambers for MC events generated with value of g taken from PDG.

to the number of HMC events generated. We decide to accept 5 HMC events per one real event for the analysis.

### Order of Expansion

In the HMC method, we have to make a choice as to what order of expansion of the weight $w$ in Equation 4.9 is sufficient. Figure 4.29 shows the difference between the HMC estimate and the input value as a function of the order of expansion. The bias is insensitive to the order of expansion. We decide to expand the weight up to the sixth order for the analysis.

### Input $g$ Value

Figure 4.30 shows the difference between the HMC estimates and the input values as a function of the $g$ value. The range of $g$ value was chosen to be around the PDG value for $g$ in steps of $5 \times 10^{-4}$. Essentially the bias is very insensitive to the input values.

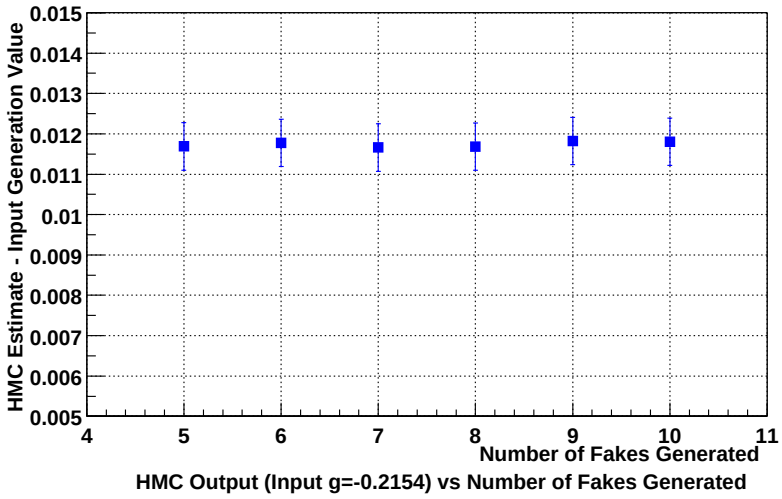


Figure 4.28: Difference between HMC estimates and input value of $g$ as a function of number of HMC events with *reconstructed input*.

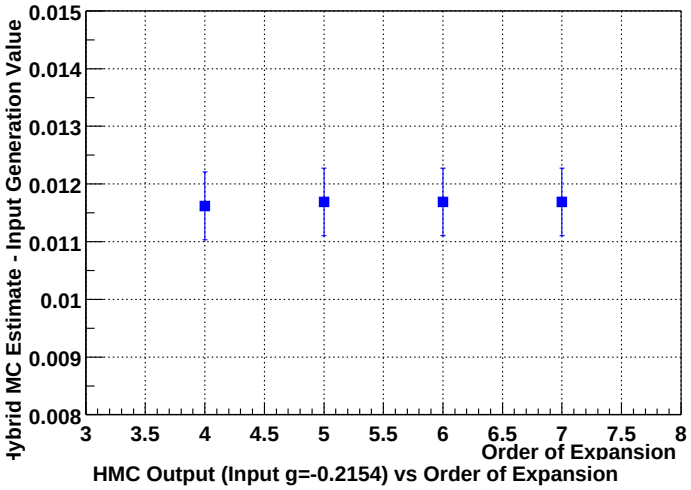


Figure 4.29: Difference between HMC estimates and input value of $g$ as a function of order of expansion with *reconstructed input*.

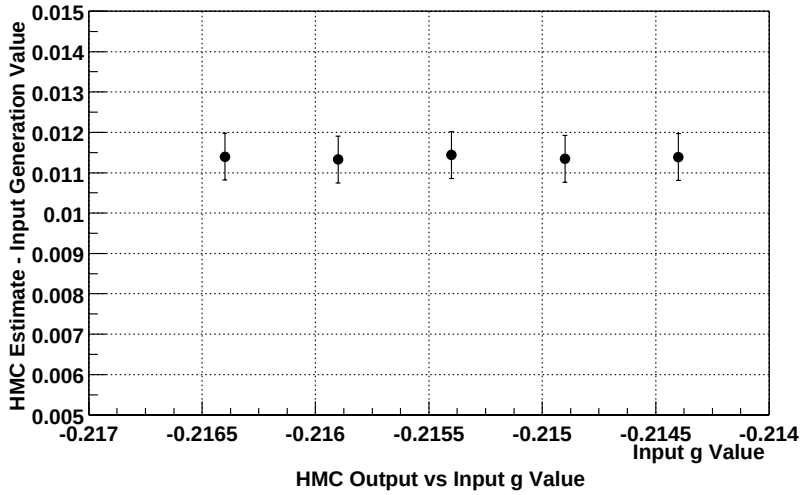


Figure 4.30: Difference between HMC estimates and input values as a function of input $g$ value with *reconstructed input*.

### Number of Events Analyzed

Since the numbers of $K^+$ and $K^-$ events are not the same, we want to know how sensitive the HMC estimates are to the number of events analyzed. The MC events were generated without any multiple scattering for this study and are labeled as *ideal* MC events. The black dots in Figure 4.31 show the difference between the HMC estimates and the input values as a function of the number of events analyzed. The bias is insensitive to the number of events analyzed.

### Multiple Scattering

Also shown in Figure 4.31 is a point where the *reconstruted input* was generated with multiple scattering consistent with the amount of material in the spectrometer. The result is consistent with that without multiple scattering. This is not surprising as the reconstrucion efficiency is insensitive to multiple scattering because all the track-finding cuts were loose enough to accomodate small deviation.

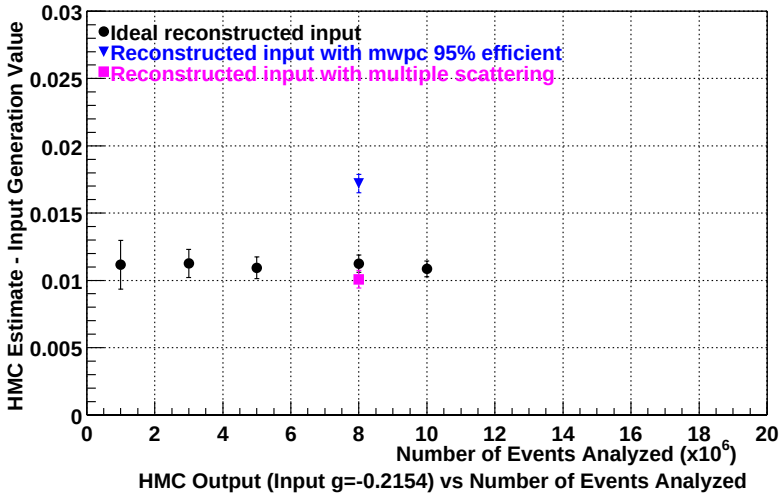


Figure 4.31: Difference between HMC estimates and input value of $g$ as a function of the number of events analyzed with *reconstructed input*. The plot also includes results with the MC events generated with different conditions.

### Beam Momentum of Kaon

Different slices of the momentum of the secondary beam were selected and passed to the HMC program. The width of the bin used for each slice was 10 GeV/c except for the last slice which had a width of 20 GeV/c in order to have comparable statistics as the other slices. Figure 4.32 shows the difference between the HMC estimates and the input value as a function of the momentum of the charged Kaon. The bias seems to increase with the momentum. This seems to correlate with the change in reconstruction efficiency as shown in Figure 4.33.

### Efficiency of Wire Chamber

To study the effect of the efficiency of the MWPCs on the HMC estimates, MC events were generated with uniform inefficiency across all the wire planes in the spectrometer. Figure 4.34 shows the difference between the HMC estimates and the input value as a function of the MWPC efficiency. The magnitude of the difference decreases as the wire chambers become more efficient. The bias is changed by $1 \times 10^{-3}$ for a 1% variation in the MWPC efficiency. As shown in Figure 4.35, the reconstruction efficiency decreases as the

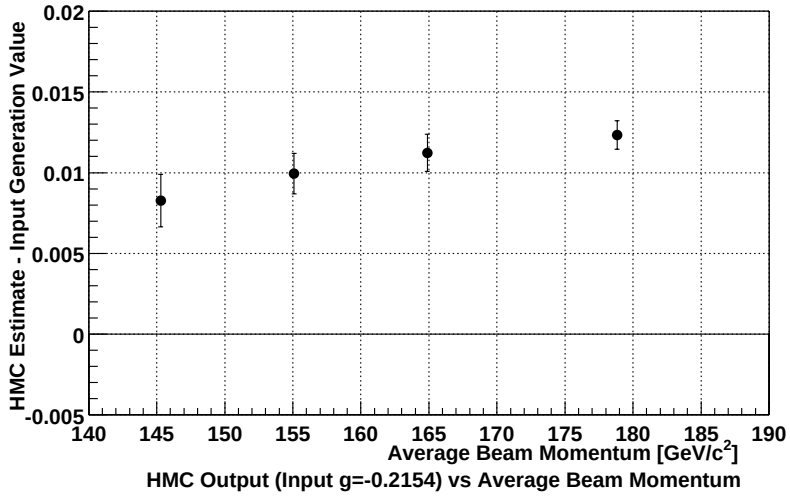


Figure 4.32: Difference between HMC estimates and input $g$ value as a function of charged Kaon momentum with *reconstructed input*.

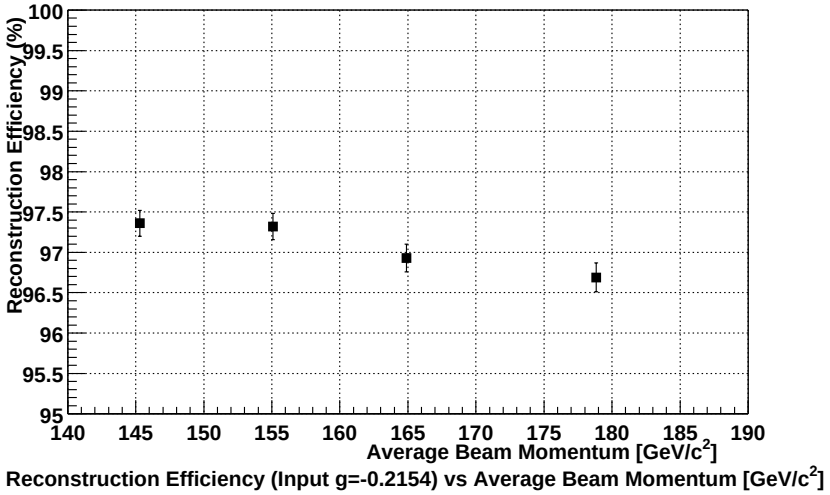


Figure 4.33: Reconstruction efficiency as a function of charged Kaon momentum.

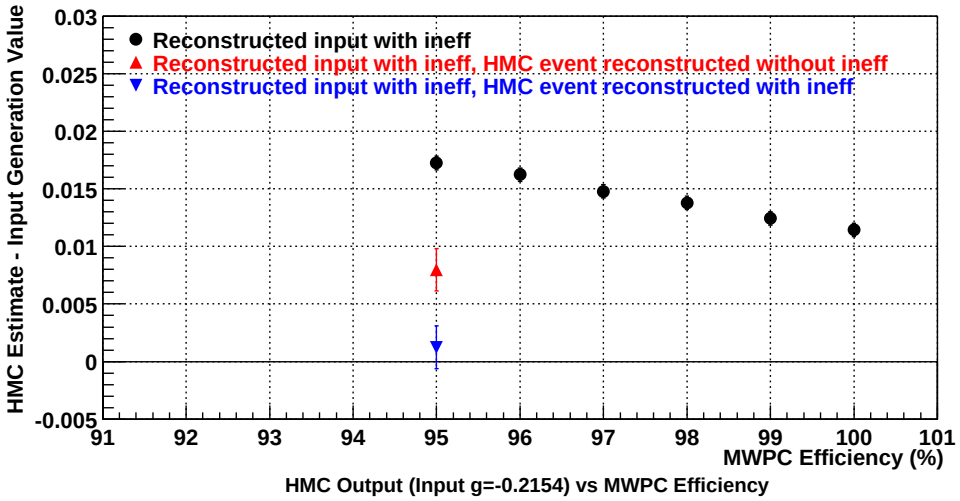


Figure 4.34: Difference between HMC estimates and input $g$ value as a function of the efficiency of MWPC with *reconstructed input*. Results for reconstructed HMC events are also shown.

MWPC efficiency drops. Thus, the change in the bias could be correlated with the change in reconstruction efficiency.

In order to verify that the bias is caused by reconstruction, the effect of reconstruction was simulated in the HMC method. This was done by tracing the HMC events through the spectrometer in the software with or without simulating wire chamber inefficiency, The positions where the tracks transverse the wire plane were then digitized and the HMC events were reconstructed. The results are shown in Figure 4.34. The HMC estimates are more than three standard deviations away from the input value when the HMC events were reconstructed without simulating wire chamber inefficiency as opposed to the input MC events. However, the HMC estimates are consistent with the input value when the same wire chamber inefficiency used for generating the input MC events is included in the HMC program because the acceptance of the HMC events are correctly simulated in this case.

### Efficiency of OS Counter

In this case, MC events were generated with different OS counter efficiency. Figure 4.36 shows the difference between the HMC estimates and the input value as a function of

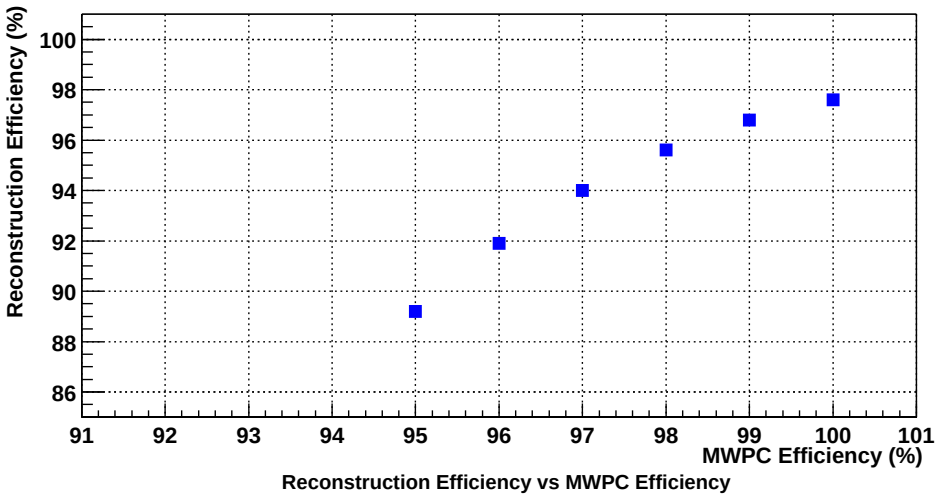


Figure 4.35: Reconstruction efficiency as a function MWPC efficiency.

the OS counter efficiency. There are two sets of results in Figure 4.36, one for the efficiency of the whole OS hodoscope that was varied uniformly and the other for only varying the efficiency of OS8. OS8 was chosen because it was closed to the mean of the X position of the opposite-sign pion at the hodoscope. The bias is less sensitive to the efficiency of the whole OS hodoscope than to the efficiency of a specific OS counter. By varying the efficiency of the whole OS hodoscope, the effect is essentially the same as prescaling the number of events because there was only one OS track to trigger on, hence we do not expect the bias to change. On the other hand, if only the efficiency of an OS counter is changed, events are removed non-uniformly in the Dalitz plot, causing the bias to change.

### Efficiency of SS Counter

Similar to the study with the OS hodoscope, Figure 4.37 shows the difference between the HMC estimates and the input value as a function of the SS counter efficiency. In the case of investigating the effect of a single counter, the efficiency of SS12 was changed. SS12 was chosen because it was closed to the mean X position of the same-sign pions at the hodoscope. In contrast to the OS hodoscope, the bias is more sensitive to the efficiency of the whole SS hodoscope than to that of a specific SS counter.

The dependence of the bias on the efficiency of the SS hodoscope can be explained by

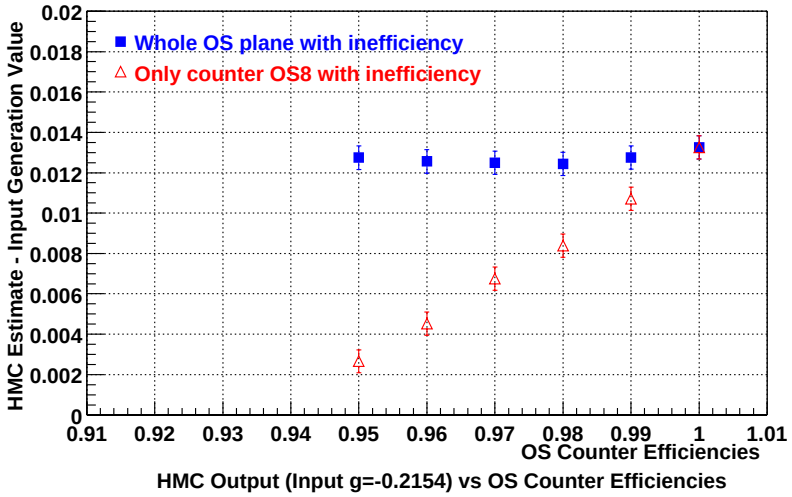


Figure 4.36: Difference between HMC estimates and input $g$ value as a function of OS counter efficiency with *reconstructed input*.

the fact that the acceptance of the charged Kaon decays is not perfect. Recall that only SS2 to SS18 were used in the K trigger. If only a single same-sign pion was required to trigger the SS hodoscope, the acceptance of the Kaon events was about 98.8%, very good but not perfect. If the efficiency of the whole SS hodoscope is changed, we introduce a non-uniform variation in the Dalitz distribution causing the bias to change. On the other hand, since the inefficiency of each of the SS counters was less than a percent as indicated in Figure 3.24, the probability of both same-sign pions not setting a SS counter was small. Because the trigger only required at least one same-sign particle, the bias is less sensitive to the variation of the efficiency of a SS counter.

## 4.4 Analysis Strategy

As already stated in Section 4.2.1, the acceptance function $A(X_r, Y_r)$ of the real events and $A'(X_f, Y_f)$ of the accepted HMC events are assumed to be the same. Therefore, the efficiencies of the detectors have to be understood well in order to come up with the correct acceptance function. But this can be a difficult task. In addition, we have shown that the HMC estimate is biased if the HMC events are not reconstructed. We can correct for this

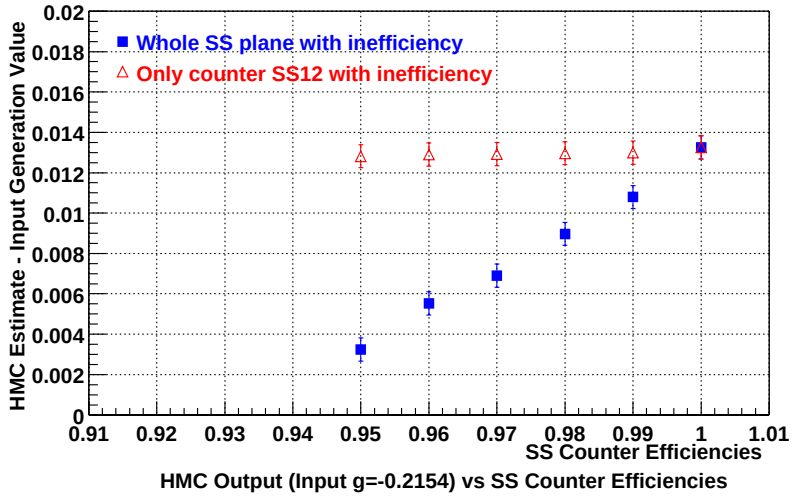


Figure 4.37: Difference between HMC estimates and input $g$ value as a function of SS counter efficiency with *reconstructed input*.

reconstruction bias in one of the following two methods: (1) reconstruct the accepted HMC events; or (2) correct the Dalitz distribution of the real data with the acceptance calculated with MC. Both methods would require detailed MC simulation, and reconstructing the HMC events is computing intensive.

Is it really nesessary to correct for the bias? If the biases from the positive and the negative data are the same then it is not necessary to correct for the bias because the measurement is an asymmetry determination and the biases cancel out. We know that the biases are not necessarily identical as we have already shown that the bias is fairly sensitive to certain variables. However, we can still take advantage of the cancellation of biases if the difference in the biases is small. Therefore, we have to show that any difference between the positive and negative data that can result in a false asymmetry is comparable to or below the sensitivity of the measurement. This is the study of systematic effects which is the subject of the next section.

## 4.5 Systematic Errors

Any difference between the positive and negative data resulting in a difference in the acceptance could lead to a systematic error in the HMC estimate. It is important to estimate how sensitive the HMC estimate is to the various differences that exist between the positive and negative data. The systematic errors are estimated by first quantifying the differences between the positive and negative data. Then two independent samples of MC events are generated, reconstructed and analyzed with the first sample simulating the positive data and the second sample simulating the negative data. The difference between the HMC estimates from the two MC samples is an estimate of the systematic error from a particular source under study.

Due to time restriction and limited computing resources, only 30 million MC events were generated for each sample for the systematic study. These MC events were reduced by 60% after applying all the analysis cuts.

### 4.5.1 Secondary Beam

The momentum spectra of $K^+$'s and $K^-$'s exiting the collimator were slightly different due to different production mechanism. In order to match the accepted MC Kaon beam with the data, an overly simplified model was used to simulate the production. The model assumes the invariant cross-section was proportional to $e^{-p_T^2/b}(1-x_F)^n$, where $p_T$ is the transverse momentum, $x_F$ is the Feynman x which is the fraction of allowable longitudinal momentum of the produced particle in the center-of-mass system of the incident proton and the target nucleon, and $b$ and $n$ depend on the production dynamics but are tunable parameters in this study.

Figures 4.38 and 4.39 show the comparisons of momentum components and positions distributions at the exit of the collimator for the $K^+$ and $K^-$ data with the MC events respectively. The agreement between the data and the MC is not perfect due to the overly simplified model used to simulate the production. But the general features of the distributions agree reasonably well. It is the difference that will ultimately determine the systematic error. By analyzing the MC events that simulated the positive and negative data samples separately, the difference in the HMC estimates on $g$ between the two samples is $(1.6 \pm 1.9) \times 10^{-3}$, consistent with zero.

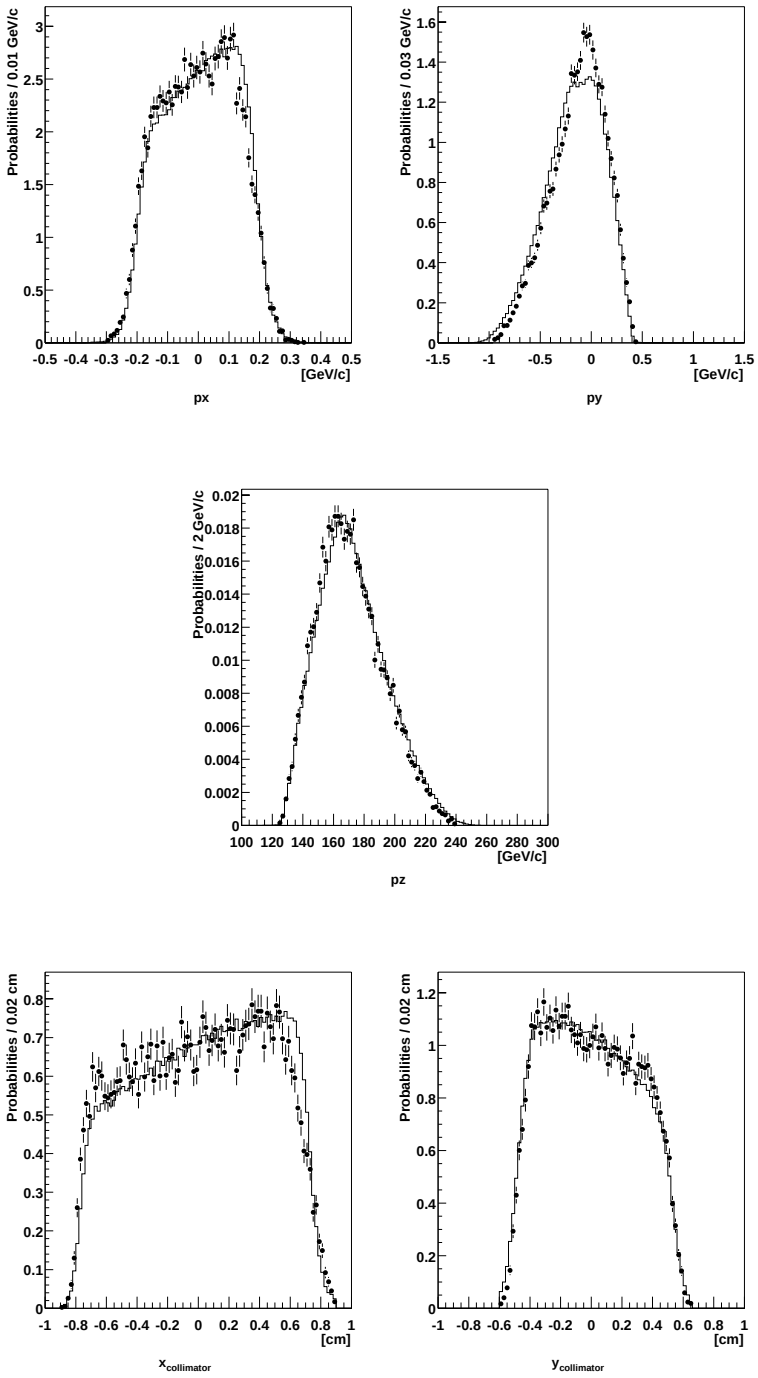


Figure 4.38: Comparisons of momentum components ($p_x$, $p_y$, $p_z$) and positions ($x_{collimator}$, $y_{collimator}$) of $K^+$ at the exit of the collimator for data (histograms) and MC (dots).

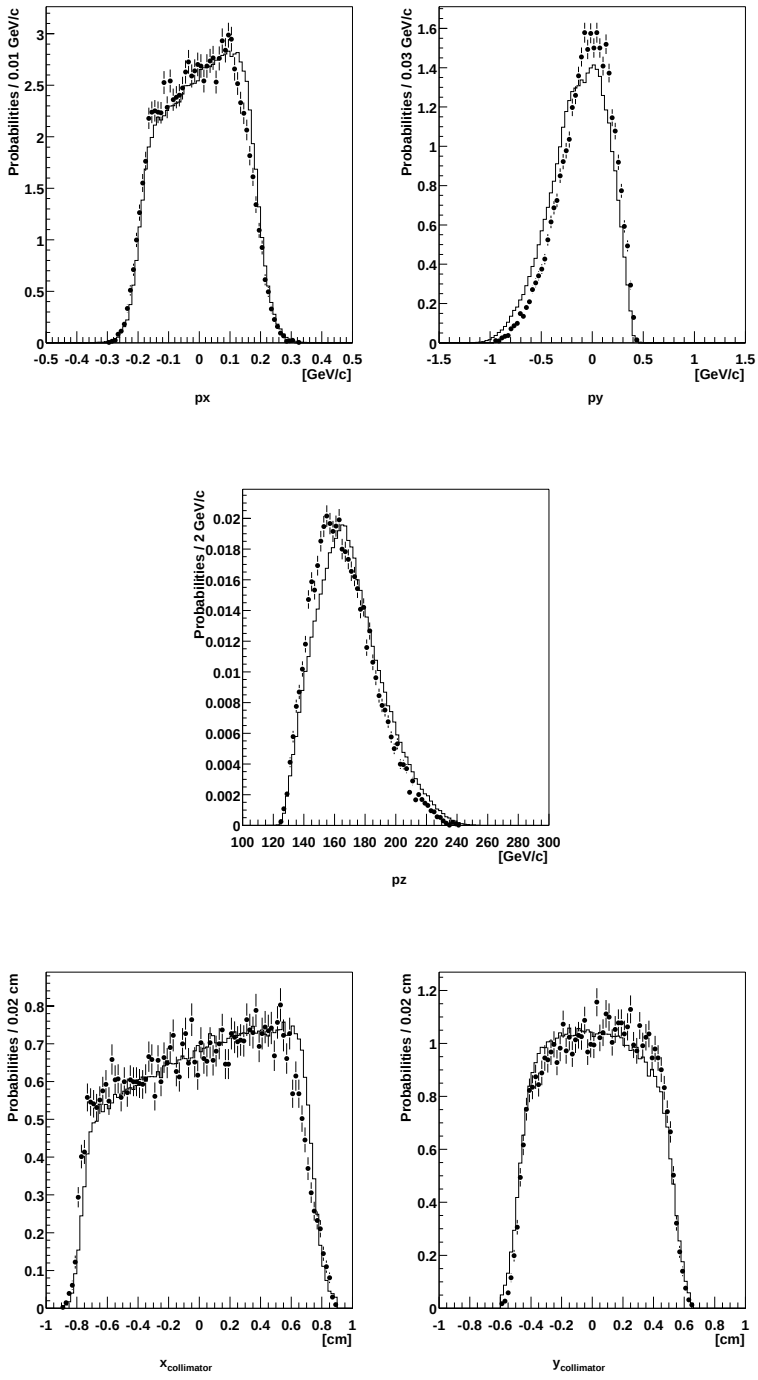


Figure 4.39: Comparisons of momentum components ($p_x$, $p_y$, $p_z$) and positions ($x_{collimator}$, $y_{collimator}$) of $K^-$ at the exit of the collimator for data (histograms) and MC (dots).

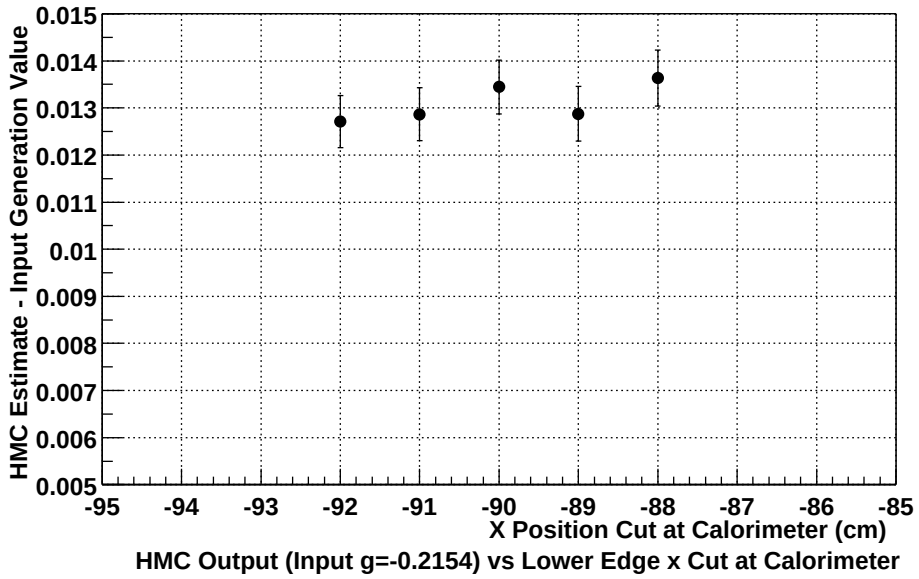


Figure 4.40: Difference between HMC estimates and input $g$ value as a function of the $x_{calorimeter}$ cut.

### 4.5.2 Fiducial of Calorimeter

It was required that the X projection of the OS track at the upstream surface of the calorimeter be greater than $x_{calorimeter} = -90.0$ cm. This cut removed over 40% of the $\tau$ decay of the charged Kaon events. MC events were analyzed as a function of $x_{calorimeter}$ to study the sensitivity of the HMC estimate to this cut. Figure 4.40 shows the difference between HMC estimates and the input values for the slope $g$ as function of the $x_{calorimeter}$ cut. The HMC estimate is fairly insensitive to the variation of this cut. To be quantitative, it was determined from MC that the resolution of the X position at the upstream surface of the calorimeter is 0.14 cm. Varying the $x_{calorimeter}$ cut by this value changes the HMC estimate on $g$ by $(0.5 \pm 1.9) \times 10^{-3}$. This is consistent with zero within the statistical error.

### 4.5.3 Interaction

The difference in interactions between the $\pi^+$ and $\pi^-$ from charged Kaons decays with the material in the spectrometer should be minimal because of isopin invariance in strong

interaction which dictates that the $\pi^+p$ and $\pi^-n$ cross-sections as well as $\pi^+n$ and $\pi^-p$ cross-sections should be the same. Furthermore, most of the materials in the spectrometer contained approximately the same number of protons and neutrons.

However, in order to estimate the sensitivity of the asymmetry to the difference in interactions, we assumed the extreme case that the inelastic cross-sections of the $\pi^+p$ and $\pi^-p$ collisions are given by [37]

$$\sigma_{\pi^+p} = 24.3 - 12.3\ p_{lab}^{-1.91} + 0.324\ log^2 p_{lab} - 2.44\ log\ p_{lab}, \quad (4.20)$$

$$\sigma_{\pi^-p} = 26.6 - 7.18\ p_{lab}^{-1.86} + 0.327\ log^2 p_{lab} - 2.81\ log\ p_{lab}, \quad (4.21)$$

where $p_{lab}$ is the momentum of the pion in the laboratory. Assuming 22 mb as the average $\pi p$ inelastic cross-section, it was calculated that the probability of a $\pi^+$ interacting with material in the spectrometer between the exit window of the decay pipe and C7 inclusively was approximately $\mathcal{P}_I = 0.0116$. Using Equations 4.20 and 4.21, the probabilities of charged pions interacting in the spectrometer, $\mathcal{P}_I^{\pi^\pm}$, were then estimated as

$$\mathcal{P}_I^{\pi^\pm}(p_{lab}) = \frac{\sigma_{\pi^\pm p}}{22}\mathcal{P}_I. \quad (4.22)$$

Also, we assumed that the event was not reconstructible if any of the charged pions from $\tau$ decay of charged Kaon interacted in the spectrometer. Simulating interactions with MC for the decays of $K^+$ and $K^-$, the difference in the HMC estimates on $g$ is found to be $(0.2 \pm 1.9) \times 10^{-3}$. This is consistent with zero within the MC statistical error.

### 4.5.4 Efficiency of Hodoscope

As described in Section 3.3, the efficiency of each counter in the OS and SS hodoscopes was calculated on a run-by-run basis. We can simulate the response of the trigger hodoscopes using these calculated efficiencies. Figure 4.41 shows the difference between the HMC estimates and the input generated values for the slope $g$ for a subset of runs distributed throughout the data-collection period of the experiment.

In order to estimate the sensitivity of the asymmetry to the difference in the response of the trigger hodoscopes, we calculated the weighted averages of the efficiencies for all counters based on the run-by-run efficiencies as summarized in Table 4.1 and 4.2. Using the these efficiencies to simulate the response of the trigger hodoscopes for positive and negative runs separately, the HMC estimates on $g$ differ by $(1.3 \pm 1.9) \times 10^{-3}$. This is consistent with zero within the MC statistical error.

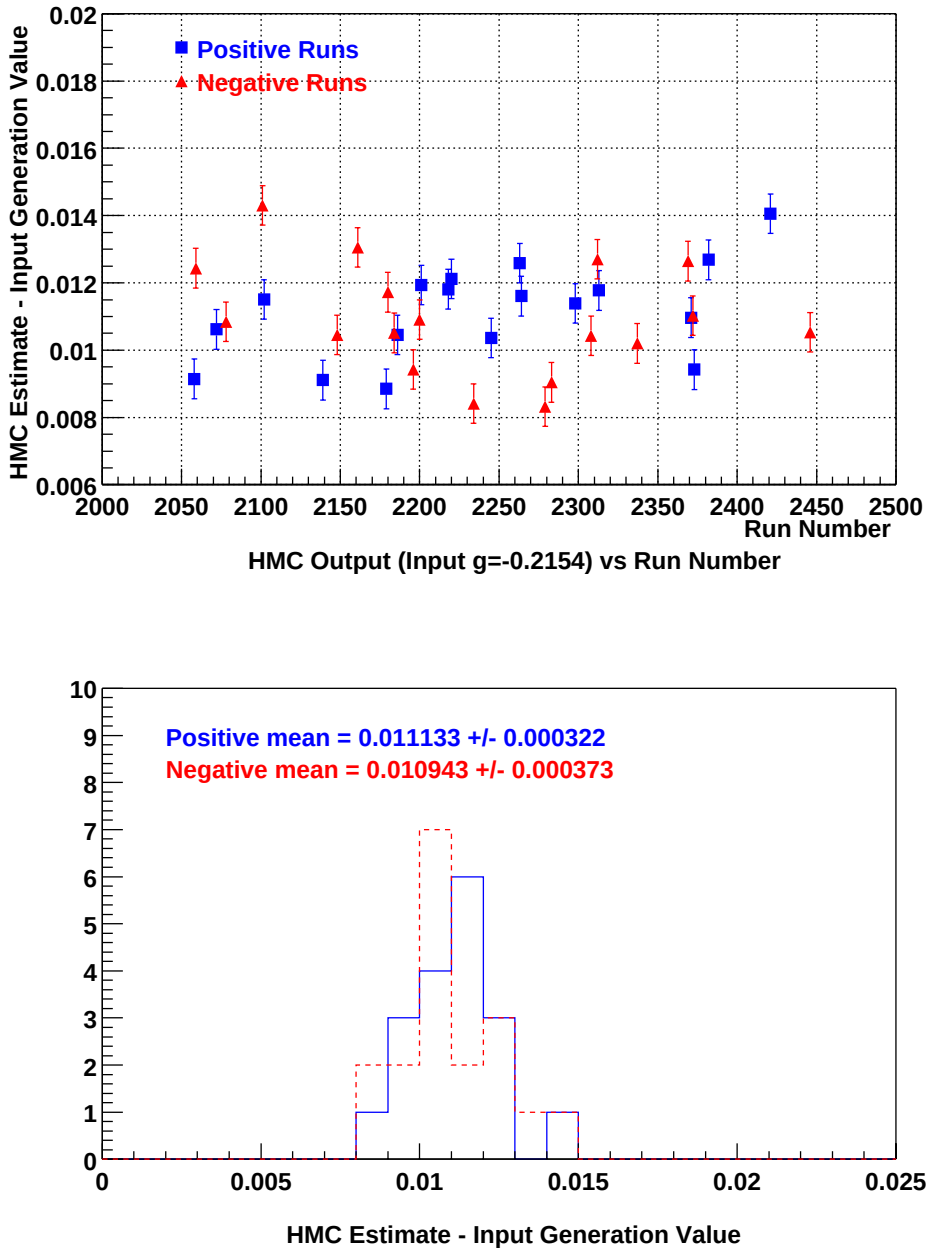


Figure 4.41: Difference between HMC estimates and input g value. Input MC events were generated with the measured response of the trigger hodoscopes. The top plot shows the difference between the HMC estimates and the input g value as a function of run. The bottom plot is a distribution of the difference for the postive (line) and negative (dash) runs with the numbers indicating the mean of the distribution.

| OS Counter | OS Efficiency (+) | OS Efficiency (-) |
|---|---|---|
| OS1 | 1.0000 ± 0.0000 | 1.0000 ± 0.0000 |
| OS2 | 0.6195 ± 0.1331 | 1.0000 ± 0.0000 |
| OS3 | 0.9641 ± 0.0049 | 0.9437 ± 0.0141 |
| OS4 | 0.9926 ± 0.0006 | 0.9912 ± 0.0013 |
| OS5 | 0.9943 ± 0.0003 | 0.9939 ± 0.0006 |
| OS6 | 0.9943 ± 0.0002 | 0.9947 ± 0.0004 |
| OS7 | 0.9950 ± 0.0002 | 0.9944 ± 0.0004 |
| OS8 | 0.9962 ± 0.0002 | 0.9956 ± 0.0004 |
| OS9 | 0.9941 ± 0.0004 | 0.9917 ± 0.0009 |
| OS10 | 0.9184 ± 0.0060 | 0.8544 ± 0.0162 |
| OS11 | 0.6436 ± 0.0192 | 0.7545 ± 0.0377 |
| OS12 | 0.6137 ± 0.0228 | 0.7096 ± 0.0490 |
| OS13 | 0.6483 ± 0.0322 | 0.7370 ± 0.0664 |
| OS14 | 0.5719 ± 0.0425 | 0.7061 ± 0.0851 |
| OS15 | 0.5931 ± 0.0403 | 0.6211 ± 0.0919 |
| OS16 | 0.5195 ± 0.0968 | 0.6047 ± 0.1525 |

Table 4.1: Efficiency of OS counter for positive and negative data. Only OS2 to OS9 were used in the K trigger.

### 4.5.5 Efficiency of Wire Chamber

Similar to the hodoscope efficiency, the wire-by-wire efficiency of the wire chamber was calculated run-by-run as described in Section 3.3. MC events were generated with this wire efficiency incorporated, then were reconstructed and analyzed. Figure 4.42 shows the difference between the HMC estimates and the input value for the slope $g$ for a subset of runs.

Similar to the hodoscope efficiency, the weighted averages of the wire efficiencies were calculated from the run-by-run wire efficiency. MC events were then generated with the weighted average wire efficiency for the positive and negative data separately. After reconstruction and event selection, the HMC estimates on $g$ are found to differ by $(0.7 \pm 1.9) \times 10^{-3}$.

### 4.5.6 Targeting

It can be seen in Figures 4.3 and 4.4 that targeting could move as much as 0.5 mm from the nominal targeting in both transverse directions. To study the effect on the asymmetry due to a difference in transverse targeting, MC events were generated with different X

| SS Counter | SS Efficiency (+) | SS Efficiency (-) |
|---|---|---|
| SS1 | 0.9833 ± 0.0001 | 0.9845 ± 0.0001 |
| SS2 | 0.9964 ± 0.0000 | 0.9965 ± 0.0000 |
| SS3 | 0.9951 ± 0.0000 | 0.9953 ± 0.0000 |
| SS4 | 0.9960 ± 0.0000 | 0.9961 ± 0.0000 |
| SS5 | 0.9955 ± 0.0000 | 0.9955 ± 0.0001 |
| SS6 | 0.9955 ± 0.0000 | 0.9956 ± 0.0001 |
| SS7 | 0.9952 ± 0.0000 | 0.9955 ± 0.0001 |
| SS8 | 0.9950 ± 0.0000 | 0.9953 ± 0.0001 |
| SS9 | 0.9948 ± 0.0001 | 0.9949 ± 0.0001 |
| SS10 | 0.9946 ± 0.0001 | 0.9952 ± 0.0001 |
| SS11 | 0.9943 ± 0.0001 | 0.9946 ± 0.0002 |
| SS12 | 0.9936 ± 0.0001 | 0.9946 ± 0.0002 |
| SS13 | 0.9932 ± 0.0002 | 0.9941 ± 0.0004 |
| SS14 | 0.9919 ± 0.0004 | 0.9913 ± 0.0007 |
| SS15 | 0.9891 ± 0.0007 | 0.9859 ± 0.0015 |
| SS16 | 0.9710 ± 0.0023 | 0.9772 ± 0.0036 |
| SS17 | 0.8848 ± 0.0101 | 0.8957 ± 0.0173 |
| SS18 | 0.4862 ± 0.0359 | 0.4905 ± 0.0600 |
| SS19 | 0.3190 ± 0.0680 | 0.3900 ± 0.0954 |
| SS20 | 1.0000 ± 0.0000 | 0.3953 ± 0.2157 |
| SS21 | 0.5000 ± 0.3536 | 1.0000 ± 0.0000 |
| SS22 | 0.3333 ± 0.1925 | 1.0000 ± 0.0000 |
| SS23 | 1.0000 ± 0.0000 | 1.0000 ± 0.0000 |
| SS24 | 1.0000 ± 0.0000 | 1.0000 ± 0.0000 |

Table 4.2: Efficiency of SS counter for positive and negative data. Only SS2 to SS18 were used in the K trigger.

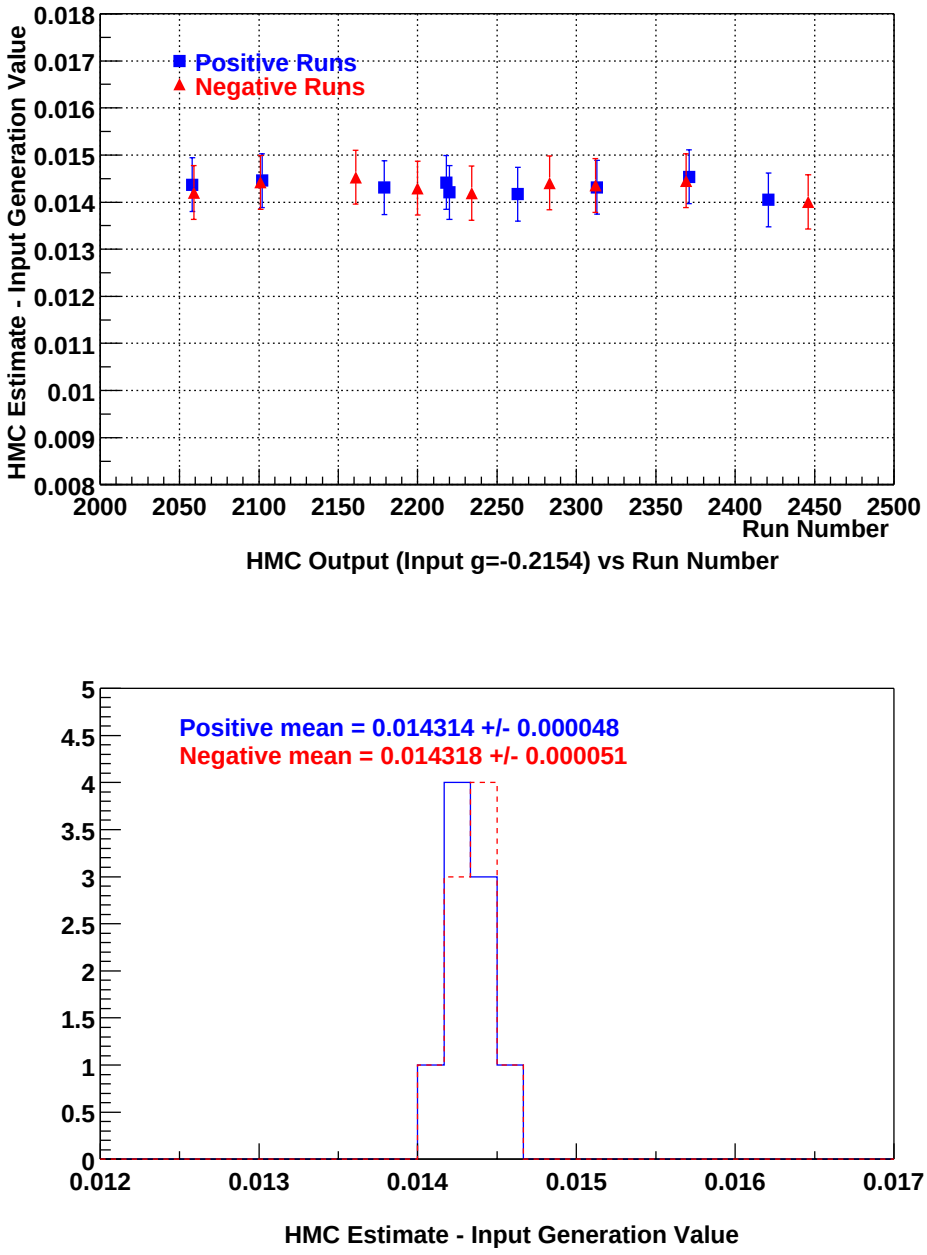


Figure 4.42: Difference between HMC estimates and input $g$ value. Input MC events were generated with the wire-by-wire efficiency incorporated. The top plot shows the difference between the HMC estimates and the input $g$ value as a function of run. The bottom plot is a distribution of the difference for the postive (line) and negative (dash) runs with the means of the distributions shown.

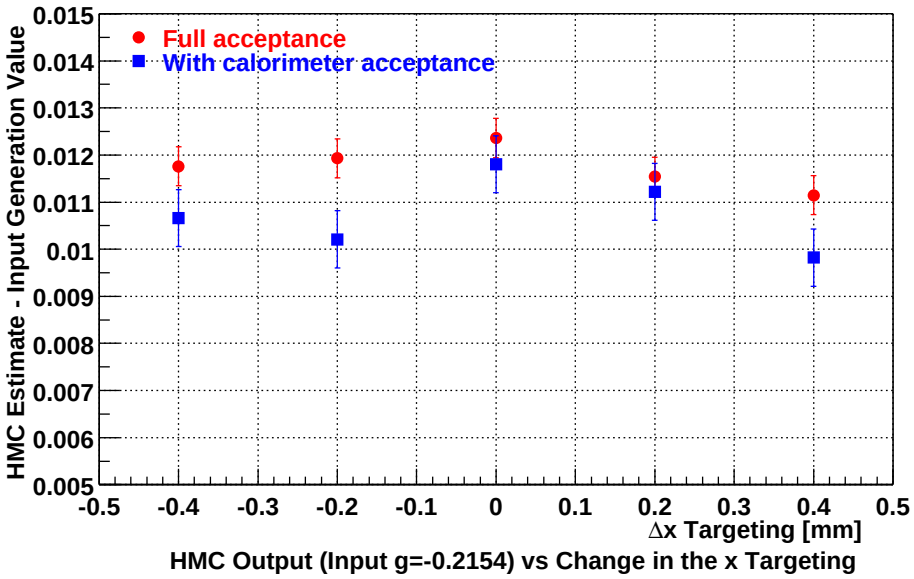


Figure 4.43: Difference between HMC estimates and input $g$ value as a function of X position at the target.

and Y nominal positions at the target. Figures 4.43 and 4.44 show the difference between the HMC estimates and the input $g$ value as a function of different X and Y targeting respectively. The distributions indicate, within the statistical error, that the asymmetry is fairly insensitive to the transverse targeting.

On the average, the transverse targeting of the positive data differed from the negative data by -32.0 $\mu$m in the X direction and -51.0 $\mu$m in the Y direction. MC events with these shifts in the transverse targeting lead to a difference in the HMC estimates on $g$ by $(0.5 \pm 1.9) \times 10^{-3}$ for the shift in X targeting and by $(1.0 \pm 1.9) \times 10^{-3}$ for the shift in Y targeting.

### 4.5.7 Magnetic Field

There were two sources of potential systematic effect coming from a difference in magnetic field between the positive and negative runs in the spectrometer. One was the effect of the earth's magnetic field and the other was the precision of the Hall probes from which we measured the field of the analysis magnet. We assumed that both effects would produce

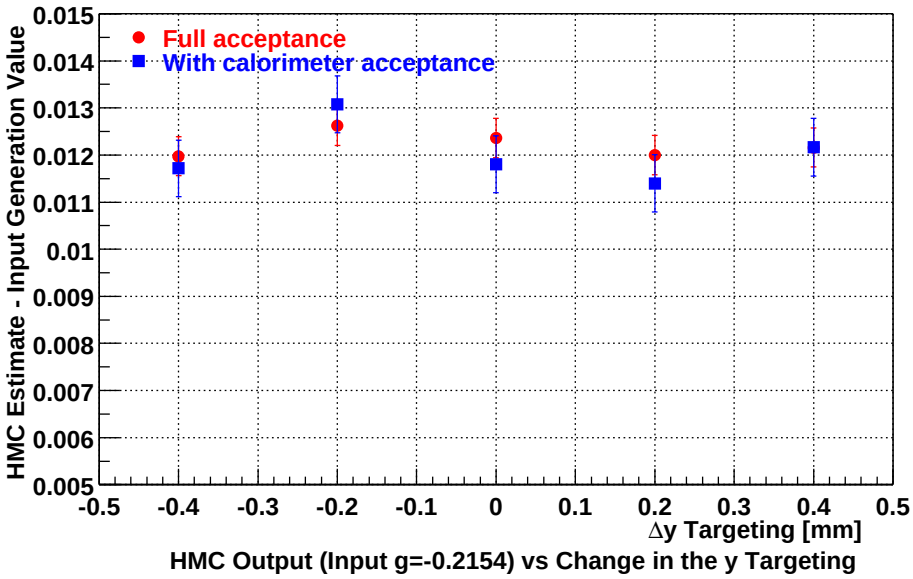


Figure 4.44: Difference between HMC estimates and input $g$ value as a function of Y position at the target.

a difference in the momentum kick as the particle transversed through the spectrometer.

The earth's magnetic field, $B_{earth}$, at Fermilab is about 0.6 G and is inclined at a dip angle $\theta_{earth} \approx 60^{\circ}$. A simple estimation of the difference in kick between the positive and negative data is given by

$$\Delta p_{kick}^{Earth} = 2 \times 0.3 \; B_{earth} L \; sin \; \theta_{earth}, \tag{4.23}$$

where $L = 16$ m is the effective length of the earth's field and was approximately the distance between wire chamber C1 and wire chamber C8 less the length of the analysis magnet (the earth's field was shielded in the analysis magnet). The factor of two accounts for the fact that positive and negative tracks bend in opposite direction. This gives $\Delta p_{kick}^{Earth} = 5.2 \times 10^{-4}$ GeV/c. On the other hand, from the specification of the Hall probes, the uncertainty in the kick due to the precision of the Hall probes was estimated to be $\Delta p_{kick}^{Hall} = 2 \times 10^{-4}$ GeV/c. This value is consistent with the asymmetry seen in the reconstructed Kaon mass from the same polarity.

To study the systematic effect due to the difference in magnetic field, we generated MC events with the average field of the analysis magnet but reconstructed and analyzed with a

| Source of Systematic | $\frac{\Delta g}{2g_{PDG}}$ Error $(\times 10^{-3})$ |
|---|---|
| Secondary Beam | 1.6 |
| Calorimeter Fiducial | 0.5 |
| Interaction | 0.2 |
| Hodoscope Efficiency | 1.3 |
| Wire Efficiency | 0.7 |
| Targeting | $0.5 \pm 1.0$ |
| Magnetic Field | $1.7 \pm 1.0$ |
| MC statistics | 1.9 |
| Total | 3.7 |

Table 4.3: Systematic error on the asymmetry $\Delta g/2g_{PDG}$.

different field representing the difference in kick. The change in $g$ is $(1.7 \pm 1.9) \times 10^{-3}$ for the effect of the earth's magnetic field and $(1.0 \pm 1.9) \times 10^{-3}$ for the effect of the precision of the Hall probes.

## 4.6 Summary and Discussion of the Systematic Errors

Table 4.3 summarizes the estimated systematic errors on the asymmetry $\Delta g/2g_{PDG}$ studied in this analysis. All of the numbers are not small compared to the sensitivity of the measurement. However, statistically, all of the numbers are consistent with zero. The studies are limited by the number of MC events. Adding all contributions in quadrature, the total systematic error on the asymmetry $\Delta g/2g_{PDG}$ is $3.7 \times 10^{-3}$. It is not clear that the measurement would be dominated by systematic effect. Even so, most of systematic effect could be corrected. Unfortunately, due to lack of time and resources, generating more MC events was not practical at this moment. In addition, a better simulation of the systematic effects might be required to accurately estimate the systematic error. Much time and effort are needed for another iteration on the estimation of the systematic error and perform possible corrections.

# Chapter 5

# Results and Conclusions

In the previous chapter, the Hybrid Monte Carlo method is presented as a method to extract the coefficients of the expansion describing the Dalitz plot. However, the acceptance of the HMC events was not properly simulated, in particular event reconstruction was not included and this omission led to biases in the HMC estimates of the coefficients. Since correcting the biases is computing intensive and would require detailed understanding of the spectrometer which is still in progress, the approach of understanding the sensitivity of the biases to known differences between the positive and negative data is taken. This is documented in the previous chapter. When the difference in the coefficients between the positive and negative data is calculated, the biases are removed leaving the remaining asymmetry due to physics.

## 5.1 Determining Linear Slope $g$ and CP Asymmetry

The slope $g$ for each run was estimated using the HMC method. Figure 5.1 shows the $g$ values as a function of run for the positive and negative data sets. There is a slight dependence of the estimated $g$ values on run number. This temporal shift could be due to a number of effects which were not simulated in the HMC method. There could be time variation in the wire chamber alignment. In addition, temporal shifts in targeting caused the charged Kaon beam to move, leading to a different acceptance due to the odd pion at the fiducial of the calorimeter. In any case, the same trend appears in both the positive and negative runs and would cancel when we calculate the asymmetry. Apart from the slight dependence with time, the fluctuation of the measured values are essentially statistical as

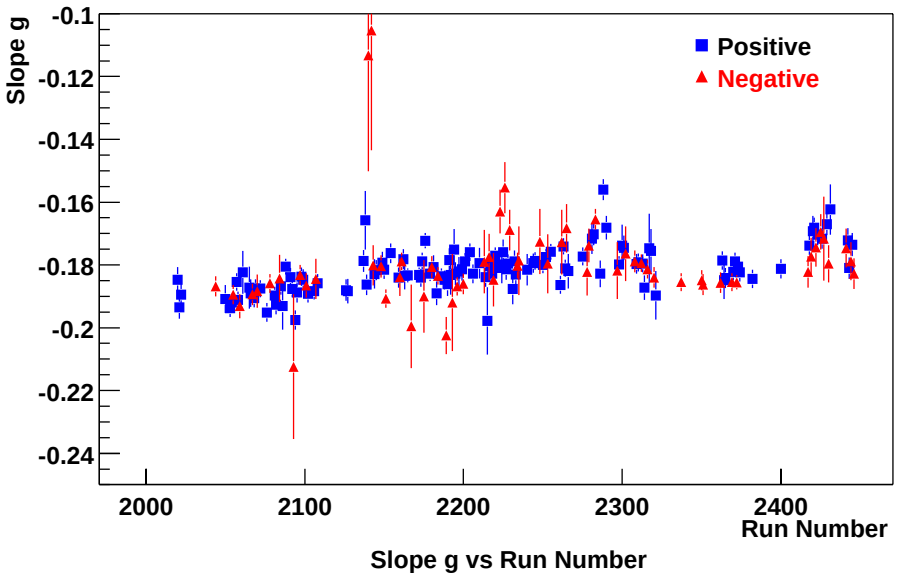


Figure 5.1: Measured $g$ as a function of run.

shown in Figures 5.2 and 5.3. The values are normally distributed. More importantly, there does not seem to have any systematic shift between the positive and negative distributions implying that there is no observed asymmetry in the linear slope $g$.

In order to get a single value for $g$, the data from all the runs for a single polarity were processed together with the HMC program. The results are

$$g_+ = -0.18091 \pm 0.00030, \tag{5.1}$$

$$g_- = -0.18187 \pm 0.00055. \tag{5.2}$$

Thus, the resulting asymmetry is

$$\Delta g/2g_{PDG} = (2.2 \pm 1.5) \times 10^{-3}. \tag{5.3}$$

The dependence of the answer to the event selection cuts was studied by varying the cuts as listed in Table 3.3 and re-analyzing the data. The description of the variations in the cuts are listed in Table 5.1. The asymmetries $\Delta g/2g_{PDG}$ are presented in Figure 5.4. Statistically, the answers are consistent among themselves and we assign no systematic error to the effect of variation in the cuts.

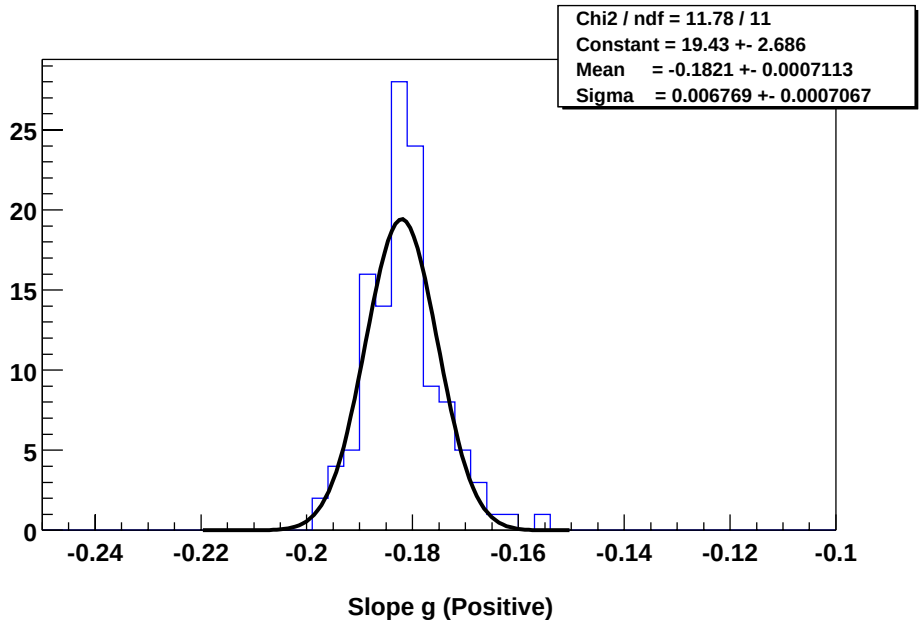


Figure 5.2: Distribution of measured $g$ for positive runs.

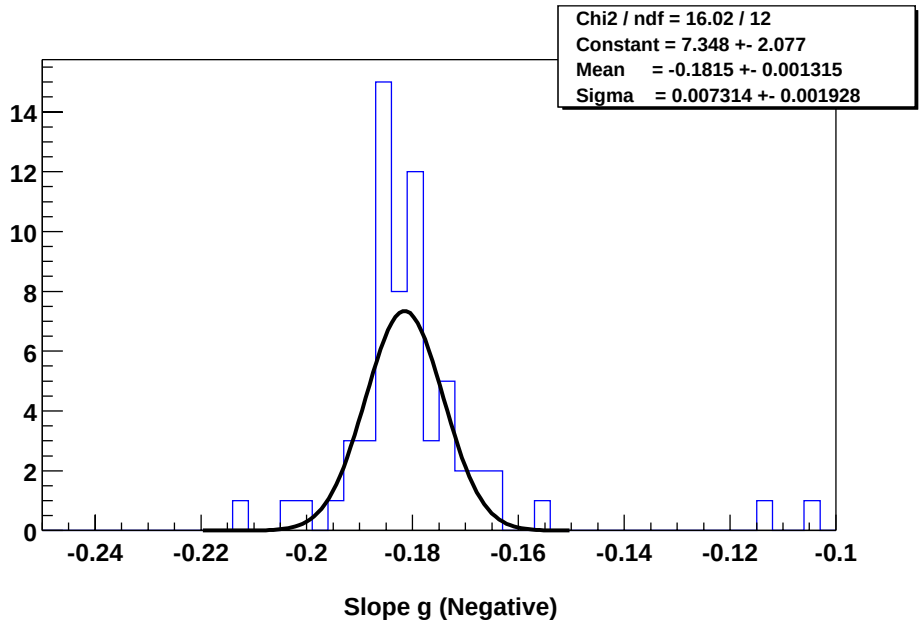


Figure 5.3: Distribution of measured $g$ for negative runs.

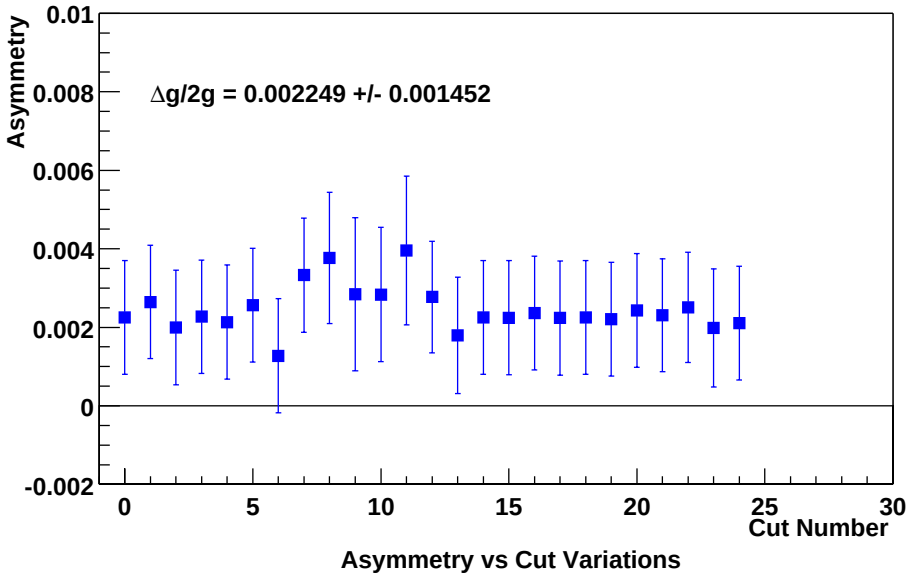


Figure 5.4: Asymmetry $\Delta g/2g_{PDG}$ as a function of variation of cut. The description of each cut number is listed in Table 5.1.

| Cuts | Descriptions |
|---|---|
| 0 | Nominal cut |
| 1-2 | Vary $m_{\Lambda\pi}$ cut by $\pm 1$ standard deviation. |
| 3 | Accept events with more than one Kaon candidates. |
| 4-5 | Vary $\chi^2_{DF}$ cut by $+0.3$ and $-0.2$. |
| 5-6 | Vary $m_{3\pi}$ cut by $\pm 1$ standard deviation. |
| 8-11 | Tighten collimator exit cut to avoid the edges. |
| 12-13 | Vary decay vertex Z cut by $\pm 25$ cm. |
| 14-15 | Vary Kaon momentum cut by $\pm 1$ GeV/c. |
| 16-19 | Vary target pointing cut by $\pm 0.02$ mm. |
| 20 | Remove gamma conversion cut. |
| 21 | Loosen $m_\Omega$ cut by $\pm 1$ MeV/c$^2$. |
| 22-23 | Vary calorimeter fiducial cut by $\pm 2$ cm. |
| 24 | Remove K trigger cut. |

Table 5.1: Variation of cuts.

## 5.2 Conclusions

We have studied the asymmetry of the linear slope parameter, $\Delta g/2g_{PDG}$, of the Dalitz plot of $K^{\pm} \to \pi^{\pm}\pi^{\pm}\pi^{\mp}$ decays. Based on 41.8 million $K^+$ and 12.4 million $K^-$ events, we obtained a result

$$\frac{\Delta g}{2g_{PDG}} = [2.2 \pm 1.5(stat) \pm 3.7(syst)] \times 10^{-3} \tag{5.4}$$

which is consistent with no observed CP asymmetry between the $\tau^+$ decay and $\tau^-$ decay of charged Kaon. Our measurement agrees with the previous determination of $(g_{\tau^+} - g_{\tau^-})/(g_{\tau^+} + g_{\tau^-}) = (-7.0 \pm 5.3) \times 10^{-3}$ [29], though with a better statistical uncertainty.

The current study is dominated by the systematic uncertainty which could be significantly reduced by performing better simulation of the systematic effects and generating more MC events. In addition, we could try to correct for the HMC bias by correctly simulating the acceptance of the HMC events. Another iteration on the systematic studies would be required.

# Appendix A

# Track-Finding Algorithm

In this appendix, the track-finding algorithm is described. Positions of charged particle tracks transversing the spectrometer were measured by eight MWPCs, four upstream and four downstream of the analysis magnet, at different Z locations. In each MWPC, there were four wire planes resulting in up to thirty-two discrete measurements or hits for each track. The task of the track-finding algorithm is to reconstruct all tracks transversing the spectrometer from the recorded MWPC hits.

## A.1 Chamber Orientation

The views of the four wire planes are labelled as X, U, V, and X'. In principle, the orientation of each wire plane can be defined by three Euler angles. However, the wire planes inside a MWPC are parallel and separated from the adjacent planes by 6 mm. So, the four views in a given MWPC share two of the angles defined by the orientation of the MWPC. The third angles is defined by the direction of the wires.

The coordinate as measured by each wire plane is done in the local coordinate system The local coordinate system $(x_c, y_c, z_c)$ is defined by having the $x_c$ axis perpendicular to the the wire direction (this axis measures the coordinate of the view), the $z_c$ axis perpendicular to the wire plane pointing downstream, and the $y_c$ axis completing the right-handed coordinate system. The local coordinate system can be related to the laboratory coordinate

system:

$$\begin{pmatrix} x_c \\ y_c \\ 0 \end{pmatrix} = [M] \begin{pmatrix} x \\ y \\ z - z_0 \end{pmatrix}, \tag{A.1}$$

where $[M]$ is a $3 \times 3$ transformation matrix and $z_0$ is the z position of the wire plane at $(x, y) = (0, 0)$. $z_c$ is set to zero because the origin of the local coordinate system is taken to be on the wire plane and at $(x, y) = (0, 0)$. In addition, $z_0$ is subtracted from the $z$ coordinate because the transformation matrix can be simplified if both coodinate systems share a common origin.

The matrix $[M]$ is a product of three rotation matrices:

$$[M] = R_z(\theta_z) R_y(\theta_y) R_x(\theta_x), \tag{A.2}$$

where

$$R_z(\theta_s) = \begin{pmatrix} cos\ \theta_z & sin\ \theta_z & 0 \\ -sin\ \theta_z & cos\ \theta_z & 0 \\ 0 & 0 & 1 \end{pmatrix}, \tag{A.3}$$

$$R_y(\theta_y) = \begin{pmatrix} cos\ \theta_y & 0 & -sin\ \theta_y \\ 0 & 1 & 0 \\ sin\ \theta_y & 0 & cos\ \theta_y \end{pmatrix}, \tag{A.4}$$

$$R_x(\theta_x) = \begin{pmatrix} 1 & 0 & 0 \\ 0 & cos\ \theta_x & sin\ \theta_x \\ 0 & -sin\ \theta_x & cos\ \theta_x \end{pmatrix}. \tag{A.5}$$

$R_x$ corresponds to rotating the laboratory coordinate system $(x, y, z)$ about the x-axis by an angle $\theta_x$ to the coordinate system $(x_1, y_1, z_1)$. $R_y$ represents rotation of the cooordinate system $(x_1, y_1, z_1)$ about the $y_1$ axis by an angle $\theta_y$ to the coordinate system $(x_2, y_2, z_2)$. Finally, $R_z$ rotates the cooordinate system $(x_2, y_2, z_2)$ about the $z_2$ axis by an angle $\theta_z$ to the local coordinate system $(x_c, y_c, z_c)$.

Defining $s_x = sin\ \theta_x, c_x = cos\ \theta_x, s_y = sin\ \theta_y, c_y = cos\ \theta_y, s_z = sin\ \theta_z$ and $c_z = cos\ \theta_z$, the rotation matrix $[M]$ is given by

$$M = \begin{pmatrix} M_{11} & M_{12} & M_{13} \\ M_{21} & M_{22} & M_{23} \\ M_{31} & M_{32} & M_{33} \end{pmatrix}$$

$$= \begin{pmatrix} c_y c_z & s_x s_y c_z + c_x s_z & -c_x s_y c_z + s_x s_z \\ -c_y s_z & -s_x s_y s_z + c_x c_z & c_x s_y s_z + s_x c_z \\ s_y & -s_x c_y & c_x c_y \end{pmatrix}, \tag{A.6}$$

where $\theta_x$ and $\theta_y$ are defined by the orientation of the MWPC and are common to all four views in the MWPC, $\theta_z$ is the stereo angle of the wire plane and defines the wire direction. The wire coordinate is given by $x_c$:

$$x_c = M_{11}x + M_{12}y + M_{13}(z - z_0). \tag{A.7}$$

## A.2 Clustering of Hits

Clustering of hits is the process of combining adjacent hits on a wire plane to form a single hit. Clustering is needed because sometimes more than one hit are produced by a charged particle transversing a wire plane. In the experiment, downstream tracks are fairly separated and are unlikely to produce hits that are adjacent to each other on a wire plane. On the other hand, this is not the case for the upstream tracks. Hence, downstream hits are clustered and upstream hits are not. The maximum number of hits in a single cluster is optimized to be three and the clustering is done in ascending wire coordinates. The centroid of the clustered hit is taken to be the mean of the individual hits and its error is given by $(\textit{number of hits in the cluster} \times \textit{pitch of the wire plane})/\sqrt{12}$.

## A.3 Reconstruction of Space-points

As a charged particle transverses a MWPC, hits will be produced in each of the wire plane with high efficiency. By combining the hits from the four wire planes within a MWPC, space-points ($x$ and $y$ coordinates) at where the track crosses a MWPC can be reconstructed. In principle, only two views with differecnt orientation are needed to reconstruct space-points. But in this case, ambiguities will arise in reconstructing space-points if more than one track crosses a MWPC at the same time. Hence, the MWPC in the experiment are constructed with four views to help resolve ambiguities and also provide redundancy in reconstructing space-points.

To a good approximation, $\theta_x$ and $\theta_y$ are small and can be ignored when constructing space-points. Thus, a wire plane within a MWPC is uniquely difined by its stereo angle $\theta_z$

and the wire coordinate is approximately given by

$$x_c = cos(\theta_z)\ x + sin(\theta_z)\ y. \tag{A.8}$$

At least three different views are required to form a space-point. The following steps are taken in associating the hits to a space-point:

1. Since X and X' views have wires parallel to each other but offset by half a pitch from each other, their hits can be matched to space-points if the difference between their wire coordinates is within some fixed tolerance.

2. Each MWPC is constructed such that $|(\theta_z)_U| = -|(\theta_z)_V|$. Hence, a checksum criterion can be used to associate the U and the V hits to the X and/or X' hits:

$$|u + v - 2x\ cos(|(\theta_z)_U|)| < checksum_{tolerance}, \tag{A.9}$$

   where $u$, $v$, and $x$ are the U, V and X/X' coordinates of the hits respectively. If X and X' wire coordinates match, then $x$ is taken as their mean. These space-point candidates have one of the hit combinations: (X, X', U, V), (X, U, V) and (X', U, V). This set of space-points is denoted as seed space-points that are used as initial points in reconstructing tracks. The checksum criterion assumes that the gap between the wire planes within a MWPC is negligible. This assumption can cause some inefficiency in constructing space-points for tracks transversing the MWPC with a large angle relative to the normal of the wire planes.

3. The remaining unmatched hits are used to form space-points with the following hit combinations: (X, X', U) and (X, X', V). This set of space-points are not used as seed space-points because they contain more ghost space-points. They are used to match to the track candidate.

Assuming that the gap between the wire planes within a MWPC is negligible and using Equation A.8, the $(x, y)$ coordinates of the space-points candidates are determined by minimizing the following $\chi^2$ function:

$$\chi^2 = \sum_i \frac{[cos(\theta_z)_i\ x + sin(\theta_z)_i\ y - m_i]^2}{\sigma_i^2}, \tag{A.10}$$

where $m_i$ is the wire coordinate of the hit for wire plane $i$ that is associated to the space-point candidate and $\sigma_i$ is the error of the wire coordinate. A cut is made on the value of the $\chi^2$ to filter out poor quality space-points.

Using Equations A.1, A.6 and the reconstructed $(x, y)$ coordinates of the space-point, the z coordinate of the wire plane associated to the space-point is given by

$$z = -\frac{M_{31}x + M_{32}y}{M_{33}} + z_0. \tag{A.11}$$

## A.4 Reconstruction of Upstream and Downstream Tracks

The MWPCs in the spectrometer are divided into two sets: upstream and downstream. Track candidates are reconstructed separately using upstream and downstream MWPCs. These track candidates are labeled upstream tracks and downstream tracks.

For each set of MWPCs, the MWPCs are labeled as 1, 2, 3 and 4 in ascending Z positions. The following steps are made in finding the upstream and downstream track candidates:

1. At least two space-points are needed to define a track segment. In order to have sufficient efficiency in finding track candidates, three combinations of two seed space-points from different MWPCs are used to define the track candidate. The three seed combinations are (1,4), (1,3) and (2,4) where the numbers in the parantheses are the MWPC labels. Each track candidate defined by the two seed space-points is projected to the other MWPC to search for space-points that are associated to the track candidate. A road is defined around the track candidate to look for the associated space-points. Each track candidate is required to contain at least three space-points.

2. In some cases, due to inefficiency, tracks transversing the spectrometer can produce space-points with hit combinations of the type (X, X', U) and (X, X', V) in adjacent MWPCs. These tracks would not be reconstructed using the three seed combinations described in Step 1. Hence, another three seed combinations are used to find this type of tracks: (1,2), (2,3) and (3,4). Again, the track candidate is projected to the other MWPC that are not part of the seed chambers to search for associated space-points. In order to find track candidate that has not been found in the previous step, only space-points with hit combinations of the type (X, X', U) and (X, X', V) are looked for.

3. A three-dimensional track is uniquely defined by the slope and intercept of a line in two orthogonal projections: (X,Z) plane and (Y,Z) plane. They have the following

linear relationship:

$$x = a_x z_i + b_x, \tag{A.12}$$

$$y = a_y z_i + b_y, \tag{A.13}$$

where $a_x$ and $a_y$ are the slopes, $b_x$ and $b_y$ are the intercepts, and $z_i$ is the Z positions of the wire plane measured from the bend plane of the spectrometer. The definition of the bend plane will be described in Section A.5.1. In brief, the Z position of the bend plane is the mean Z position where the upstream and downstream tracks intersect in the analysis magnet. This translation of the $z = 0$ position to the bend plane is made so that the upstream and downstream tracks are reconstructed with approximately equal moment arm. Substituting Equation A.12 and A.13 into Equation A.7, the calculated wire coordinate is given by

$$(x_c)_i = M_{11}[a_x z_i + b_x] + M_{12}[a_y z_i + b_y] + M_{13}(z_i - (z_0)_i), \tag{A.14}$$

where the subscript $i$ refers to the wire plane $i$ and $z_i$ is given by Equation A.11. Thus, the parameters are determined by minimizing the following $\chi^2$ function:

$$\chi^2 = \sum_i \frac{((x_c)_i - m_i)^2}{\sigma_i^2}, \tag{A.15}$$

where $m_i$ is the wire coordinate of the hit from wire plane $i$ that is associated to the track candidate. From Equation A.11, $z_i$ clearly depends on the track parameters. Equation A.15 will then involve non-linear terms. Therefore, an iterative method would be necessary to minimize the $\chi^2$. However, to a good approximation, $z_i$ can be assumed constant because the intersection of the track with the wire plane is not expected to change much from the fit. With this assumption, the problem becomes linear and minimizing the $\chi^2$ can be solved analytically. A cut is made on the value of the $\chi^2$ to weed out poorly reconstructed tracks and fake tracks.

4. A charged particle that produces less than three hits as it tranverses a MWPC would not have its space-points reconstructed. Therefore, track candidates with only three space-points are projected to the wire planes of the MWPC that has no space-points to search for hits which can be associated with the track candidate. If extra hits are found, the track candidate is refitted with the extra hits included.

5. Some of the track candidates found are essentially the same track because of the number of seed combinations used. Also, in some cases, tracks that are closed to each other will produce some unwanted track candidates resulting from the combinatorial of the space-points. Therefore, a metric is needed to group similar tracks together. One such metric is defined by forming a $\chi^2$ function to compare any two tracks:

$$\begin{aligned} \chi^2 &= (\mathbf{v}_1 - \alpha)^T V_1 (\mathbf{v}_1 - \alpha) + \\ & \quad (\mathbf{v}_2 - \alpha)^T V_2 (\mathbf{v}_2 - \alpha), \end{aligned} \tag{A.16}$$

where the components of the vector $\mathbf{v_1}$ and $\mathbf{v_2}$ correspond to the X-slope, X-intercept, Y-slope and Y-intercept (i.e., $\mathbf{v_1}^T = (a_{x1}, b_{x1}, a_{y1}, b_{y1})$) of track one and track two respectively. $V_1$ and $V_2$ are the covariance matrix of track one and track two respectively. To simplify the $\chi^2$ expression in Equation A.16, the covariance matrix are modified such that the terms relating the parameters of the X projection of the track to the parameters of the Y projection of the track are set to zero. In other words, the correlation between the X projection and Y projection of the track is assumed negligible which is a valid approximation. The vector $\alpha$ is an estimate of the mean of the two track parameters. Minimizing Equation A.16 gives a minimum $\chi^2$, $\chi^2_{min}$, that can be used as a metric for grouping similar tracks. For a given group of similar tracks, the track with the smallest $\chi^2$ defined in Equation A.15 is selected as the track candidate of the group.

Most of the upstream tracks are fairly closed together. However, downstream tracks are fairly well separated after passing the analysis magnet and they are less ambiguous and easier to reconstruct. Therefore, in order to have high efficiency of reconstructing closed upstream tracks, cuts used in finding upstream track candidates are more relaxed than the same cuts used in finding downstream track candidates. The drawback is that upstream track candidates contain more ghost tracks. These ghost tracks are filter out by matching the downstream track candidates to the upstream track candidates which is described in the next section.

## A.5 Complete Reconstruction of Track

### A.5.1 Single-Bend-Plane Approximation

A complete track candidate is reconstructed by matching the downstream track candidates with the upstream track candidates. In principle, the upstream track candidates can be propagated through the analysis magnet using the field map of the magnet to match to the downstream track candidate. But this can be a computing intensive process. In addition, the magnetic field map is not very well understood yet. However, the major component of the field is a dipole field and is fairly constant in the central region of the magnet. Therefore, single-bend-plane approximation is applied to match the upstream and downstream track candidates. Assuming that the angle of the track entering a perfect dipole magnet and the total bend angle of the track after transversing the magnet are negligible, it can be shown that there exists a virtual plane inside the magnet where the upstream and downstream track intersect. This virtual plane is called the bend plane. In general, this bend plane depends on the angle of the upstream track and the bend angle. However, the polar angles of the upstream tracks in the experiment are fairly small resulting in a small variation in the location of the bend plane, small relative to the length of the magnet. Therefore, a mean position of the bend plane can be defined.

In the spectrometer, the two analysis magnets can be treated as a single magnet as they are placed relatively closed together. The magnets are aligned such that their dipole fields are perpendicular to the Z-axis. Hence, the bend plane is perpendicular to the Z-axis. The Z position of the mean bend plane is denoted as $z_{bendplane}$ and is determined from the distribution of the Z positions where the upstream and downstream tracks have the smallest distance of approach. The mean of this distribution is taken to be $z_{bendplane}$.

### A.5.2 Matching Upstream and Downstream Tracks

For each downstream track candidate, it is matched to an upstream track candidate to construct a complete track candidate using the following criteria:

1. Since the main component of the M2 field is along the Y direction, the tracks are bend in the (X,Z) plane. Thus, the difference in the Y slopes between the upstream and downstream track candidates has to be small. A $\chi^2_{slope}$ function is constructed to

express the quality of this difference:

$$\chi^2_{slope} = \frac{(a_{yu} - a_{yd})^2}{\sigma^2_{a_{yu}} + \sigma^2_{a_{yd}}}, \tag{A.17}$$

where $a_{yu}$ and $a_{yd}$ are the y slopes of the upstream and downstream track candidates respectively, $\sigma_{a_{yu}}$ and $\sigma_{a_{yd}}$ are their errors which are taken from the diagonal elements of the covariance matrix from track fitting.

2. The difference in the (X,Y) intercept at the Z location detemined with the distance of closest approach between the upstream and downstream track candidates has to be small. A $\chi^2_{incpt}$ function is constructed to express the quality of this difference:

$$\chi^2_{incpt} = \frac{(b_{cxu} - b_{cxd})^2}{\sigma^2_{b_{cxu}} + \sigma^2_{b_{cxd}}} + \frac{(b_{cyu} - b_{cyd})^2}{\sigma^2_{b_{cyu}} + \sigma^2_{b_{cyd}}}, \tag{A.18}$$

where $b_{cxu}$ and $b_{cxd}$ are the X intercepts of the upstream and downstream track candidates at the Z position of the distance of closest approach respectively, $\sigma_{b_{cxu}}$ and $\sigma_{b_{cxd}}$ are their errors which are taken from the diagonal elements of the covariance matrix from track fitting. Similarly, $b_{cyu}$ and $b_{cyd}$ are the Y intercepts of the upstream and downstream track candidates at the Z position determined by the distance of closest approach, and their errors are denoted as $\sigma_{b_{cyu}}$ and $\sigma_{b_{cyd}}$.

3. The Z position where the upstream and downstrem track candidates intersect $z_{intersect}$ (i.e, have the closest distance of approach) has to be within a fixed window $\Delta z_{tolerance}$ of the $z_{bendplane}$:

$$|z_{intersect} - z_{bendplane}| < \Delta z_{tolerance}. \tag{A.19}$$

### A.5.3 Global Fit of Tracks

A constraint fit can be applied to the complete track candidates to obtain a better estimate of the track parameters. The constraints are based on two assumptions: (1) the upstream and downstream track segments intersect at the mean bend plane; and (2) the analysis magnet has a dipole field along the Y direction resulting in the track receiving a $p_t$ kick in the X direction only. These constraints can be put in following equations:

$$b_{xu} = b_{xd}, \tag{A.20}$$

$$b_{yu} = b_{yd}, \tag{A.21}$$

$$a_{yu} = G a_{yd}, \tag{A.22}$$

where

$$G = \sqrt{\frac{1 + a_{xu}^2}{1 + a_{xd}^2}}. \tag{A.23}$$

The factor G arises from the fact that a track entering the analysis magnet will receive a $p_t$ kick in the X direction, thus changing the Z component of the track momentum $p_z$ in order to conserve the total momentum. Since the Y component of track momentum $p_y$ remains the same as the track transverses the analysis magnet, the Y slope of the track $p_y/p_z$ has to change according to Equation A.22.

Using Equation A.14, a $\chi^2$ function is constructed for each complete track:

$$\begin{aligned} \chi^2 &= \sum_i \frac{[M_{11}(a_{xu}z_i + b_{xu}) + M_{12}(a_{yu}z_i + b_{yu}) + M_{13}(z_i - (z_0)_i) - m_i]^2}{\sigma_i^2} + \\ &\quad \sum_j \frac{[M_{11}(a_{xd}z_j + b_{xd}) + M_{12}(a_{yd}z_j + b_{yd}) + M_{13}(z_j - (z_0)_j) - m_j]^2}{\sigma_j^2}, \end{aligned} \tag{A.24}$$

where the indices $i$ and $j$ correspond to the hits of the upstream and downstream chambers associated to the track respectively. Using the constraints in Equations A.20, A.21 and A.22, the above $\chi^2$ can be rewritten as

$$\begin{aligned} \chi^2 &= \sum_i \frac{[M_{11}(a_{xu}z_i + b_{xu}) + M_{12}(a_{yu}z_i + b_{yu}) + M_{13}(z_i - (z_0)_i) - m_i]^2}{\sigma_i^2} + \\ &\quad \sum_j \frac{[M_{11}(a_{xd}z_j + b_{xu}) + M_{12}(G^{-1}a_{yu}z_j + b_{yu}) + M_{13}(z_j - (z_0)_j) - m_j]^2}{\sigma_j^2}. \end{aligned} \tag{A.25}$$

The five unknown parameters are $a_{xu}$, $a_{yu}$, $b_{xu}$, $b_{yu}$ and $a_{xd}$. Since $z_i$, $z_j$ and the factor $G$ depends on the parameters being estimated, the problem of minimizing Equation A.25 becomes a non-linear problem. However, to a good approximation, $z_i$, $z_j$ and the factor $G$ can be treated as constants, then minimizing Equation A.25 is a linear problem and can be solved analytically.

### A.5.4 Complete Track Candidates

The minimum $\chi^2$, $\chi^2_{min}$, obtained from minimizing Equation A.25 can be taken to express the quality of the track candidate. A cut is made on this $\chi^2_{min}$ to reject poorly reconstructed complete track candidates.

In some cases, more that one upstream track candidates will match to a downstream track candidate. Hence, the $\chi^2_{min}$ is also used to discriminate the matching of track segments. The pair of upstream and downstream track segments with the smallest $\chi^2_{min}$ is selected as the complete track candidate.

# Appendix B

# Single-Vertex Geometric Fit (GFIT1V)

A better estimation of the track parameters can be obtained by performing a global constrained fit to reflect the topology of an $N$-prong decay of a particle. The decay particles emanate from a common point called a vertex. As the decay particles propagate through the spectrometer, each decay particle leaves two track segments (upstream track and downstream track) that intersect at the mean bend plane, producing a kink in the X-Z plane. This kink is a result of the $p_t$ kick of the analysis magnet in the X direction.

The upstream track segment of track $n$ can be described by the following equations:

$$x_n = a_{xu,n}z + b_{xu,n}, \tag{B.1}$$

$$y_n = a_{yu,n}z + b_{yu,n}, \tag{B.2}$$

where $a_{xu,n}$ and $a_{yu,n}$ are the X and Y slopes of the upstream track segment respectively, $b_{xu,n}$ and $b_{yu,n}$ are the X and Y intercepts of the upstream track respectively. The position $z$ is measured from $z_{bendplane}$. Similar equations exist for the downstream track segment:

$$x_n = a_{xd,n}z + b_{xd,n}, \tag{B.3}$$

$$y_n = a_{yd,n}z + b_{yd,n}. \tag{B.4}$$

A $\chi^2$ function similar to Equation A.24 is constructed summing over all the tracks of an event:

$$\chi^2 = \sum_n \left[ \sum_i \frac{[M_{11}(a_{xu,n}z_i + b_{xu}) + M_{12}(a_{yu,n}z_i + b_{yu}) + M_{13}(z_i - (z_0)_i) - m_i]^2}{\sigma_i^2} + \right.$$

$$\sum_j \frac{[M_{11}(a_{xd,n}z_j + b_{xd}) + M_{12}(a_{yd,n}z_j + b_{yd}) + M_{13}(z_j - (z_0)_j) - m_j]^2}{\sigma_j^2}\Bigg]. \quad \text{(B.5)}$$

The constraints reflecting the kink at the mean bend plane are given by (see description following Equation A.20, A.21 and A.22 for more details)

$$b_{xu,n} = b_{xd,n}, \quad \text{(B.6)}$$

$$b_{yu,n} = b_{yd,n}, \quad \text{(B.7)}$$

$$a_{yu,n} = G a_{yd,n}, \quad \text{(B.8)}$$

where

$$G = \sqrt{\frac{1 + a_{xu,n}^2}{1 + a_{xd,n}^2}}. \quad \text{(B.9)}$$

In addition, the equations for constraining all the tracks to a vertex are given by

$$x_D = a_{xu,n}z_D + b_{xu,n}, \quad \text{(B.10)}$$

$$y_D = a_{yu,n}z_D + b_{yu,n}, \quad \text{(B.11)}$$

where $x_D, y_D$, and $z_D$ are the coordinates of the vertex.

Using the above constraints, Equation B.5 becomes

$$\chi^2 = \sum_n \Bigg[ \sum_i \frac{[M_{11}\{a_{xu,n}(z_i - z_D) + x_D\} + M_{12}\{a_{yu,n}(z_i - z_D) + y_D\} + M_{13}(z_i - (z_0)_i) - m_i]^2}{\sigma_i^2} + \sum_j \frac{[M_{11}(a_{xd,n}z_j - a_{xu,n}z_D + x_D) + M_{12}\{a_{yu,n}(G^{-1}z_j - z_D) + y_D\} + M_{13}(z_j - (z_0)_j) - m_j]^2}{\sigma_j^2}\Bigg]. \quad \text{(B.12)}$$

Specifically, for charged $K \to 3\pi$ decay, $n = 3$ and there are 12 unknown parameters: $x_D$, $y_D$, $z_D$, $a_{xu,1}$, $a_{xu,2}$, $a_{xu,3}$, $a_{yu,1}$, $a_{yu,2}$, $a_{yu,3}$, $a_{xd,1}$, $a_{xd,2}$ and $a_{xd,3}$. Because of the terms containing $z_D$, minimizing Equation B.12 is a non-linear problem requiring an iterative method.

The $\chi^2$ function can be expanded in a Taylor series:

$$\chi^2(\alpha) = \chi^2(\alpha_0) + \sum_m \left.\frac{\partial \chi^2}{\partial \alpha_m}\right|_{\alpha_0} (\alpha_m - \alpha_{0m}) + \frac{1}{2}\sum_{m,n} \left.\frac{\partial^2 \chi^2}{\partial \alpha_m \partial \alpha_n}\right|_{\alpha_0} (\alpha_m - \alpha_{0m})(\alpha_n - \alpha_{0n}) + ..., \quad \text{(B.13)}$$

where $\alpha$'s are the fitting parameters and $\alpha_0$'s are the initial values. Ignoring higher-order terms and differentiating Equation B.13 with respect to the $k$th component of $\alpha$ gives

$$\left.\frac{\partial \chi^2}{\partial \alpha_k}\right|_{\alpha} = \left.\frac{\partial \chi^2}{\partial \alpha_k}\right|_{\alpha_0} + \frac{1}{2}\sum_m \left.\frac{\partial^2 \chi^2}{\partial \alpha_m \partial \alpha_k}\right|_{\alpha_0} (\alpha_k - \alpha_{0k}). \quad \text{(B.14)}$$

The next iteration toward $\alpha$ can be obtained by setting $\partial\chi^2/\partial\alpha_k|_\alpha = 0$:

$$\alpha = \alpha_0 - V|_{\alpha_0} \cdot Q|_{\alpha_0}, \tag{B.15}$$

where V is a matrix whose $(m,n)$th components is $V^{-1}_{mn} = \frac{1}{2}\partial^2\chi^2/\partial\alpha_m\partial\alpha_n$, and Q is a vector whose $m^{\text{th}}$ component is $\partial\chi^2/\partial\alpha_m$. Equation B.15 is used to find the solution by iteration which will terminate when the $\chi^2$ is in the vicinity of a minimum to within a preset tolerance.

A set of good initial values $\alpha_0$ is needed for the first iteration. All the slopes of the tracks can be taken from the result of the global track fitting (see Appendix A). The remaining parameters that need to be estimated are the coordinates of the vertex. An estimation of the vertex can be obtained by minimizing a function $D$ that expresses the sum of the separations between pairs of tracks:

$$D = \sum_m \sum_{n>m} [(x_m - x_n)^2 + (y_m - y_n)^2], \tag{B.16}$$

where $x_n$ and $y_n$ are given by Equation B.1 and B.2 respectively.

Monte Carlo events are used to assess the performance of the event reconstruction algorithm. Figures B.1, B.2 and B.3 show the distributions of the difference between reconstructed and generated values for some kinematical parameters. All the distributions centered close to zero but tail off much slowly than Gaussian distributions because the resolutions are not constants but depend on the parameters themselves (for example, the momentum resolution of the tracks depends quadratically on the momentum). The root mean square (RMS) of the distributions can be taken as a measure of the mean resolution for the respective parameters. In addition, Figures B.4 and B.5 show the comparisons of the reconstructed $3\pi$ mass and the reduced GFIT1V $\chi^2$ distributions between the real data and reconstructed Monte Carlo generated data.

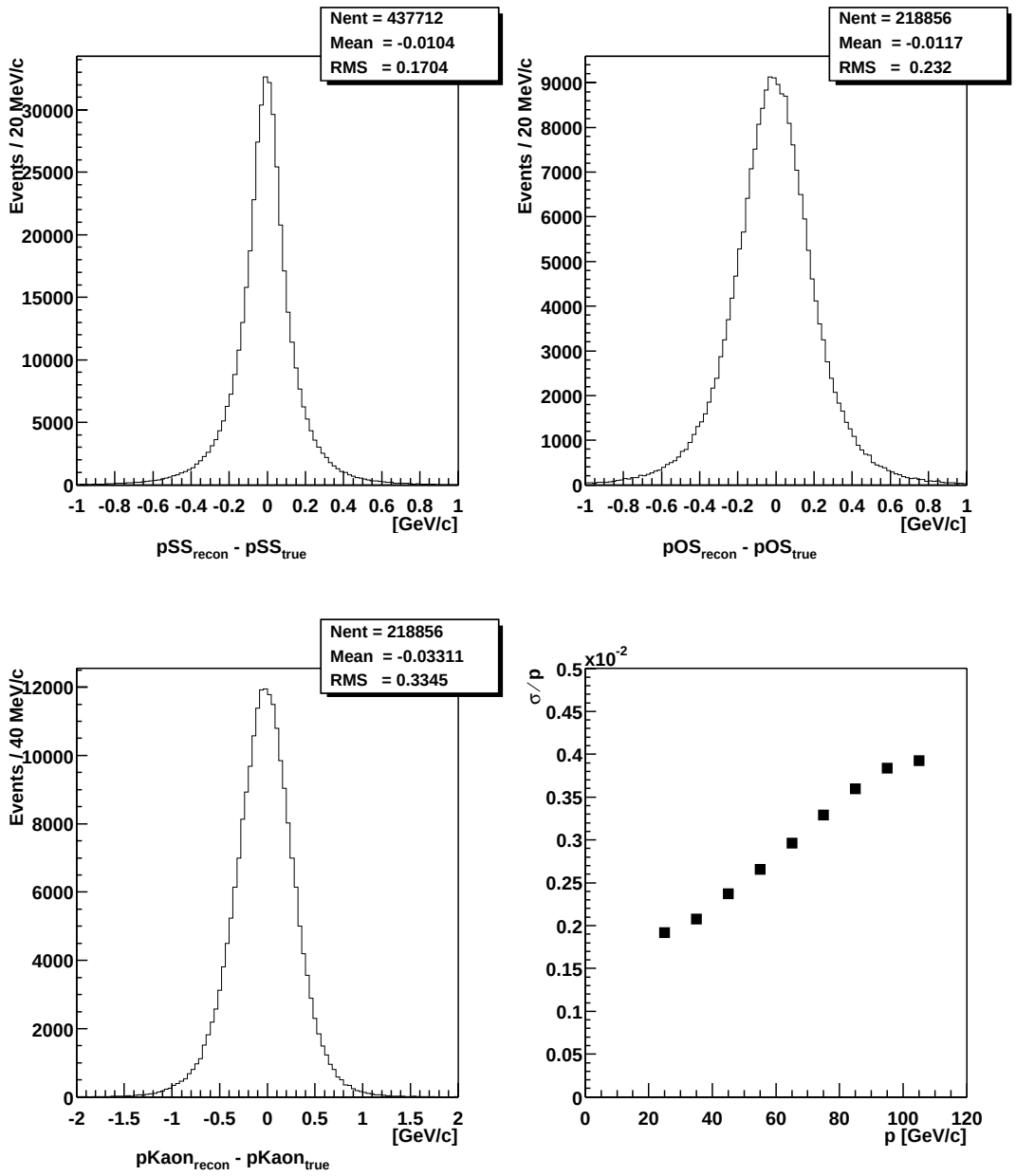


Figure B.1: Distributions of difference between reconstructed and generated SS momentum (top left), OS momentum (top right) and Kaon momentum (bottom left). The bottom right plot shows the relative momentum resolution as a function of momentum. Except for the end points, the relationship, as expected is linear.

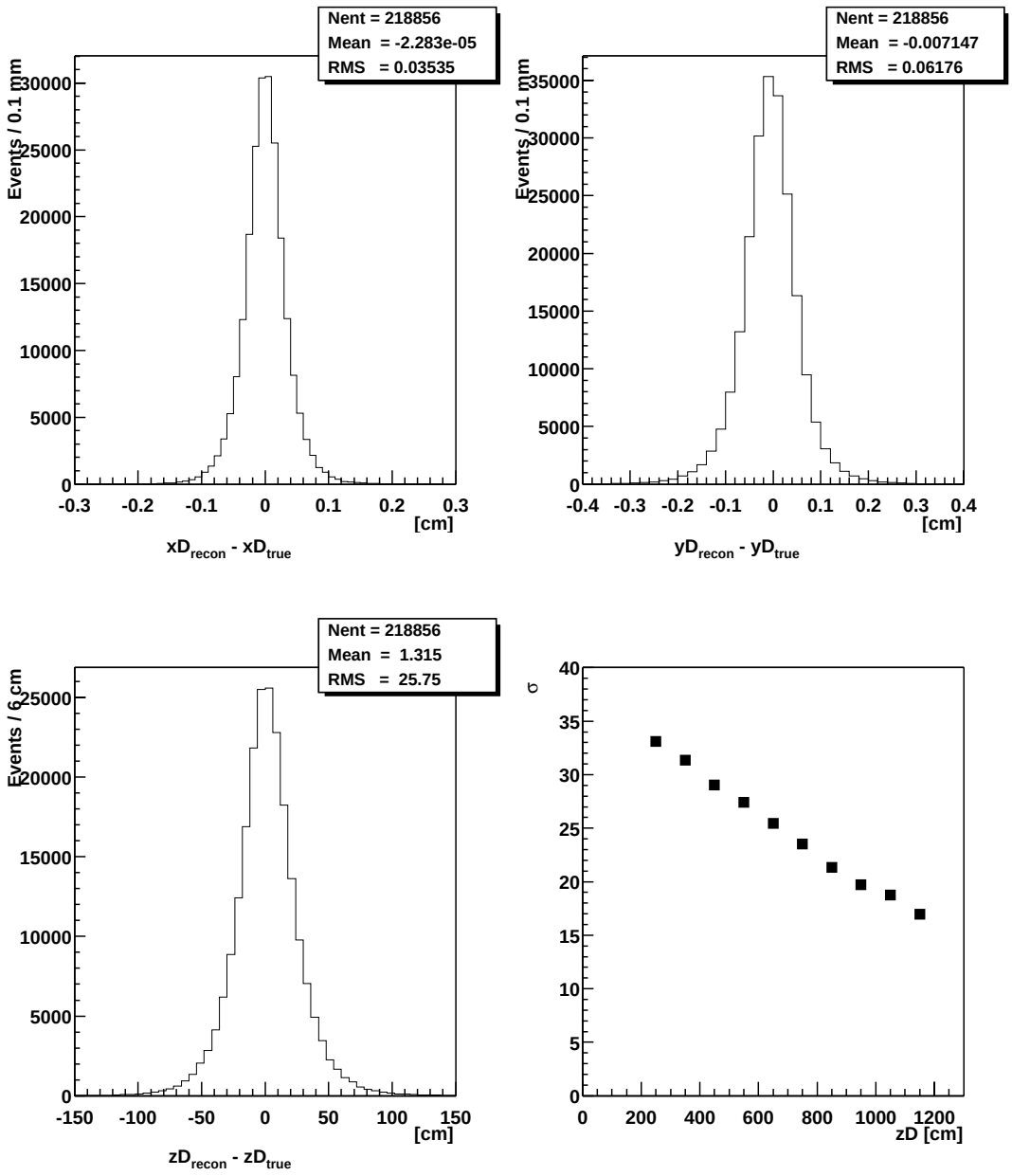


Figure B.2: Distributions of difference between reconstructed and generated X coordinate (top left), Y coordinate (top right) and Z coordinate (bottom left) of the decay vertex. The bottom right plot shows the resolution of the Z coordinate as a function of the Z.

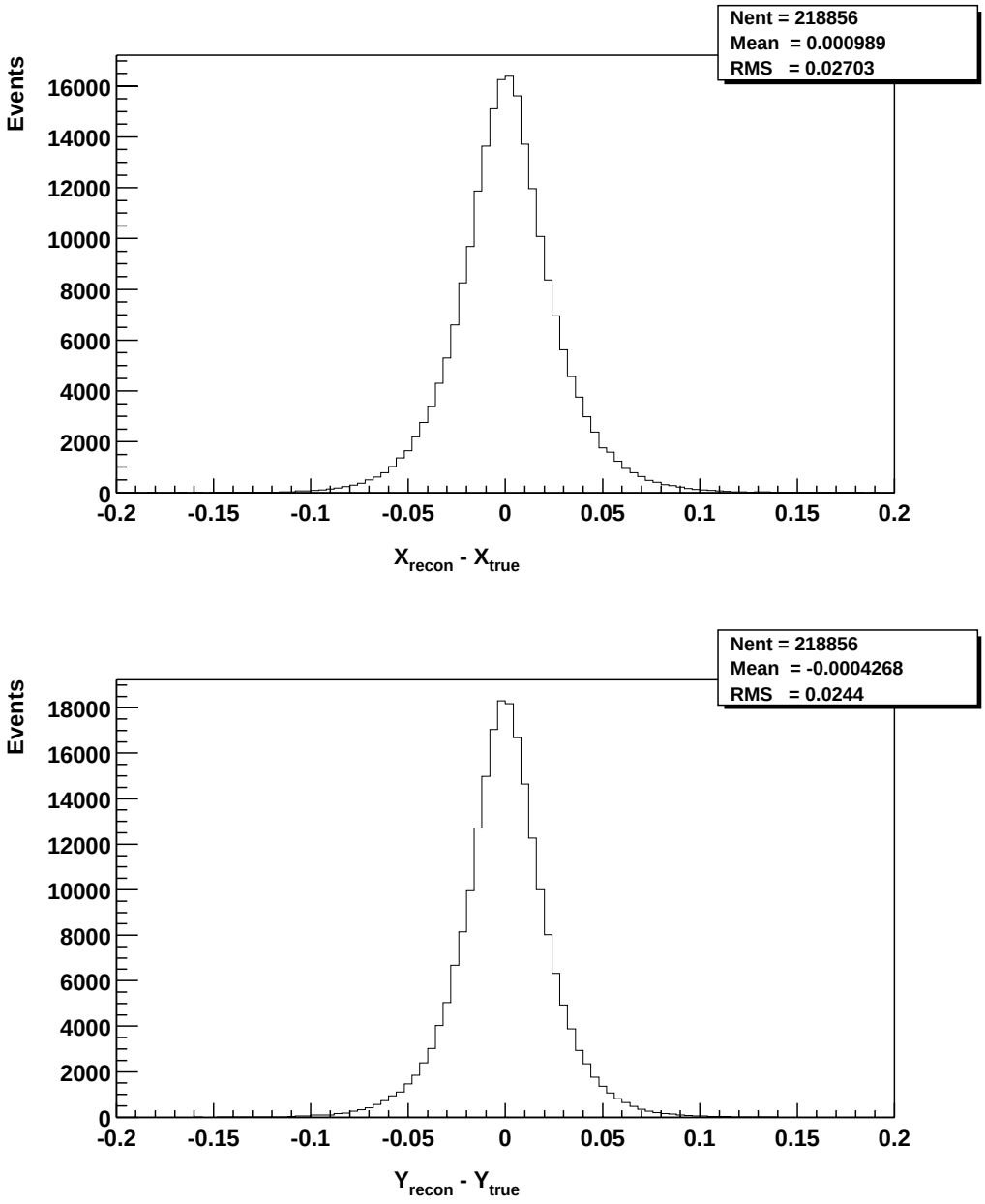


Figure B.3: Distributions of the difference between reconstructed and generated X (top) and Y (bottom) parameters of the Dalitz plot.

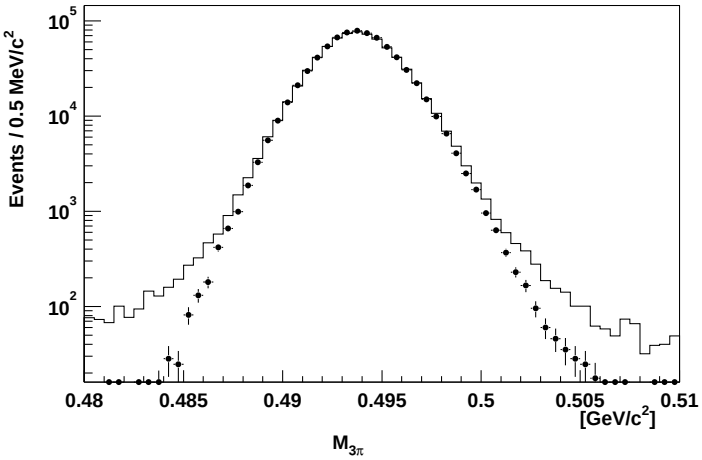


Figure B.4: Comparisons of reconstructed $3\pi$ invariant mass distributions between real data (histogram) and MC events (points). The excess of events away from the peak in the real data is due to background contaminations.

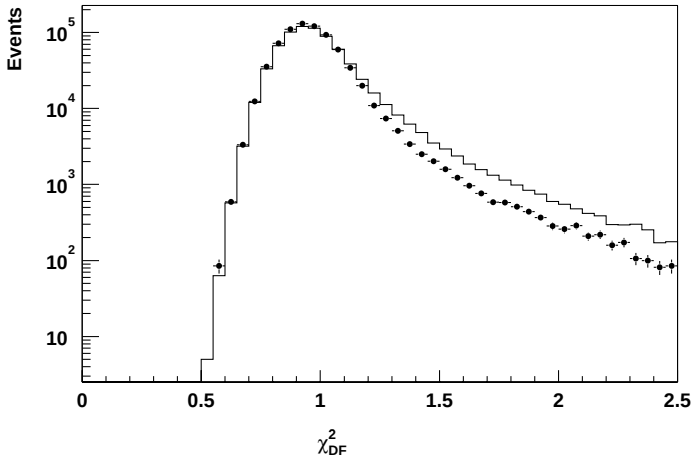


Figure B.5: Comparisons of reduced GFIT1V $\chi^2$ distributions between real data (histogram) and MC events (points). The disagreement may be due to background contaminations, and the fact that not all effects were properly simulated and fine tuned in the Monte Carlo.

# Appendix C

# Target Trace-Back

From the three tracks forming the Kaon event, the momentum of the Kaon can be reconstructed. Using this momentum and the decay vertex, the position of the Kaon at the exit of the collimator can be calculated. The beam can also be linearly extrapolated back to the target in the horizontal direction as the magnetic field inside the collimator is along the horizontal, producing a kick in the vertical direction. Charged particles follow a circular trajectory in a vertical plane inside the collimator as a result of the applied magnetic field. As described in Section 2.2, the central orbit is described by a charged particle with a momentum $p_c = 156.7$ GeV/c and is along the horizontal direction at $z_{target} = -638.8$ cm. Using the equation of motion of a charged particle in a uniform magnetic field, the Y coordinate, $y_c$, of this central orbit measured from a linear coordinate system is given by

$$y_c(z) = 0.3 q_c \int_{z_{target}}^{z} \int_{z_{target}}^{z''} \frac{B}{p_c} dz' dz'', \tag{C.1}$$

where $q_c$ is the charge of the particle in unit of proton charge, $B$ is the magnetic field, in Tesla, inside the collimator magnet along the vertical, and the Z position is measured in meter.

For a particle with charged $q$, momentum $p$, and an angle $\theta_{target}$ made with the Z-axis at $z_{target}$, the equation of motion is given by

$$y(z) = y(z_{target}) + (z - z_{target}) tan\ \theta_{target} + 0.3 q \int_{z_{target}}^{z} \int_{z_{target}}^{z''} \frac{B}{p} dz' dz''. \tag{C.2}$$

Since $p$ and $p_c$ are constant, they can be taken out of the double integral. Subtracting

Equation C.1 from C.2 yields

$$y(z) - y_c(z) = y(z_{target}) + (z - z_{target})tan\ \theta_{target} + \left(\frac{q}{p} - \frac{q_c}{p_c}\right) 0.3 \int_{z_{target}}^{z} \int_{z_{target}}^{z^{''}} B dz^{'} dz^{''}. \tag{C.3}$$

By definition, $y_c(z) = 0$ for all $z$ inside the collimator. Solving Equation C.3 for $y(z_{target})$ yields

$$y(z_{target}) = y(z) - (z - z_{target})tan\ \theta_{target} - \left(\frac{q}{p} - \frac{q_c}{p_c}\right) 0.3 \int_{z_{target}}^{z} \int_{z_{target}}^{z^{''}} B dz^{'} dz^{''}. \tag{C.4}$$

In order to trace a charged particle of momentum $p$ back to the target, we would need to know the Y position and the angle $\theta$ at a certain Z position inside the collimator. This Z position is taken to be at the exit of the collimator.

Taking $B$ as a constant, the term containing the double integral is simplified to

$$\left(\frac{q}{p} - \frac{q_c}{p_c}\right) 0.3 \int_{z_{target}}^{L} \int_{z_{target}}^{z^{''}} \frac{B}{p} dz^{'} dz^{''} = \frac{1}{2} 0.3 B L^2 \left(\frac{q}{p} - \frac{q_c}{p_c}\right), \tag{C.5}$$

where $L = 6.096$ m is the length of the collimator.

To calculate the angle $\theta_{target}$, consider a charged particle of momentum $p$ going through the collimator. The charged particle will receive a vertical kick:

$$p\ sin(\theta(z_{collimator})) - p\ sin\ \theta_{target} = 0.3 q B L, \tag{C.6}$$

where $\theta(z_{collimator})$ is the angle of the particle at the exit of the collimator made with the Z axis. On the other hand, $\theta(z_{collimator})$ is the sum of $\theta_{target}$ and the bend angle of the particle, $\theta_{bend}$, after tranversing the collimator:

$$\theta(z_{collimator}) = \theta_{target} + \theta_{bend}. \tag{C.7}$$

Assuming small-angle approximation, which is valid in this experiment, $\theta_{bend}$ is given by

$$\theta_{bend}(p) = 0.3 q B L \frac{1}{p}. \tag{C.8}$$

Relative to the central orbit, the Y slope of the particle at the exit of the collimator is

$$\frac{p_y}{p_z} = (\theta_{target} + \theta_{bend}(p)) - \theta_{bend}(p_c). \tag{C.9}$$

Using Equation C.8, $\theta_{target}$ is found to be

$$\theta_{target} = \frac{p_y}{p_z} - 0.3 B L \left(\frac{q}{p} - \frac{q_c}{p_c}\right). \tag{C.10}$$

Therefore, using C.5 and C.10, Equation C.4 becomes

$$y(z_{target}) = y(z_{collimator}) - L \left[\frac{p_y}{p_z} - 0.3 B L \left(\frac{q}{p} - \frac{q_c}{p_c}\right)\right] - \frac{1}{2} 0.3 B L^2 \left(\frac{q}{p} - \frac{q_c}{p_c}\right). \tag{C.11}$$

# Bibliography


[1] E. Noether, Nachr. Kgl. Geo. Wiss Gottinger **235**, (1918).

[2] C.S. Wu, E. Amber, R. Hayward, D. Hoppes, and R. Hudson, Phys. Rev. **105**, 1413 (1957).

[3] R.L. Garwin, L.M. Lederman, and M. Weinrich, Phys. Rev. **105**, 1415 (1957).

[4] J.H. Christenson, J. Cronin, V. Fitch, and R. Turlay, Phys. Rev. Lett **13**, 138 (1964).

[5] S.L. Glashow, Nucl. Phys. **22**, 579 (1961).

[6] S. Weinberg, Phys. Rev. Lett. **19**, 1264 (1967).

[7] A. Salam, in *Elementary Particle Theory (Nobel Symposium No. 8)*, edited by N. Svartholm (Almqvist and Wiksell, Stockholm, 1968).

[8] P.W. Higgs, Phys. Rev. Lett **12**, 132 (1964).

[9] P.W. Higgs, Phys. Rev. Lett **145**, 1156 (1966).

[10] N. Cabibbo, Phys. Rev. Lett. **10**, 531 (1963).

[11] M. Kobayashi and T. Maskawa, Prog. Theor. Phys. **49**, 652 (1973).

[12] L.-L. Chau and W.-Y. Keung, Phys. Rev. Lett. **53**, 1802 (1984).

[13] A. Alavi-Harati *et al.*, Phys. Rev. Lett. **83**, 22 (1999).

[14] C. Caso *et al.* (Particle Data Group), Eur. Phys. J. C **3**, 1 (1998).

[15] C. Zemach, Phys. Rev. **133**, 1201 (1964).

[16] T.J. Devlin and J.O. Dickey, Rev. Mod. Phys. **51**, 237 (1979).

[17] G. Isidori, L. Maiani, and A. Pugliese, Nucl. Phys. **B**, 522 (1992).

[18] G. D'Ambrosio, G. Isidori, A. Pugliese, and N. Paver, Phys. Rev. **D50**, 5767 (1994).

[19] G. D'Ambrosio and G. Isidori, Intl. Jour. Mod. Phys. **13**, 1 (1998).

[20] M.K. Gaillard and B.W. Lee, Phys. Rev. Lett. **33**, 108 (1974).

[21] G. Altarelli and L. Maiani, Phys. Lett. **52B**, 351 (1974).

[22] F.J. Gilman and M.B. Wise, Phys. Rev **D20**, 2392 (1979).

[23] G. Altarelli, G. Curci, G. Martinelli, and S. Petrarca, Nucl. Phys. **B187**, 461 (1981).

[24] H.-Y. Cheng, Phys. Rev **D44**, 919 (1991).

[25] G. D'Ambrosio, G. Isidori, and N. Paver, Phys. Lett. **B273**, 497 (1991).

[26] E. P. Shabalin, Nucl. Phys. **B409**, 87 (1993).

[27] A. Bel'kov, G. Bohm, D. Ebert, A. Lanyov, and A. Schaale, Phys. Lett. **B300**, 283 (1993).

[28] E. Shabalin, ITEP Preprint 8-98 (1998).

[29] W.T. Ford *et al.*, Phys. Rev. Lett. **25**, 1370 (1970).

[30] Group 3 Model LPT-141 at 3.0 Tesla full-scale, Group 3 Technology Ltd., P.O. Box 71-111 Rosebank, Auckland 7, New Zealand.

[31] Y.C. Chen *et al.*, accepted for publication in Nucl. Instr. Meth. (2000).

[32] S. Amato *et al.*, Nucl. Instr. Meth. **A324**, 535 (1993).

[33] G. Bunce, Nucl. Instr. Meth. **172**, 553 (1980).

[34] P.T. Cox, Ph.D. thesis, University of Michigan, 1980.

[35] K.-B. Luk, Ph.D. thesis, Rutgers University, 1983.

[36] P.-M. Ho, Ph.D. thesis, University of Michigan, 1990.

[37] *Landolt-Börnstein: Numerical Data and Functional Relationships in Science and Technology, New Series I/12a*, edited by O. Madelung (Springer-Verlag, Berlin Heidelberg New York, 1988).